Development and characterization of a LaB_6 based high brightness field emission electron source

Dissertation

zur Erlangung des Doktorgrades

Des Department Physik

Der Universität Hamburg

vorgelegt von

GOPAL SINGH

aus Neu Delhi, Indien

Hamburg 2020

Gutachter/in der Dissertation:	Professor Dr. R.J. Dwayne Miller Professor Dr. Franz X. Kärtner
Gutachter/in der Disputation:	Professor Dr. Andreas Stierle Dr. Sadia Bari
Vorsitzender des Prüfungsausschusses:	Professor Dr. Sven-Olaf Moch
Datum der Disputation:	13/11/2020

Abstract

Recent scientific advancements made it possible to track physical, chemical and biological reactions in space and time simultaneously. Cryo-electron microscopy (cryo-EM), which bagged the Nobel prize of 2017, enables a better understanding of biological structures at the atomic level. However, it does not provide information about dynamical events faster than a few ms. Radiation damage and beam-induced motion blurring are other concerns in cryo-EM. In principle, in-liquid microscopy is a promising alternative capable of fully tracking molecular trajectories. However, specimen motion in the liquid environment results in resolution loss. Hence, short-pulse, high-brightness electron beams are needed to use the full potential of in-liquid microscopy.

The current Ph.D. work is a step towards the development and the characterization of an electron source that can fulfil the brightness requirement of in-liquid microscopy. Brightness is defined as the angular current density per unit emission area. A novel fabrication method of a LaB_6 field emitter source, using a combination of electrochemical etching and FIB milling, has been developed. These sharp emitters with size less than 100 nm can provide a brightness, defined in terms of reduced and angular normalized brightness, of up to $10^9 Am^{-2}Sr^{-1}V^{-1}$ for electron microscopes. Moreover, experimental setups to characterize the energy spread and the angular current density of the resultant electron beam have been built. Additionally, the fabricated field emitters were triggered by pulsing the extraction voltage to generate 10µs e-pulses. The versatility of these field emitters is enhanced by the fact that they can emit >10 µA peak current in 10µs pulse duration at the same vacuum environment as Schottky emitters.

The experimental output of the current Ph.D. work is a promising leap towards the dream of capturing the structure and dynamics of biological systems in their native state on a molecular level.

Zusammenfassung

Jüngste wissenschaftliche Fortschritte machten es möglich, physikalische, chemische und biologische Reaktionen in Raum und Zeit gleichzeitig zu verfolgen. Die Kryo-Elektronenmikroskopie (Kryo-EM), die mit dem Nobelpreis 2017 ausgezeichnet wurde, ermöglicht ein besseres Verständnis der biologischen Strukturen auf atomarer Ebene. Sie liefert jedoch keine Informationen über dynamische Ereignisse, die schneller als einige ms ablaufen. Strahlenschäden und strahlinduzierte Bewegungsunschärfen sind weitere Probleme bei der Kryo-EM. Im Prinzip ist die In-Flüssigkeits-Mikroskopie eine vielversprechende Alternative, die in der Lage ist, molekulare Trajektorien vollständig zu verfolgen. Allerdings führt die Bewegung der Probe in der flüssigen Umgebung zu Auflösungsverlusten. Daher werden kurzpulsige Elektronenstrahlen mit hoher Helligkeit benötigt, um das volle Potenzial der In-Flüssigkeits-Mikroskopie zu nutzen.

Die aktuelle Doktorarbeit ist ein Schritt in Richtung der Entwicklung und Charakterisierung einer Elektronenquelle, die die Helligkeitsanforderungen der In-Flüssigkeits-Mikroskopie erfüllen kann. Die Helligkeit ist definiert als die Winkelstromdichte pro Einheit der Emissionsfläche. Es wurde ein neuartiges Herstellungsverfahren einer LaB_6-Feldemissionsquelle entwickelt, das eine Kombination aus elektrochemischem Ätzen und FIB-Fräsen verwendet. Diese scharfen Emitter mit einer Größe von weniger als 100 nm können eine Helligkei

Declaration

Declaration on oath

I hereby declare, on oath, that I have written the present dissertation by my own and have not used other than the acknowledged resources and aids.

Eidesstattliche Versicherung

Hiermit erkläre ich an Eides statt, dass ich die vorliegende Dissertationsschrift selbst verfasst und keine anderen als die angegebenen Quellen und Hilfsmittel benutzt habe.

Gopal Singh

Table of Contents

1 Introduction 1

2 Electron emission processes and source characterization parameters: Theory 5

2.1 Primary electron emission mechanisms 5

2.1.1 Thermionic emission 6

2.1.2 Photoemission 6

2.1.3 Schottky emission 7

2.1.4 Field emission 10

2.1.5 Primary factors affecting the field emission operation 12

2.2 Source parameters 15

2.2.1 Angular current density 15

2.2.2 Effective source size 15

2.2.3 Reduced Brightness 19

2.2.4 Energy spread 20

2.3 Comparison of electron sources used in conventional TEM 20

2.4 Need for a new field emitter to fulfil the dream of single-shot high-resolution phase-contrast imaging 20

3 Description of the relevant experimental setup, devices, and electronic circuit boards 23

3.1 Electrochemical etching set-up 23

3.1.1 First-generation set-up 24

3.1.2 Second-generation set-up 25

3.2 Focused ion beam (FIB) machine 26

3.3 Test chamber 28

3.4 Energy Analyzer 30

4 Fabrication of Tungsten (W) Lanthanum Hexaboride (LaB_6) cold field emitter and their characterization 32

4.1 Fabrication of emitters 33

4.1.1 Tungsten (W) emitter fabrication 33

4.1.2 Lanthanum Hexaboride emitter fabrication, challenges and solution 37

4.2 Surface study of the fabricated tip 44

4.3 Gallium implantation issues and the damage of the LaB_6 surface 46

5 Characterization of the fabricated electron sources 50

5.1 Field emission measurements of W and LaB_6 50
5.2 Reproducibility test of our method of fabrication 54
5.3 Temporal stability of fabricated tips 57
5.3.1 W tips 57
5.3.2 LaB_6 tips 60
5.4 Angular current density 63
5.5 Energy spread measurements 66
5.5.1 In- house built electron energy analyzer 67
5.5.2 Experimental results and analysis 68
5.6 The temperature profile of fabricated tips during electron emission 71
5.6.1 Nottingham effect 72
5.6.2 Theoretical study of fabricated tip emitter temperature profile 74
5.7 Generation and characterizations of microsecond pulses from fabricated LaB_6 emitters 79
5.7.1 Enhancing the longevity of the electron source 79
5.7.2 In-house developed microsecond high voltage (µs-HV) pulse generator 80
5.7.3 Generation of high current pulses 81
5.7.4 Characterization of the high current microsecond pulses 83
5.8 Summary 88

6 Development of a coherence measurement setup: towards brightness estimation 89

6.1 Theoretical concepts 89
6.1.1 Reduced brightness and limitation of its formulation 89
6.1.2 Theoretical considerations of brightness and its quantum limitations 90
6.2 Results and developments 93
6.2.1 Reduced brightness B_r 93
6.2.2 Ultimate brightness B_{max} and degeneracy δ 95
6.3 Lateral coherence length L_{sc} and the development of a point projection microscope (PPM) 95
6.3.1 Image formation in PPM 96
6.3.2 The relation between coherence length and effective radius 96
6.3.3 In-house built point projection microscope and results 97

7 Conclusion and Outlook 103

Appendices **107**
References **112**
Acknowledgements **126**

List of Figures

Figure 2.1 Schematic of energy diagram showing the (Schottky effect) bending of potential barrier at different applied fields (red, green and blue) compared to the absence of field (black line) 8

Figure 2.2 Diagram illustrating the concept of induced image-charge (+*e*) by the electron (-*e*), resulting in image charge potential 9

Figure 2.3 a) Smoothening effect and charge distribution at b) (100) smooth surface and c) (110) rough surface 13

Figure 2.4 Illustration of electron momenta and angles at the emitter-vacuum interface during electron emission 16

Figure 2.5 Refraction of electrons at curved boundary 17

Figure 2.6 The backward extension of the trajectory of an electron are not meeting at the Gaussian image plane, but forming a disc of confusion r_{eff} 18

Figure 3.1 Illustration of the schematic (left) and photograph (right) of the 1st generation of electrochemical set-up during etching of LaB_6 rod 24

Figure 3.2 a) Schematic of the second generation electrochemical etching setup. A gold ring of 5 mm diameter was used to carry the electrolyte near to the rod. b) The photograph of the setup showing its different components c) An enlarged view of the LaB_6 rod dipping in the electrolyte carrying gold ring 26

Figure 3.3 Focussed ion beam (FIB) milling facility in Prof. Henry Chapmann group used for sharpening the LaB_6 microtip in the current thesis 27

Figure 3.4 Schematic of the focused ion beam (FIB) milling process. An ion beam is used to modify the target surface and an electron beam to monitor the milling process. 28

Figure 3.5 Photograph illustrating the different components of the test chamber used to characterize the fabricated electron (LaB_6 and W) source 29

Figure 3.6 Illustration of the Computer-aided-design (CAD) of the in-house developed retarding potential energy analyzer. The schematic and working of this device is explained in chapter 5 31

Figure 4.1 Photo of the spot-welding machine in S. T. Purcell group in Lyon, France 33

Figure 4.2 a) Schematic of tungsten (W) wire mounted on a ceramic mount, b) Photo of Tantalum wedge welded on ceramic to make an electrical connection between W wire and ceramic legs or pins 34

Figure 4.3 Snapshot of Electrochemical etching set up in S.T. Purcell group in Lyon showing electronics (labeled) associated with the setup 35

Figure 4.4 Schematic of the vortex flow during the electrochemical etching that regulates the flow of the tungstate ions and determines the shape of the tip 36

Figure 4.5 Tungsten tip fabricated by immersing tungsten wire a) 0.5mm and b) 1mm in an electrolytic solution (1M NaOH) 36

Figure 4.6 Simple cubic structure of Lanthanum Hexaboride (LaB_6) with one Lanthanum in the middle surrounded by Boron octahedra structures 37

Figure 4.7 The photograph showing inside view of the laser welding facility located in the University of Hamburg workshop located on the DESY campus 38

Figure 4.8 a) Schematic and b) photo of LaB_6 mounting assembly showing LaB_6 rod inserted inside the W wrapped Ta tube 39

Figure 4.9 Photograph showing Hydrogen bubbling around the LaB_6 surface on reacting with phosphoric acid 40

Figure 4.10 Optical microscope image showing boron phosphate particle around the tip, uneven bright and dark spots are due to uneven surface resulting in partial shadowing 40

Figure 4.11 Schematic showing the immersed LaB_6 in electrolytic solution a) that results in the formation of boron phosphate (BPO_4) and Lanthanum hydroxide ($La(OH)_3$), intermediate steps b), c) d) shows the thinning down of the tip apex resulting into 1-10μm sharp tip e)..........41

Figure 4.12 SEM image showing the morphology of LaB_6 electrochemically etched emitters with 40 minutes (left) and 60 minutes (right). (Scale bar represents 20μm) (Images were captured by the author in Henry Chapman's FIB/SEM lab located in CFEL) 42

Figure 4.13. EDX spectrum shows sharp peak of La and B after chemical etching 43

Figure 4.14 Schematic of FIB milling of LaB_6 needle (left), LaB_6 tip after FIB milling (right), inset is showing apex of the tip. Images are taken from Singh *et al.*[150] 43

Figure 4.15 HRTEM image of the FIB milled LaB6 tip apex, inset is showing the electron diffraction pattern. Image taken from Singh *et al.* [150] 45

Figure 4.16 EDX spectrum of LaB_6 tip at accelerating voltage of 5 keV 46

Figure 4.17 Simultation results of Ga ion trajectory (sky blue) inside the LaB6 and red dots showing the defect (vacancies) created during FIB milling 47

Figure 4.18 Sputtering yields of La and B atoms on hitting with energetic 30 keV Ga beam 48

Figure 4.19 Gallium ions distribution inside the FIB milled LaB_6 tip showing a peak at 8.9nm 49

Figure 4.20 Graph showing the number of vacancies formation inside the fabricated LaB_6 tip per target atom 49

Figure 5.1 Schematic of the test chamber (photo shown in Chapter 3) used to measure the field emission current 50

Figure 5.2 a) SEM image of W(111) tested in the vacuum chamber for its I-V characteristic, b) field emission micrograph (FEM) of W(111) tip...51

Figure 5.3 Graph showing experimental I-V data (black dots) of W tip fitting very well with theoretical F-N model (solid blue line), (inset) showing F-N plot of the same tip, straight-line fit confirms the emission of electron from the localized state of W 51

Figure 5.4 (left) SEM image of LaB_6 (100) tip before testing for field emission test, (right) FEM image of LaB_6 oriented along (100) direction 53

Figure 5.5 Experimental I-V data (black squares) of LaB_6 tip orientated along (100) direction with theoretical model fit (solid red line), inset showing linear F-N plot of the tip 53

Figure 5.6 SEM images of some of the fabricated LaB_6 tip right after FIB milling process, it can be seen that the shapes (conical) of all the emitters are almost identical (Image (b) is taken from Singh *et al.* [150]) 55

Figure 5.7 I-V curves of two tips (with the same initial diameter 70nm) after thermal conditioning cycles 56

Figure 5.8 Emission current temporal profile of the W (111) tip at 7×10^{-10} mbar 57

Figure 5.9 Schematic of physisorption potential at the emitter (metal) surface, dotted curves represents the variation in adsorption potential. An adsorbate (blue dot) can cross the barrier ΔU only when its thermal energy kT> ΔU 58

Figure 5.10 Schematic showing the anode sputtering and ion desorption phenomenon, arrows depicting the direction of ions (red) and electrons (black) 59

Figure 5.11 Temporal stability of LaB_6 tip1 (black, red and green), tip2(blue and violet) and tip3 (yellow), recorded at $\mathbf{5 \times 10 - 9}$ mbar chamber pressure, for 30 minutes. Negligible drop in current was observed. Some fluctuations were observed at around 10 nA emission current, which might be due to enhanced ion collision events at higher extraction voltage (Image taken from Singh *et al*. [161]) 60

Figure 5.12 Top and side view of LaB_6 bulk with (100) terminated plane....................61

Figure 5.13 Power spectrum of the noise in emission current during 24 hours operation, in 10^{-3}-1 Hz ranges the noise magnitude is diminishing (Singh *et al.* [150]) 62

Figure 5.14 (top) photo of the arrangement of the ultra-high vacuum chamber to measure the angular current density (bottom) schematic showing a detailed configuration of the chamber 64

Figure 5.15 3D plot showing the variation of integrated intensity along semi-angles θ_x (along the x-axis) and θ_y (along the y-axis) for 50µm aperture 65

Figure 5.16 Plots showing the variation of angular current densities with applied voltages for different aperture diameters 66

Figure 5.17 Schematic of in-house built energy analyzer showing the electron beam crossing through different electrodes and only filtered out electron having reaching to detector....................67

Figure 5.18 Potential energy diagram of the energy analyzer showing the transfer of electron from the tip to analyzer E4....................68

Figure 5.19 Plot depicting variation in collector current with variation in analyzer voltage with respect to emitter voltage, red curve showing the theoretical fit that is in a good agreement with the experimental data 69

Figure 5.20 The total energy distribution (FWHM = 0.34 eV) of electrons emitted by the developed LaB_6 electron source. Theoretical model (Equation 5.5) fits (red curve) well with the experimental data (black dot)....................70

Figure 5.21 Increase in barrier slope with increase in applied voltage at constant work function and radius 70

Figure 5.22 Plot showing the energy spread profile at different voltage and emission current 71

Figure 5.23 Schematic showing Nottingham (heating and cooling) effect during electron tunneling of cold (blue dots) electrons and hot (red dots) electrons. At an equilibrium temperature T_{in}, electrons are released from fermi level and Nottingham effect vanishes. The extra energy carried by hot electrons (red dots) is released to the anode that act as a sink. 73

Figure 5.24 Field emission model of fabricated W and LaB6 tips 74

Figure 5.25 Plots showing the rise in apex temperature of W emitter (top) and LaB_6 emitter (bottom) during field emission and the blue and purple circles depicting the maximum emission currents before melting of tip starts, respectively 77

Figure 5.26 Plots showing that with same geometry for LaB_6 (black dot) and W (red dots), it is impossible for W to emit approximately 200 μA current before its destruction that LaB_6 can comfortably emit 78

Figure 5.27 Circuit diagram of in-house developed high voltage pulse generator used to produce (1-10) μs pulses 81

Figure 5.28 Illustration of the experimental setup used to generate and detect microsecond electron pulses 82

Figure 5.29 (top) Plot of data collected with oscilloscope showing 10μs pulse emitting 11μA peak current at 4.6kV peak voltage, (bottom) phosphor image of 10μs electron pulses carrying 11μA averaged over 1s time 83

Figure 5.30 Schematic of the setup to measure the angular current density for 10 μs electron pulse. The difference in this arrangment compared to measurements with continuous beam was the incorporation of pulse generator in place of continuous power supply and transimpedence amplifier aided oscilloscope in place of picoammeter 84

Figure 5.31 3D plot showing the variation of integrated intensity along semi-angles θ_x (along the x-axis) and θ_y (along the y-axis) for 200μm aperture. The peak current was 10-11 μA, at 4.5-4.6 kV peak extraction voltage was applied. The angular current density of 9.5 ± 0.1 μA/sr calculated from this plot shows no significant change compared to continuous field emission beam. 85

Figure 5.32 Schematic of the arrangement used to measure the energy spread of the generated μs electron pulses 86

Figure 5.33 Plots of the energy distribution of 10μs electron pulses emitted by the LaB_6 field emitter as function of energy with respect to Fermi level. A shift in the peak towards the low energy side is observed as the extraction voltage is increased. 87

Figure 5.34 A plot illustrating the relative peak position of the energy distribution of electrons emitted by the LaB_6 as a function of the extraction voltage. Unlike metallic emitters, a linear decrease in position is observed as the voltage increases. A linear least-squares fit drawn through the data points. The slope of the fit is −14.1 meV/V 88

Figure 6.1 Illustration of the lens effect of the tip apex that gives rise to the finite effective source size of $2r_{eff}$. The rearward asymptotic extension (dotted lines) of the electron beam rays from the beam spot is cross the Gaussian image plane at a distance of $2r_{eff}$ 94

Figure 6.2 (left) FEM of the 70 nm LaB_6 tip at 3600V. A single circular spot on the phosphor screen with (right) the Gaussian beam intensity profile (FWHM ~ 0.8 mm) indicates the Guassian nature of effective source. 94

Figure 6.5 The experimental arrangement of the point projection microscope with field emission tip generating electrons that are weakly scattered by the transparent or semi-transparent sample placed at distance *d* from the tip before reaching to the MCP-Phosphor assembly at distance *D* from the sample 96

Figure 6.6 Ray diagram of Fresnel diffraction in (left) point projection microscope, where the Fresnel fringes are formed directly on screen and (right) transmission electron microscope, where the fringes are formed at unit magnification on the focal plane of the objective lens and magnified by the subsequent lenses before detector 97

Figure 6.7 (top left) Photograph of in-house built point projection microscope having a nanotip and a μ-metal shield with sample loaded inside it, (top right) Photograph of sample holder showing quantifoil sitting in the middle of holder (bottom) Schematic of experimental setup shown with more detail 98

Figure 6.7 The magnified images of the features (in the ranges of several tens of microns to sub-micron) of quantifoil captured using PPM. (inset) showing the voltages at which images are captured. 99

Figure 6.8 Images captured at a) 61V & b) 54V, showing no fringes on decreasing the distance between tip and sample. Half-circular features were observed that might be due to image

artefacts or defects in quantifoil (No scale bar due to the absence of reference features in image). 100

List of Table

Table 1 Comparison of properties of the different electron sources used in commercial electron guns[52] [92][93][94][95][96] 20

Table 2 Statistics of the diameters of LaB_6 tips after electrochemical and subsequently FIB milling step. Out of 11 attempts to control the size in the narrow range of 70-80nm around 9 were successful. 54

Table 3 Parameters of W [177]–[179] and LaB_6 [180]–[185] used for simulating the temperature profile at the emitter surface 76

1 Introduction

All current scientific advancements are built on scientific progress across many centuries. One of the most significant technological achievements, from the author's point of view, is the discovery of electricity [1][2]. The human mind discovered electricity around 600 BC in the era of the ancient Greeks. They first described how rubbing a piece of *amber*, an organic extract of the trees, with *fur* brings an attractive force between them. However, the underlying reason on a mechanistic level remained a mystery for about 2000 years. In 1897, J. J. Thomson unravelled this secret by discovering a negatively charged particle known as the electron[3]. The transfer of electrons from *fur* to *amber* was the reason for the attractive force that Greeks observed many centuries ago.

Along with the elucidation of electricity, another field of research known as optics was emerging. Even with a complex cellular structure, the human eye is not capable of seeing smaller than 100µm and faster than a fraction of a second. This led the human mind to develop innovative tools and to touch new heights of human viewing capabilities. The first brilliant work in optics was documented by the Arabic scholar Alhazen in his '*book of optics'* at the end of the ninth century. He gave the idea of the rectilinear motion of light. With the developments of optical lenses in Europe, around the fourteenth and fifteenth centuries, the capabilities of the optical microscopy were recognized. Robert Hooke[4] and Anton van Leeuwenhoek[5] were one of the pioneers who pushed the limit of the viewing tool beyond the human imagination in that era. They invented the first generation of the optical microscopes. They presented the images of the blood cells, bacterias, bee's stings, and other microscopic objects to the world. Those inventions brought a revolution in the field of optics, and then researchers started to study the nature of light.

The double-slit experiment performed by Thomas Young[6] in 1801 changed the concept about the nature of light. He presented the phenomenon of diffraction (wave property) due to the interference of light and discarded the longstanding corpuscular theory of light proposed by Newton[7]. Later, it was realized that the wavelength of visible light (400nm-800nm) is not short enough to resolve the distances in the nanoscale regime[8]. This was the reason why applications of optical microscopy were limited to the study of the specimens in the µm size range. In 1895, W.Roentgen, a german scientist, discovered low wavelength radiation (1Å-10nm) known as X-rays[9]. Initially, these rays were solely used to diagnose dental problems. The real potential of X-rays was unravelled in 1912 by von Laue and later independently by W.L.Bragg by doing the famous X-ray diffraction experiment[10][11]. This experiment proved the ability of X-rays to investigate atomic length scales. After this discovery, X-rays have been ruled as one of the most desirable radiations to explore the nanoscopic world. In 1927, Davisson and Germer[12] confirmed the wave nature of an electron. It was the first evidence of the wave-particle duality, the concept formulated by de-Broglie in 1924[13]. After six years of this experiment, in 1933, Max Knoll and Ernst Ruska in Germany invented the first

electron microscope and succeeded in achieving sub-μm resolution. Further, improvements over the decades let the researchers to see the individual atoms in 1970[14]. The developments in the field of electron microscope opened up the door to a new branch of microscopy known as electron microscopy.

In the last century, significant developments occurred in X-rays and electron beam sources. Nowadays, these radiations are used as a probe in crystallography experiments[15][16][17]. More recently, researchers showed interest for electrons over X-rays as a probe, attribute to their 10^5-10^6 times higher cross-section, which is needed for more scattered signals[18]. Moreover, the availability of efficient, high-quality optics for electron beams, as featured in the transmission electron microscope (TEM), and the recent developments in high frame rate detectors enhanced the advantages of electrons over X-rays[19][20].

The methods of choice for structural studies in biology with electrons are cryogenic high-resolution single-particle microscopy (cryo-EM), tomography (cryo-ET), and nanocrystallography (NX)[21][22][23][24][25]. Cryo-EM involves the acquisition of high-resolution TEM images of an ensemble of vitrified individual molecules, followed by merging of the 100s to 1000s of individual particles in the image into a single high-resolution structure solution[23]. Cryo-ET uses the acquisition of multiple orientations of a single particle to reconstruct a 3D structure, and sub-tomographic averaging can further enhance spatial resolution, as long as conformational heterogeneity is low[24]. If nanocrystalline specimens are available, a tilt-series of nanobeam electron diffraction images can be acquired, providing sufficient sampling of reciprocal space to allow electron density map calculation[26][27][28]. Recent work by Bücker *et al.* on nanocrystallography in our group demonstrates the possibility of rapid high-resolution structure determination from a large ensemble of individual 3D crystals by dose and dose rate optimization using STEM[29].

While structures obtained from fixed specimens by single-particle microscopy or crystallography provide a wealth of high-resolution structural information, it is only direct *in situ* observations, where systems remain in their native, liquid environment, that can truly answer the questions of structure, dynamics, and function in real biological systems. *In situ* transmission electron microscopy is an emerging field that has been facilitated by recent advances in nanofabrication technology [30] with a resolution of a few nm possible[31]. A dynamically stabilized in situ flowcell technology has been recently developed by our previous group members[32]–[34]. However, radiation damage to the specimens through the necessarily high doses required (up to 10 $e^-/Å^2$ or more)[35][36], beam-induced specimen charging[18], and beam-induced motions of the specimen[37] are the most important factors limiting structural resolution in electron-based in-liquid imaging techniques. Direct damage to the sample can occur by chemical bond breaking due to inelastic scattering. Whereas, the indirect damage can occur through beam-induced heating or reaction of the specimen with free radicals[18][38]. While direct bond-breaking events occur instantly and depend only on the total electron

dose, specimen heating is a dose rate-dependent effect, and specimen reaction with free radicals may occur on significantly longer timescales.

The idea of exploiting the varying time scales of damage processes has already been demonstrated at the fs timescale in X-ray free-electron lasers (XFELs), where the "diffraction before destruction" approach has been successful in outrunning the Coulomb explosion of specimens due to ionization effects of intense X-ray pulses[39]. Ionization effects in the case of energetic electrons are quite different and do not result in the release of keV secondary electrons. Rather, damage occurs to a large extent by sample heating, chemical reactions with beam induced free radicals, and stresses due to bubble formation in vitrified specimens. In contrast to radiation damage by X-rays[40], the timescales on which these processes occur have not been studied in detail, but μs electron pulses will likely be short enough to at least partially outrun these damage mechanisms[41].

Attempts to understand not only the molecular structure but also the dynamics of chemical and biological processes have been a primary driving force for the development of ultrabright pulsed electron sources[42][43]. Efforts in dynamic real space imaging by electron microscopy in the subpicosecond regime have been championed mainly by Zewail[44], while Reed and coworkers have developed single-shot nanosecond electron microscopy with nanometer spatial resolution[45]. These studies were however conducted on inorganic materials, rather than radiation-sensitive biological specimens. In the femtosecond time domain, only the stroboscopic (pump-probe) approach can, in principle, achieve atomic resolution by working in the single electron per pulse regime at a high (MHz) repetition rate. However, this approach depends on the full reversibility of the process in question, such that the pump-probe cycle can be repeated millions of times on the same specimen.

Most biological processes are highly irreversible, implying the need for single shot, ideally movie mode that is, without the requirement of precise triggering acquisition schemes[45]. Limitations on electron source brightness and space charge interactions in the microscope column limit the attainable spatial resolution of dynamic transmission electron microscopes (DTEMs) to the 1-10 nm range if ns duration pulses are employed. For a high spatial resolution, of the order of 1 nm or less, the pulse duration requirements must be relaxed to the μsec regime or, equivalently, higher-brightness sources and space-charged optimized beamline designs must be employed. Tailored sequences of pulsed electron beams will allow better optimization of the tradeoff between fast acquisition times to eliminate motion-induced blurring and dose rate dependent sample heating. As certain radiation damage mechanisms occur on relatively slow timescales, i.e. in the ns or μs regime, sufficiently short pulses should allow outrunning these aspects of radiation damage[41].

An exciting combination of the in-situ flow cell technology with an ultrabright μs electron pulse source will, thus, allow investigating some interesting biological phenomenon which occurs at less explored μs-ms timescales. This thesis contributes to the development of such an ultrabright electron source and tries to show a path that can

meet the source requirements in the future. It is a well-established fact that field emitters are the brightest continuous electron beam sources available. However, this advantage comes either at the cost of rigorous vacuum conditions or low emission current or poor control over fabrication[46][47]. Due to this, search for a new field emitter is still on that can overcome these shortcomings, and hence more developments are needed in this area. Windsor [48] and more recent work by Zhang et al. [49] demonstrates that lanthanum hexaboride (LaB_6) based field emitters can survive in a relaxed vacuum environment (~10^{-9} mbar), unlike the commonly employed tungsten W. However, both of the researchers had to compromise either with less control over fabrication or with the low emission current. Additionally, the complicated, impractical transfer steps of electron source mounting overshadow the benefits of the material[49]. This motivated the author to develop a LaB_6 based bright field emission electron source which can be fabricated independently of the user skills and can meet the peak current requirements (discussed in Chapter 2) of the single-shot in-liquid imaging.

The current Ph.D. work is divided into three parts: theory of electron emission and state-of-art electron source, description of the developed setups to fabricate and characterize the electron source, and results. The second chapter is about the fundamentals of electron emission phenomena and the parameters used to quantify the quality of an electron source. At the end of the chapter, the requirements and the possible solutions for an electron source that may be used to study the structure and dynamics of biological samples are discussed. Chapter three is dedicated to the experimental setup established or used by the author to characterize the developed electron source. Chapters four to six presents the fabrication, measurements, and results obtained by the author. This includes the novel method of fabrication of the LaB_6 field emitter electron source and their surface study. In chapter five, a detailed characterization of the continuous and pulsed operation of our novel electron source is provided. The novel LaB_6 emitter developed in the thesis represents the main achievement of this Ph.D. work. Chapter six is dedicated to the development of a point projection setup to measure the brightness of the developed electron source. Preliminary results obtained with the point projection microscope are also included in this chapter. In the last chapter, number seven, the results are summarized, and an outlook of the project is discussed. Relevant simulation codes are attached as an appendix. The thesis ends with references and acknowledgements.

2 Electron emission processes and source characterization parameters: Theory

The seed of electron microscopy lies in the theoretical and experimental developments of electron emission phenomena[3][50][51]. The concept particle-wave duality of electrons, and its subsequent experimental verification[13][12], gave a treasure of ideas to the great minds of that era. The particle theory of electrons effectively describes emission and detection of electrons, and such aspects of interaction between beam and sample that give rise to energy loss and incoherent amplitude contrast. The wave nature of electrons becomes pertinent once the phase shifts suffered by the electron wave within the sample give rise to the image contrast, as in phase-contrast imaging and diffraction, which are the main modes of detection for biological specimenms at high resolution. For whatever purpose the electrons are used to study the samples, they need to be generated by the electron source. Some parameters determine the quality of an electron source, which makes it necessary to understand them and how they limit the performance of a microscope.

The theoretical discussions in this chapter are limited to the concepts and methods relevant to the experimental work described in chapters 4, 5, and 6. This chapter begins with section 2.1 explaining different electron emission mechanisms, the properties, and description of the physics behind the essential modes of electron emission. As the main focus of this thesis are field emission sources, factors affecting their operation like work function and field enhancement factor are introduced in more depth in section 2.2. Parameters like angular current density, effective source size, reduced brightness, and energy spread used to describe the quality of the electron sources are also included. Next, section 2.3 gives are more detailed comparison of all kinds of electron sources. The chapter concludes with section 2.4, which contains state-of-art developments in bright electron sources and much-needed electron source developments for phase contrast imaging of biological samples.

2.1 Primary electron emission mechanisms

There are three principle electron emissions processes – thermionic, photo-, and field emission – as well as common hybrids such as Schottky and photo-field emission. In this section, the thermionic emission is discussed briefly, then followed by Schottky emission, photoemission, and finally, the most relevant for this thesis, field emission.

2.1.1 Thermionic emission

Thermionic electron emission is the mode of electron emission in which the conducting emitter is heated to a high temperature (1700K-2700K)[52] so that due to the thermal energy electrons are able to cross the barrier (work function) and hence escape from the surface. The change in temperature directly impacts the emission current through the variation in the energy distribution of the free electron gas inside the emitter over the available states, as defined by Fermi- Dirac (F-D) distribution[53][54]:

$$f_{FD} = \frac{1}{1 + e^{\frac{E-E_F}{kT}}} \tag{2.1}$$

where E is the energy of an electronic state, E_F is the energy of the Fermi level, k is the Boltzmann constant and T is the temperature. From Equation 2.1, it can be easily estimated that as T increases from $T = 0$ K, energy states above the E_F start being populated. Electrons contained in the upper tail of the energy distribution, which may reach beyond the energy barrier height ϕ (work function) will be released into vacuum. The exponential dependence of electron emission current density on the emitter temperature was reported by Richardson in 1901 as[50]:

$$\mathrm{J} = A(1-r)T^2 \exp\left(-\frac{\emptyset}{kT}\right) \tag{2.2}$$

where A is Richardson constant and has value 1.204×10^6 A/(m^2 K^2), r is the reflection coefficient of the barrier for electrons, and T is the temperature at which emission is taking place.

Thermionic electron sources can provide beam currents in the microampere range and are easy to fabricate. However, due to the high thermal energy (1700 K – 2700 K) supplied to the lattice, the probability of electron scattering before being emitted is high, which leads to a random distribution of emitted electron trajectories[50]. Due to this, a high energy spread (1.5-3 eV) is observed for electrons emitted from thermionic sources[52]. Similarly, the lateral momentum of the emitted electrons is randomized (momentum spread), leading to low brightness, as will be defined below (10^5-10^6 Am^{-2}Sr^{-1}V^{-1}). Furthermore, they cannot provide electron pulses of the time duration better than milliseconds, due to the slow nature of thermal effects and hence author limited their discussion to this subsection.

2.1.2 Photoemission

Heinrich Hertz in 1887 experienced the enhanced sensitivity of his spark gap device by illuminating it with visible or UV light [55]. Soon after, in 1897, it was realized that the increase in sensitivity, observed by Hertz, was due to the emission of particles, named as electrons[3]. In 1902, Phillip Lenard put forward an incomprehensible result that the intensity of UV radiation does not affect the maximum kinetic energy of an

electron[56]. This remained a mystery until 1905, when Albert Einstein explained this phenomenon using his quantum theory of the photoelectric effect[51]. He proved that electrons are only emitted if the photon energy of the incident electromagnetic radiation reaches or exceeds a given threshold, the work function ϕ of the material. Also, by increasing the light intensity, only the number of emitted electrons increases, not their energy. This work bagged him the Nobel prize in 1921. He gave a relation between the maximum kinetic energy KE_{max} of the electron and the energy (hv) of the excitation radiation falling on a metal surface having work function ϕ:

$$KE_{max} = hv - \emptyset \qquad 2.3$$

Photoelectric emission is used by researchers for ultrafast time-resolved experiments and dynamic transmission electron microscopes (DTEM) [43][45][57]. It occurs because of the involvement of instantaneous energy exchange processes between electrons and electromagnetic radiation and the availability of ultrashort electromagnetic pulses (on the order of femtoseconds) from state-of-the-art laser sources. Although a larger peak emission current is achievable via photoelectric effect compared to thermionic emission and field emission, some limitations make them undesirable for biological imaging. While photo-gated planar and sharp tip cathodes are increasingly being studied with high power UV and visible lasers to achieve photo- and photo-assisted field emission[58][59], these sources are not suited to the generation of high brightness, high current, low energy spread beams with pulse durations in the ms regime, and optimized primarily for the fs temporal regime with 1-100 electrons per pulse[60][61]. Ultrabright emission fails for pulses longer than ps or ns in these devices due to thermal damage from the inevitably large trigger laser intensities[62]. Excessive energy spreads[63] and low peak currents from tip sources are additional concerns. Hence, photocathodes are not suitable for the ultimate goal of this thesis.

2.1.3 Schottky emission

Most high-resolution transmission electron microscopes (TEMs) or scanning transmission electron microscopes (STEMs) now fitted with either a Schottky or a cold field emission electron (CFE) source. This attributes to the superior brightness (section 2.2.3) of these sources compared to conventional thermionic sources. These sources have enabled routine atomic-resolution microscopy.

Even though often speciously considered, a Schottky source is neither a pure field emitter, nor is it a pure thermionic emitter, but rather a hybrid. A Schottky source in standard operation is a geometrically very sharp thermionic source where the effective work function of the material has been lowered by the applied electric field known as the Schottky effect (Figure 2.1). Despite the emission process being ultimately thermionic, Schottky emitters provide a vastly improved energy spread and brightness[64].

Unlike Schottky emitters, there are no high temperatures involved in operation of a cold field emitter (CFE). There, instead of having a tail of the electron energy distribution reaching over the emission barrier, electrons can tunnel through the barrier, which has been narrowed by the Schottky effect. The author thinks that it is important to go into more detail regarding the Schottky effect as this is not only important for the Schottky emitters but also for the cold field emitters, which are the gist of this thesis.

Figure 2.1 gives an illustration of the energy diagram for electrons near the interface of an electron source and vacuum while there is an electric field on the surface. To exit the emitter material, electrons must overcome an energy barrier called the work function, ϕ.

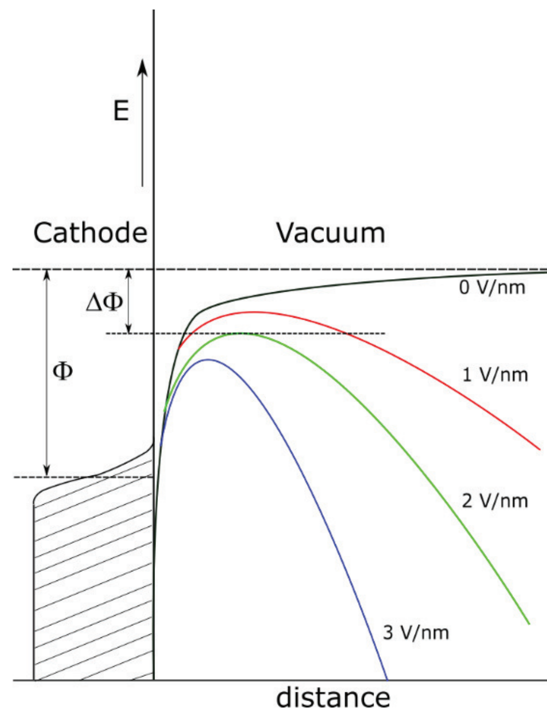

Figure 2.1 Schematic of energy diagram showing the (Schottky effect) bending of potential barrier at different applied fields (red, green and blue) compared to the absence of field (black line)

When an electron (-*e*) leaves the surface, it induces an image charge (+*e*) beneath it (Figure 2.2). This results in a layer of positive charge at the emitter surface. Hence, an electrostatic force F_{image} between charge and its image comes into play that can be written as:

$$F_{image} = \frac{(-\mathrm{e}).(+\mathrm{e})}{4\pi\epsilon_0(2x)^2} \qquad 2.4$$

This gives the corresponding image potential as:

$$V_{image} = -\frac{e}{4\pi\epsilon_0 . 4x} \qquad 2.5$$

To set itself free from the emitter surface electron must cross the potential barrier E_x resultant of the work function, the image potential, and the external field which can in total be written as:

$$E_x = \emptyset - \frac{e^2}{4\pi\epsilon_0\, 4x} - eFx \qquad 2.6$$

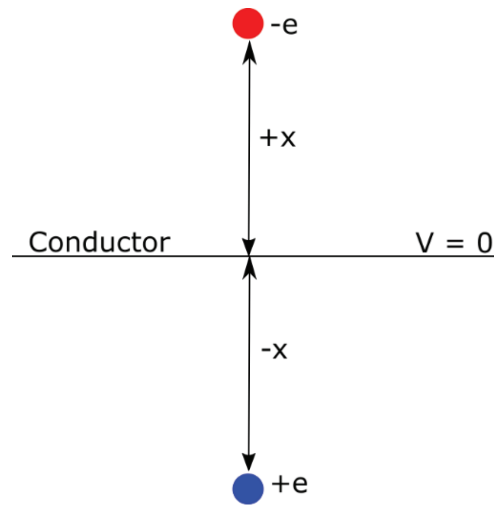

Figure 2.2 Diagram illustrating the concept of induced image-charge (+*e*) by the electron (-*e*), resulting in image charge potential

where ϕ is the inherent work function of the clean electron emitter. By finding the position x_m corresponding to the maximum value of the barrier E_x and substituting it in Equation 2.6 one obtains the value of the Schottky-reduced potential barrier or effective work function ϕ_{eff} :

$$\emptyset_{eff} = \emptyset - \sqrt{\frac{e^3 F}{4\pi\epsilon_0}} \qquad 2.7$$

Equation 2.7 gives a complete picture of how the Schottky effect reduces the work function. This effect aids in leaking out of electrons employed together with thermionic emission in the Schottky emitters. In recent decades, the integration of the Schottky

emitters has been increased in electron microscopes due to the rare combination of sufficient brightness, compatibility with state-of-art electron guns and less current fluctuations compared to thermionic, photo, and field emitters.

However, not every electron source can fulfil all the requirements of every experiment, and hence different emitters are used for different goals. As discussed in the introduction, the drive of this thesis is to develop a pulsed electron source that is optimal for high-resolution single-shot phase-contrast imaging applications[65]. This demands pulsing of the electron source. A reliable pulsed Schottky emission is not possible to achieve by regular switching off the extraction voltage. Schottky emitters require a particular field strength to maintain their tip shape, so dips in the field large enough to shut down emission would result in tip deformation. Moreover, to get a good on-off-ratio a very strong voltage pulse is needed as the quasi-thermionic current behaviour is much less steep than a cold field emission (see next subsection). Insufficient beam quality, such as brightness and energy spread of emitter are other concerns[66].

2.1.4 Field emission

As explained in section 2.1.3, the Schottky effect bends the potential barrier at the surface of metals. If the applied field is increased such that electrons start emanating without heating the surface, that emitter enters into a regime known as cold field emission or simply field emission. In this regime, the emission occurs through tunnelling from electronic states near the Fermi level through the barrier. This phenomenon was explained in the late 1920s by Fowler and Nordheim using quantum mechanics[46]. To establish reliable field emission concepts and theory, the following assumptions were made[67]:

a) All metals are assumed to obey the Sommerfeld free electron model with Fermi-Dirac statistics,
b) Only the planar geometry (1D) of the metal surface is considered to reduce the mathematical complexities,
c) Within the metal, the potential barrier is deemed to be constant for electrons,
d) Outside the metal, the potential barrier for electrons is assumed to be due to the image potential V_{image} (Equation 2.5),
e) The calculation for the cold field emission calculation was performed at T = 0K.

Under these assumptions, the current density J for field emitters is given by:

$$J = e\, v_x \int_0^{\infty} n(k_x)\, f(E) D(k_x) dk_x \qquad 2.8$$

where $n(k_x)$ is the number of states between k_x and $k_x + dk_x$, $f(E)$ is the F-D distribution of electrons at energy E and $D(k_x)$ is the tunneling probability.

Further developments by Stratton [68] and independently by Murphy and Good [69] led to the famous Fowler-Nordheim (F-N) equation for current density as:

$$J = \frac{1.54 \times 10^{-6}}{\emptyset t(y)^2} F^2 \exp\left[\frac{-6.8 \times 10^7 \emptyset^{3/2}}{F} v(y)\right] \quad 2.9$$

where $y = 3.79 \times 10^{-4} \times \frac{\sqrt{F}}{\emptyset}$, $t(y)$ and $v(y)$ are the correction terms included in the expression to incorporate the effect of V_{image}. Due to the weak dependence of the correction terms on y, it is justifiable to set them to unity[70].

Equation 2.9 can be written in a very simple form in terms of the experimental observables (current I, and applied voltage V) as:

$$I = AV^2 \exp\left[\frac{-B\emptyset^{3/2}}{\beta V}\right] \quad 2.10$$

where

$$A = \frac{1.54 \times 10^{-6} S\beta^2}{\emptyset\, t(y) d^2}$$

and

$$B = \frac{6.8 \times 10^7 v(y)}{\beta}$$

S is the surface area of the emitter, d is the distance between emitter and anode and β is the field enhancement factor that depends on the radius and geometry of the field emitter as discussed in section 2.1.5.2.

Equation 2.10 can be written as:

$$\log\left(\frac{I}{V^2}\right) = \log A - \frac{B\emptyset^{\frac{3}{2}}}{\beta}\left(\frac{1}{V}\right) \quad 2.11$$

A graph of $\log\left(\frac{I}{V^2}\right)$ vs $\frac{1}{V}$ gives a straight line with slope:

$$m = \frac{B\emptyset^{\frac{3}{2}}}{\beta} \quad 2.12$$

This plot is known as the Fowler-Nordheim plot or the F-N plot. Using Equation 2.12, the field enhancement factor can be calculated, and hence the radius of the tip emitter can be estimated to an acceptable accuracy.

In addition to some inherent properties of cold field emitters listed in Table 1, they have a combination of advantages that make them superior to the rest of the three modes of emission. On the one hand, the instantaneous nature (tens of attoseconds) of the electron tunnelling process [71] ensures faster response time of field emission compared to thermionic and Schottky field emitters due to slow thermal effects[72]. By using rapid electronic pulsing, the electric field can be turned on and off for µs–ns duration, and therefore shorter electron bunches can be created [73]. On the other hand, the smooth integration of field emitters with commercial machines makes them practical and promising candidates over photocathodes.

There are two crucial parameters of the field emitters on which the field emission current (Equation 2.10) depends. One is the work function ϕ, and the other is the field enhancement factor β. So it is essential to discuss these crucial parameters, as will be done in the next section.

2.1.5 Primary factors affecting the field emission operation

2.1.5.1 *Work function*

The work function of any material is entirely dependent on its surface conditions. The work function depends on two intrinsic factors and one extrinsic factor. One of the inherent factors is the characteristic inner potential that is the difference between the chemical potential of the electrons in the metal and that in a vacuum. Second is the anisotropy in atomic packing along the different orientations in a crystal. This anisotropy determines which orientation of a crystal must be used to fabricate the field emission electron source.

The concept of crystallographic anisotropy, as shown in Figure 2.3, was put forward by R. Smoluchowski [74] in 1941. At the densely packed face of any crystal, when there is no atomic layer present next to it, the potential that binds the electron to surface atoms would be less than the potential that binds them to atoms inside the metal. Hence, the wavefunctions of electrons present at these loosely packed faces are less concentrated inside the metal and are spread out in the vacuum to lower the energy. This spilling out of the electron wavefunction is termed as 'spreading'[74]. Because of this spreading of negative charge corresponding positive charge arises inside the metal side (Figure 2.3 b). This negative layer in vacuum increases the work function as it is an additional potential barrier that electrons must have to cross before leaving the surface.

On the other hand, at the loosely packed face of a crystal, the surface atoms and the gaps between two atoms make a rough structure of high surface energy (Figure 2.3 c). The electron starts to flow from the "hill" (surface atom) into the "valley" (gaps) to lower the surface energy. This flow of electrons was termed as 'smoothening' (shown by the dashed line in Figure 2.3) of the electronic cloud. This smoothening results in the

formation of electron-deficient "hills" and electron-rich "valleys"[74]. Due to the layer of a positive charge on the surface atoms (hills), the work function drops.

The planar density (PD) describes how closely packed a particular plane is. It is defined as the number of atoms per unit area that are present on a specific crystallographic plane. Robust metals like W and Mo used as field emitters have the body-centred cubic (bcc) structures. The order of PD in BCC is as follows:

$$PD_{(110)} > PD_{(100)} > PD_{(111)}$$

In terms of atomic smoothness, the (110) plane is the smoothest, and the (111) plane is the roughest. That is the reason why the magnitude of work functions is ordered as:

$$\emptyset_{110} > \emptyset_{100} > \emptyset_{111}$$

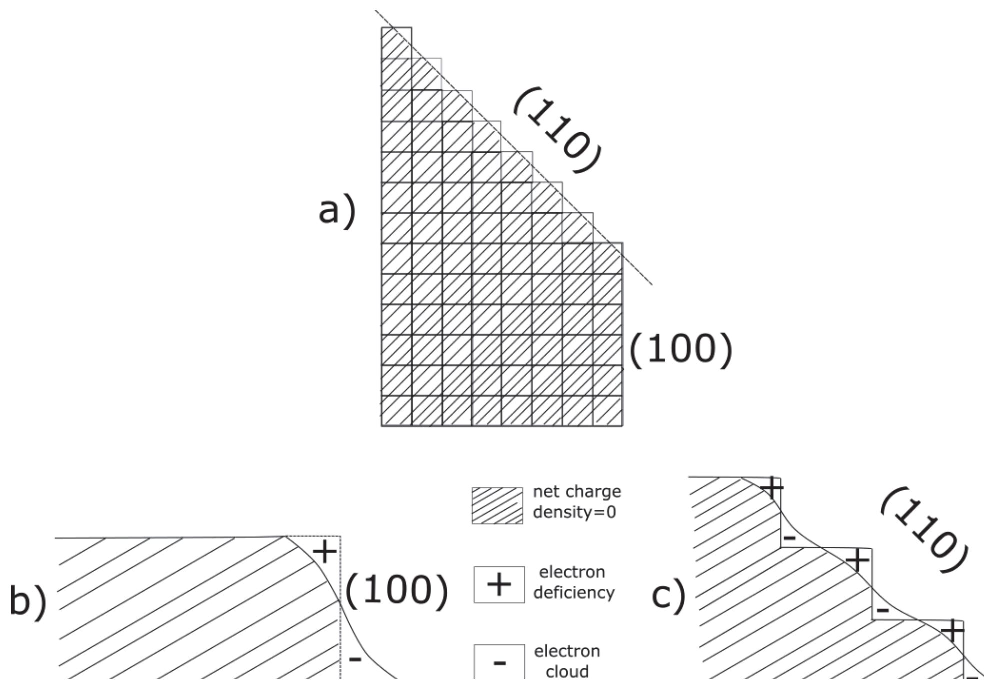

Figure 2.3 a) Smoothening effect and charge distribution at b) (100) smooth surface and c) (110) rough surface

This explains why most single-crystal field emitters are chosen to have a (111) orientation when there is the requirement of the high total current, due to the exponential dependence of current on ϕ (Equation 2.10). However, the advantage of the low work function of the (111) orientation comes at the cost of the high surface energy[74], which makes it unsuitable for a stable emission current. The (100) face is, therefore, the best

choice for the researcher that gives them an optimum combination of low work function and surface energy[75].

Finally, the extrinsic parameter on which the work function of any material depends is the dipole moment of the adsorbates covering it. The increase in the work function due to adsorption is given by[75]:

$$\emptyset_{ad} = \emptyset + g\pi\alpha F_0\sigma_0\theta \quad 2.13$$

where g is either 2 or 4, depending on the degree of proximity of the induced dipole moment resulting from the adatom or adsorbate, α is the polarizability of the adsorbates, $\sigma_0\theta$ is the adsorbate density on the surface and F_0 is the electric field at the adsorbate. The polarizability α can be written in terms of the induced dipole moment μ_{ind} as [75]:

$$\alpha = \frac{\mu_{ind}}{F_0} \quad 2.14$$

Hence, the direction of the induced surface dipole moment determines the decrement or increment of the work function due to adsorbate $\emptyset_{ad}$. When an electropositive adsorbate sits on the surface, μ_{ind} points towards the outward direction and hence there is a reduction in the effective work function and vice versa in the case of an electronegative adsorbate.

2.1.5.2 *Field enhancement (β) factor*

The field distribution around an emitter depends on its geometry. In the theory of field emission, the effect of the emitter profile is included using the β factor (Equation 2.10). The β factor depends on the shape factor k and the radius r of the field emitter as [75]:

$$\beta = \frac{1}{kr} \quad 2.15$$

The k factor of the emitter is dependent on two factors. First, the fabrication method that determines the initial shape of the emitter and second, the post-fabrication conditioning (thermal or field) that changes the emitter shape by surface diffusion processes [76][77]. The conditioning transports the mass towards or away from the tip apex resulting in blunting or sharpening of the tip, respectively[78]. However, the diffusion processes are dependent on the initial shape of the emitter that is determined by the fabrication method.

Dyke and Dolan gave an empirical relation for the *k* factor as [79]:

$$k = 0.5 \log \left(\frac{Cx}{r} \right) \qquad 2.16$$

where x is the distance between tip and counter-anode, $C = 1$ to 4 depends on the field emitter apex-shank shape and r is the radius of the emitter at the time of measurement.

2.2 Source parameters

It is important to know about the parameters that determine the quality of an electron source. This section begins with the notions of angular current density followed by effective source size and reduced brightness, then concludes with a short discussion of the energy spread.

2.2.1 Angular current density

The primary function of an electron source is to provide free electrons. Hence, the number of electrons per second, or current is an important quantity. However, as along the beam-shaping elements of a microscope, any electrons travelling at too large angles are removed, the practically more important property that is used to determine the electron source quality is the angular current density, that is, current per unit solid angle. By definition, this must be written as[80]:

$$J_a = \lim_{\Delta\Omega \to 0} \frac{\Delta I}{\Delta\Omega} \qquad 2.17$$

The above definition represents the mathematical limit of an infinitesimally small acceptance angle, which is not possible to measure experimentally. To overcome the ambiguity in the aperture sizes to be used in actual measurement, researchers [81] suggested using the solid angle defined by allowing half of the total current to pass. This methodology is used in this thesis work to measure the angular current density

2.2.2 Effective source size

Electrons emanating from the surface appear to have been emitted from an effective source or virtual source, which is obtained by back-tracing the trajectories of emitted particles, in analogy to a virtual image in ray optics. This virtual source will lie inside the emitter, and due to the strong lensing effect of the curved field outside field emitter[76] the axial position of the virtual source will shift strongly. In an electron beam instrument, the effective source size determines the extent of the coherence length of the

electrons at the sample, which is a significant determinant of achievable resolution. That's why the concept of effective source size is discussed below in detail, including the analytical and practical methods of measuring it.

To keep the mathematics simple without losing the generality, let us consider an emitter-vacuum planar boundary as shown in Figure 2.4. Analogous to photons, electrons also refract as they travel from one region (inside cathode) to another (vacuum) in the presence of applied potential[82]. At the interface, transverse momentum p_x (or velocity) remains conserved as no electric potential applied in the transverse direction. This gives:

$$p_x{}^{in} = p_x{}^{out} \tag{2.18}$$

By writing the transverse components of the total momentum in terms of the angle θ_{in} with which electron striking at the metal-vacuum interface and the angle θ_{out} with which electrons are emanating from the metal surface to the vacuum as:

$$p_{total}{}^{in} sin\theta_{in} = p_{total}{}^{out} \, sin\theta_{out} \tag{2.19}$$

A slight rearrangement in Equation 2.19 gives an expression equivalent to Snell's law used in light optics:

$$\frac{sin\theta_{in}}{sin\theta_{out}} = \frac{p_{total}{}^{out}}{p_{total}{}^{in}} \tag{2.20}$$

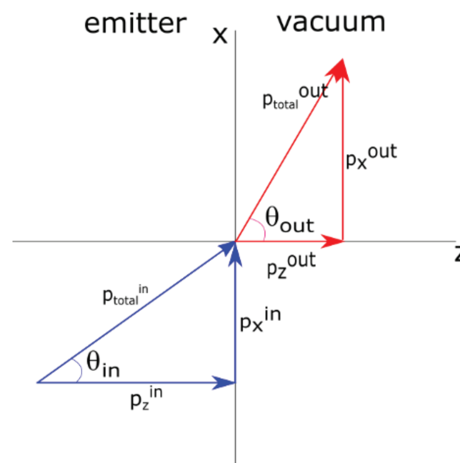

Figure 2.4 Illustration of electron momenta and angles at the emitter-vacuum interface during electron emission

The excitation energy E_{exc} used to emanate electrons from the surface can be a thermal, photo, or electrostatic potential energy. On assuming that an electron at a particular state has energy E, after excitation, the total energy of the electron increases to $E+E_{exc}$. However, to cross the emitter-vacuum interface, the electron has to cross a barrier of $E_F + \phi$. Hence, Equation 2.20 can be written in terms of energies as follows:

$$\frac{sin\theta_{in}}{sin\theta_{out}} = \frac{n_{out}}{n_{in}} = \sqrt{\frac{(E + E_{exc}) - (E_F + \phi)}{(E + E_{exc})}} \qquad 2.21$$

where n_{out} and n_{in} are the refractive indices of vacuum and interior of the emitter respectively. It can be perceived from Equation 2.21 that the emission angle θ_{out} is determined by the excitation energy E_{exc} and the emitter geometry plays no role in it. At a very high value of $E + E_{exc}$ compared to $E_F + \phi$, the square root term tends to unity, and hence emission angle θ_{out} tends to the value of incident angle θ_{in} of the electron. In other words, at very high excitation energy, no change in angles occurs at the interface.

The theory and the conclusion discussed above are valid for the emitter having the planar geometry. However, the result obtained in Equation 2.21 can also be used for the curved surface emitters. In the case of field emitters, the radius of curvature R of the emitter plays an important role. Due to the curvature, field emitter tips act as a lens.

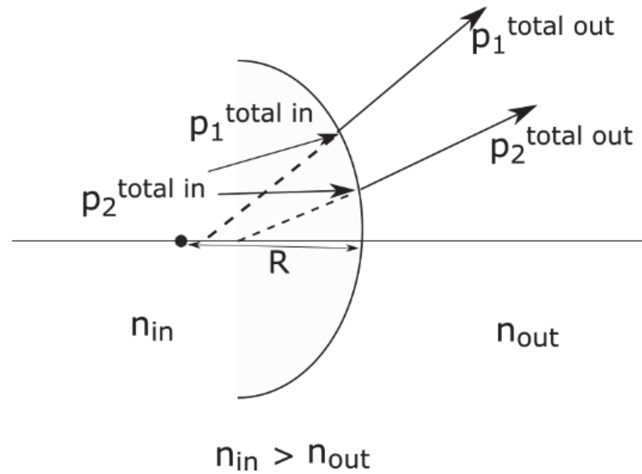

Figure 2.5 Refraction of electrons at curved boundary

The focal strength of any curved boundary is defined as[83]:

$$\frac{1}{f} = \frac{1}{R}\left(1 - \frac{n_{in}}{n_{out}}\right) \qquad 2.22$$

Using the result in Equation 2.21, the relation between the focal length, the radius of curvature of a field emitter, and the energies involved in the emission phenomenon can be written as:

$$\frac{1}{f} = \frac{1}{R}\left(1 - \sqrt{\frac{(E + E_{exc})}{(E + E_{exc}) - (E_F + \emptyset)}}\right) \quad 2.23$$

As the square root term will always be greater than unity, and hence the bracket term will always be negative. That's why the concave surface of the field emitters (negative radius of curvature *R*) always emit the electrons at diverging angles. The distribution in angles dependent on the focal strength that relies on the local field (or E_{exc}) distribution and ϕ (Equation 2.23).

The backward extensions (inside the field emitters) of the trajectories of the electrons leaving the field emitter tip at different angles do not meet at a point in the gaussian image plane [80] as shown in Figure 2.6. At the Gaussian image plane, the distance of the backward extended rays from the principal axis defines the effective source size r_{eff}.

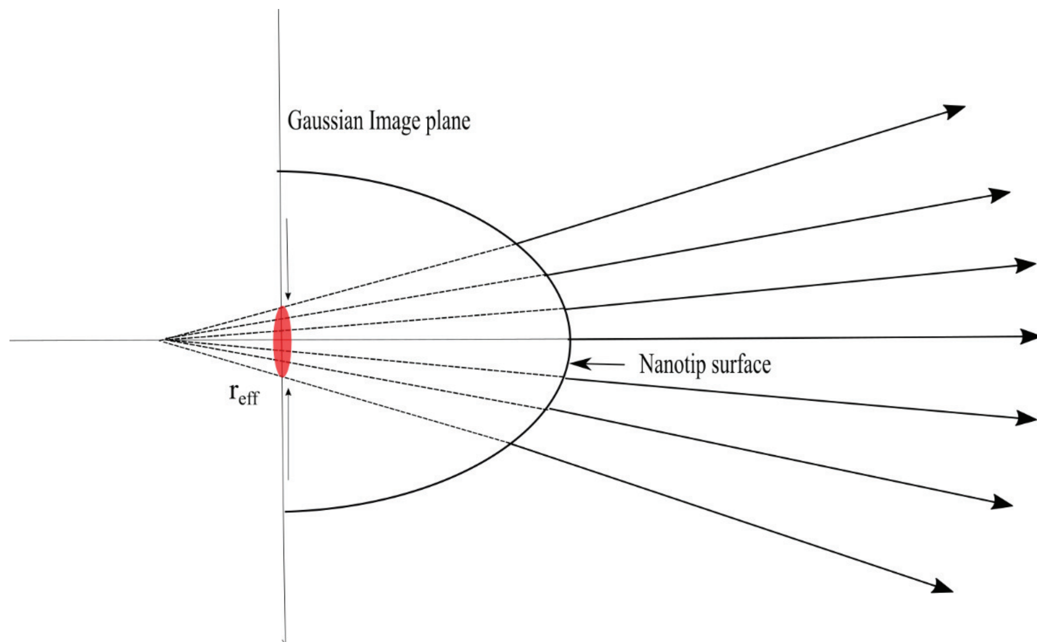

Figure 2.6 The backward extension of the trajectory of an electron are not meeting at the Gaussian image plane, but forming a disc of confusion r_{eff}

Usually, r_{eff} is measured by the ray-tracing simulation programs or by the point projection microscopy (discussed in 6.3). In general, r_{eff} is smaller than or equal to the physical source size[84]. However, one can find the limitation set by the Heisenberg uncertainty principle ($\Delta x \sim h/4\pi.\Delta p_x$) as suggested by previous researchers[85]. The term Δx is the uncertainty in position, so $\Delta x \sim r_{eff}$. The electron beam emanates out from the emitter surface with an angle θ_{beam} (Figure 2.4), this angle is commonly known as half opening angle of the beam. This angle can be determined by the beam diameter. The uncertainty in momentum along the x-direction can be written in terms of the half-opening angle as $\Delta p_x = p\, sin\theta_{beam}$. This gives, for a small half opening angle, the effective source size as[85]:

$$r_{eff} \sim \frac{\lambda}{4\pi\theta_{beam}} \qquad 2.24$$

2.2.3 Reduced Brightness

The reduced brightness of an electron source is defined as the angular current density J_a (or current density J) divided by the effective source area πr^2_{eff} (or solid angular area $\pi\alpha^2$) and acceleration voltage. Mathematically, it can be expressed as:

$$B_r = \frac{J_a}{\pi r_{eff}^2}\left(\frac{1}{V}\right) = \frac{J}{\pi\alpha^2}\left(\frac{1}{V}\right) \qquad 2.25$$

where α is the half-angle subtended by the source at the aperture or the sample. B_r is a conserved quantity and hence does not change with the acceleration/deceleration voltage in the optical column.

The beam brightness not only includes the information about the current I carried by an electron beam but also about its spatial coherence length L_c. Spatial coherence length L_c is defined as the distance over which the correlation exists between the phases of an electron wave at different points along the transverse direction of propagation. It is defined in terms of wavelength λ, and α as $L_c = \lambda/2\alpha$. For an electron beam of size σ carrying current I and coherence length L_c, the brightness (using Equation 2.25) can be written as [86][87]:

$$B_r = \frac{2me}{\pi^4\hbar^2}\left(\frac{IL_c^2}{\sigma^2}\right) \qquad 2.26$$

2.2.4 Energy spread

To describe an electron source, energy spread ΔE is one of the crucial parameters. During the emission of electrons, the slight difference in energies of the electrons can come due to the distribution of energy levels inside the emitter and local variation in the work function discussed in section 2.1.5.1. Due to energy conservation, this energy spread stays in the beamline even after the acceleration to a very high voltage. This energy difference can not be characterized by a single number but with a distribution of energies. The energy spread is determined by the full width at half maximum (FWHM) of the distribution by the reasearchers[88][89][90].

The initial energy spread can be increased if the stochastic interaction (Boersch effect) between electrons comes into the picture[91]. Due to the Boersch effect, some of the electrons in a beam are accelerated, and some are decelerated, which increases the width of the energy distribution. This effect is more prominent near the emitter surface, where the charge density is maximum compared to the other places in the optical column of the electron microscopes[91]. The space charge effects at lens crossover points are the other contributors which increase the energy spread.

2.3 Comparison of electron sources used in conventional TEM

The primary electron sources used in electron diffraction or imaging experiments are discussed in section 2.1. The characteristics of all the electron sources are shown in Table 1. It is clear from this comparison that the disadvantages of less current stability and very high vacuum requirement for field emitter operation are the primary hurdles which make them undesirable compared to Schottky- and Photo emitters. In the next section, the developments in field emitter over the last many decades are briefly discussed. Also, how field emitters with some advancements can fulfil the dream of single-shot phase-contrast imaging is included in the next section.

	Thermionic Emitters (W or LaB_6)	**Schottky Emitters (ZrO_2/W)**	**Photo-emitters**	**Field Emitters (W)**
Energy spread (*eV*)	1.5-3	0.7	0.3-1	0.2-0.3
Reduced Brightness ($Am^2Sr^{-1}V^{-1}$)	10^5-10^6	10^7-10^8	10-10^8	10^8-10^9
Current stability *(%/hr)*	<1	<1	1-20	5
Vacuum (*mbar*)	10^{-4}-10^{-6}	10^{-8}	10^{-8}-10^{-10}	10^{-11}
Lifetime (*hr*)	100-1000	>5000	2-1000	>5000

Table 1 Comparison of properties of the different electron sources used in commercial electron guns[52] [92][93][94][95][96]

2.4 Need for a new field emitter to fulfil the dream of single-shot high-resolution phase-contrast imaging

Crewe's development work in enhancing the resolution of the scanning electron microscope[97] was a turning point in the history of the electron microscope. He claims

that the resolution limit of an electron microscope can be pushed further by using the bright field emitter electron source. This claim motivated the researchers to develop new bright electron sources to unravel the mystery of the nanoscopic world. Different field emitters[98][99][100] were designed to compete with the classical W field emitter, but no significant advantages were observed in terms of vacuum conditions. However, at the end of the last century, the new developments in carbon nanotubes (CNTs) [101] field emitters took place[88][102][47]. They showed comparative or up to one order of magnitude higher reduced brightness than W field emitters (10^8 -10^9 $Am^{-2}Sr^{-1}V^{-1}$)[103] under somewhat relaxed vacuum conditions (10^{-9}-10^{-10} mbar). Unfortunately, even after showing promising characteristics, the CNT field emitters could not become the first choice for a commercial electron microscope. The reason is the poor reproducibility of the fabrication of CNTs. During fabrication, there are many possibilities of wrapping up of carbon sheets to form nanotubes[104]. The brightness and emission current of the electron source depends on its geometry, as discussed by researchers[105][106]. An electron source whose geometry is difficult or impossible to be controlled by the manufacturer is not worth using in the electron microscopes. Another reason is the complicated steps of transferring CNTs from the substrate to the commercial electron gun mount[88][103]. Recent success in controlling the growth of CNTs by Rao *et al.* [107] may open the door for this magic material as a reliable electron source in the future.

Recent developments in ultrafast femtosecond(fs) lasers and planar photocathodes[44][43] shows a path to the researchers to generate bright electron pulses from the field emitters. As discussed in Chapter 1, these bright pulses are always a pre-requisite for a high-resolution single-shot study of the radiation-sensitive biological samples[41]. As a result, photo-triggered metallic tips in the field emission[58][59] mode are increasingly being studied with high power UV and visible lasers used to photo-assist the emission. These sources are suited to the generation of high brightness, high current, low energy spread beams with pulse durations in the fs temporal regime with 1-100 electrons per pulse [60][61]. However, ultrabright emission fails for pulses longer than ps or ns in these devices due to thermal damage from the inevitably high trigger laser intensities[62], excessive energy spreads[63] and low peak current from tip sources are additional concerns.

This reveals the absence of a generation of bright field emitter electron sources that must have the following characteristics:

a) Stable operation in low vacuum condition (comparable to Schottky emitters) to avoid any increase in economic burden to upgrade the existing Schottky emitter gun,
b) Easy to reproduce with high control over fabrication. This will make easy tailoring of apex according to required emission current (see Equation 2.10),
c) Compatible with pulsed emission to generate the electron pulses in the ms-µs time regime according to the need of the user.

The first feature can be incorporated by using a robust and low work function material to fabricate the field emitter. The second characteristic condition can be fulfilled by developing a fabrication method for highly reproducible fabrication results. Using a classical method suggested by Dyke et al.[108] of electronic pulsing of extraction voltage of the field emitters, the third characteristic can be incorporated.

The last property will help in tailoring the duration of electron pulses as per the requirement of the application. However, the duration of a pulse set some limitations on the number of electrons (or current) carried by each pulse keeping the reduced brightness constant or vice versa. This current determines the dose and hence the spatial resolution of the image. Demanding single-shot acquisition with a detector resolution of 10 Megapixel (10^7 pixels) and an average number of electron counts of 10/pixel, allowing a signal to noise ratio of 3:1 in the presence of shot noise according to the Rose criterion[109], implies that a single pulse must deliver on the order of 10^8 e^-/shot on the sample.

In phase-contrast imaging, a critical parameter is the transverse electron coherence length L_c, which must be equal or larger than the smallest region of interest in the sample. On fixing the spot size equal to or greater than the lateral sample size, the required B_r value can be estimated using Equation 2.26. For example, to study the large scale conformational rearrangements associated with biological function in membrane proteins (1-10 nm), such as self-assembly, signal transduction, which are expected to occur on the µs-ms regime, beam size of 100 nm and the coherence length of 10 nm would give a good contrast. This sets $B_r \sim 10^8$ $Am^{-2}Sr^{-1}V^{-1}$ to achieve atomic resolution in phase-contrast imaging. Similarly, for *in-situ* liquid cell imaging, multiple scattering in thicker samples will limit L_c to about 2-3 nm[110]. A wider beam of the order of 10µm is needed in this case to capture the structure and dynamical movements of membrane proteins in liquid. These conditions fixed $B_r \sim 5\times10^8$ $Am^{-2}Sr^{-1}V^{-1}$. Pushing further this brightness value is not worth as the L_c for in-situ imaging is not source dependent but by the sample thickness.

3 Description of the relevant experimental setup, devices, and electronic circuit boards

In this thesis work, some setups were developed to fabricate and characterize the electron source. The author has been an important factor in the developments or modifications of all the systems used. The functionality of the fabricated electron sources was tested intimately by the author with the developed or modified setups. This chapter will give a general description of all the equipment (commercial and modified) used in the course of the current Ph.D. thesis work.

The first system in the list is the electrochemical etching set-up. The purpose of designing this scheme was to pre-etch the LaB_6 rod. This set-up was developed by the author together with Martin Kollowe, a senior engineer in the scientific support unit (SSU) team of the Max Planck Institute. The two generations of this set-up were designed in the present work. The reasons to develop the second generation of the set-up are described in the subsection of section 3.1.

The second system is the Focused Ion Beam (FIB) milling machine, used to thin down the diameter of the emitters to a few tens of nm after the electrochemical etching. This machine is present in the labs of our collaborators. Here the author would like to acknowledge the help of Professor Henry Chapman and Miriam Barthelmes (DESY, Hamburg) and for granting access to the FIB/SEM facility where the FIB machine is situated and for providing initial user training of SEM. Also, the author is thankful to Professor Rafal E. Dunin Borkowski's group (Forschungszentrum, Juelich) for providing the FIB facility for a week. A brief description of this set up is included in section 3.2.

The test chamber used to characterize the developed electron sources is described in section 3.3. The study of field emission property, angular current density, energy spread, and the electron pulses generated from LaB_6 emitter is performed with the test chamber. The internal modifications in the test chamber were made several times during this Ph.D. work and are described in chapter 5 and chapter 6. The development of this chamber was extensively performed by the author together with Djordje Gitaric (Technical Staff) and Hendrik Schikora (SSU team member).

The chapter ends with section 3.4 that describes the energy analyzer device designed for energy spread measurements. This device was developed by the author together with Josef Gonschior (technical staff) and the senior postdoctoral researchers of the group: Dr.Günther Kässier, and Dr.Robert Bücker.

3.1 Electrochemical etching set-up

The Lanthanum Hexaboride (LaB_6) rod was pre-etched to thin it down to few to tens of microns. Both 1st and 2nd generation of the electrochemical etching set-up design is discussed in the forthcoming subsections of the current section.

3.1.1 First-generation set-up

Figure 3.1 illustrating the schematic (left), and photograph (right) of the first generation of the electrochemical etching set-up

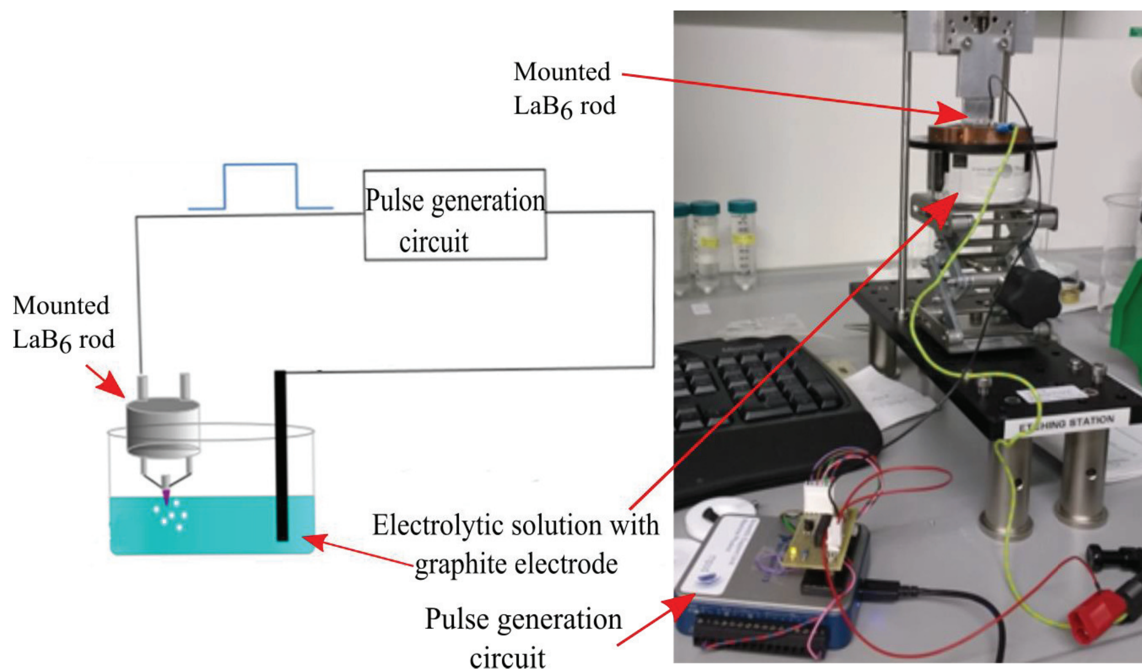

Figure 3.1 Illustration of the schematic (left) and photograph (right) of the 1st generation of electrochemical set-up during etching of LaB_6 rod

The schematic in Figure 3.1 demonstrates the electrochemical process of the LaB_6 rod immersed in a 30% phosphoric acid water-based solution (electrolyte). Graphite electrodes were used because of their chemical inertness to acid. Initially, DC voltage was applied to initiate the chemical reactions, but no sharpening of the rod was observed. Only a crowd of the bubbles around the rod was noticed. These bubbles are of hydrogen produced as a by-product in the reaction (see section 4.1.2). These hydrogen bubbles could not get enough time to escape from the surrounding of the rod and hence hindered the etching reactions. To avoid that, voltage pulses of magnitude 3-5V and time duration of 0.2-0.7 s with 1 Hz repetition rate were applied using a programmable circuit (NI USB-6000) purchased from National Instruments. The off-state of pulses provides enough time to hydrogen bubbles generated during on-state so that they can escape away from the surface of the LaB_6 rod. The sharpening of the rod was observed with this modification. However, the diameter never reached below 50-100 µm, even after many attempts and different combinations of pulse duration, voltages, and concentration of the electrolytic solution.

The possible reason could be the non-uniform concentration of oxonium (H_3O^+) ions and hydroxide (OH^-) ions along the LaB_6 rod immersed in the electrolyte. The rate

of etching of the La and B atoms depends on the concentration of oxonium (H_3O^+) ions and hydroxide (OH^-) ions, respectively. Similar failures in tungsten (W) tip fabrication due to non-uniformity of ions was observed by Chang *et al.* [92]. They addressed this problem by applying different pulse widths and got beautiful results with W.

In the LaB_6 case, the complexity was increased by its complex molecular structure compared to W. The fast and abrupt etching reactions are complicated to control. However, to control the reaction rate, the solution lift-up technique was used. This method is similar to procedures used by Ju *et al.* [93] and to do so, the second generation of electrochemical setup was designed.

3.1.2 Second-generation set-up

As mentioned in the last subsection that the complex molecular structure, differential ion concentration and fast chemical reaction rate could be the possible reason of tip breakage. So to avoid that, the second-generation electrochemical etching set-up was designed. The difference between first and second-generation setup was that in latter design, a fresh electrolytic solution was brought near to the tip for each etching cycle.

The procedure of converting LaB_6 rod of diameter 0.6mm to a diameter of few tens of micron is well described in Figure 3.2 a). A gold wire of thickness 0.5 mm was shaped into a 5mm diameter ring. This ring was attached to a programmable motorized stage. The speed of the stage was set in the range of 0.2 mm/s – 5mm/s to bring the electrolyte carrying gold ring near to the LaB_6 rod. The etching cycle started from the electrolyte beaker. A thin layer of the electrolyte was contained inside the grounded gold ring when carried out from the beaker by the motorized stage. After travelling a distance of about 5 cm, the ring touched the very end of the negatively biased LaB_6 rod. This completed the circuit and hence initiated the electrochemical etching process. The reaction was allowed to occur for 5-10 second. After that, the motorized stage brought back the ring in the electrolyte beaker and completed the etching cycle. This cycle continued for the next forty to fifty minutes, and then a sharp tip of radius 1-10 µm was obtained.

The thin layer of electrolyte assured that the reaction was limited only to the point of contact between electrolyte and rod. Unlike the first generation setup, the variation in concentrations of ions was then limited to the thin layer of electrolyte. This helped in controlling the reaction to some extent. The obtained tip was then transferred to the focused ion beam (FIB) machine, which is discussed in the next section. The detailed chemical reactions during the etching process are discussed in chapter 4 (see section 4.1.2).

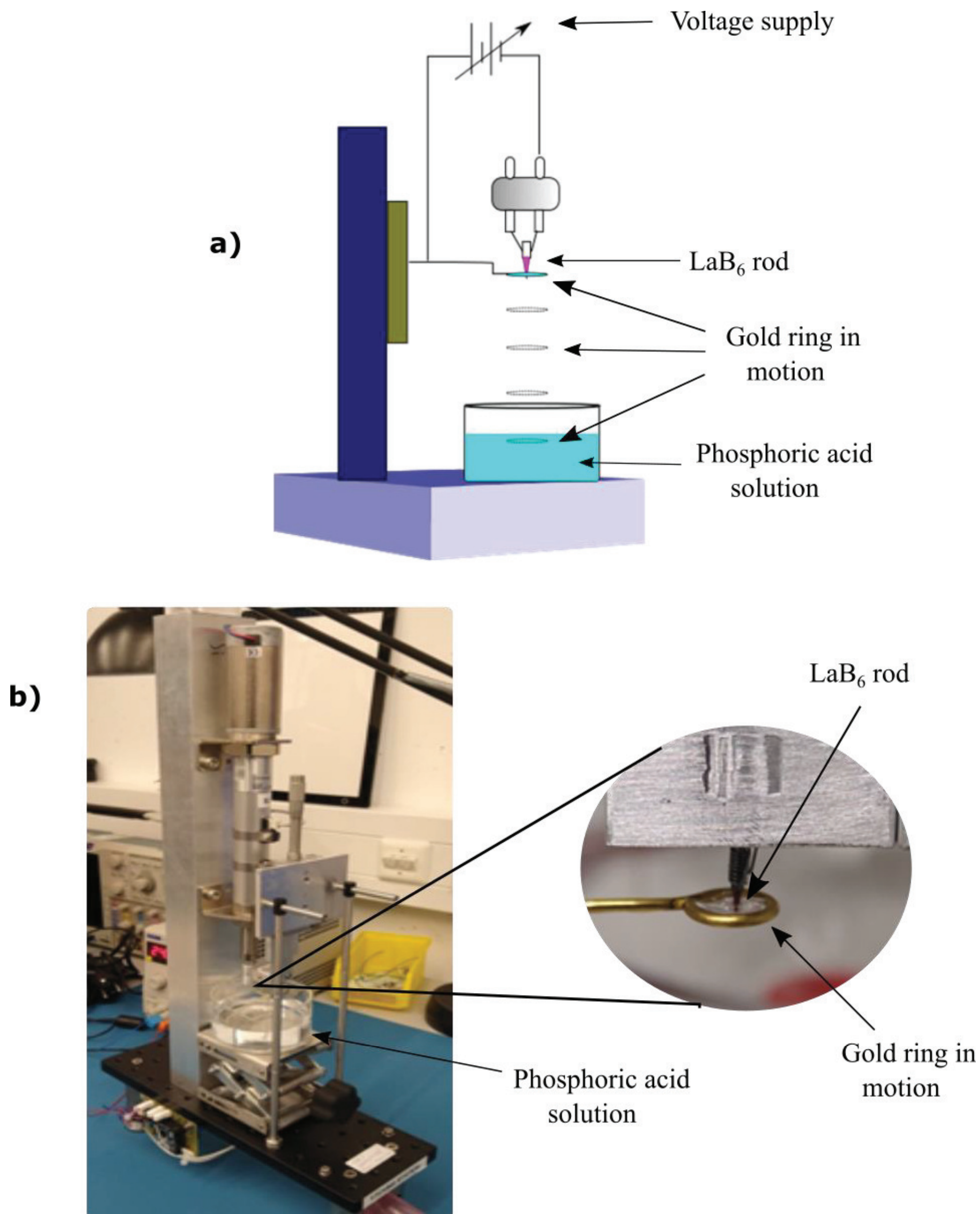

Figure 3.2 a) Schematic of the second generation electrochemical etching setup. A gold ring of 5 mm diameter was used to carry the electrolyte near to the rod. b) The photograph of the setup showing its different components c) An enlarged view of the LaB_6 rod dipping in the electrolyte carrying gold ring

3.2 Focused ion beam (FIB) machine

All the LaB_6 micro tips etched with the electrochemical etching set-up required further processing to bring their radius down to the sub-hundred-nanometer regime. This step was done using a Focussed ion beam (FIB) machine (Figure 3.3).

The sample (LaB_6 microtip) was mounted on a cleaned FIB sample holder. The principle operation of the FIB machine resembles the scanning electron microscope

(SEM). The FIB machine consists of an ion source (usually Ga), unlike an electron source in the SEM.

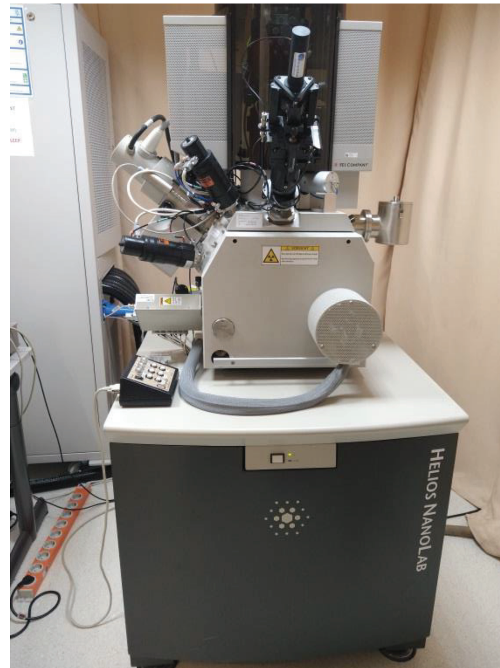

Figure 3.3 Focussed ion beam (FIB) milling facility in Prof. Henry Chapmann group used for sharpening the LaB_6 microtip in the current thesis

It uses a finely focused beam of ions to sputter/etch the surface of the target material. The size of the ion beam can be adjusted according to the feature size require on the sample. An *in situ* electron beam is used to monitor the surface of the target (Figure 3.4). The Ga^+ ion source used in the FIB machine (Helios NanoLab 600) has a very high resolution that allows milling down to 5 nm which makes it a powerful tool to modify the structure at the nanoscale level.

Another advantage of FIB milling is that no chemical reaction involves between the target and the etchant species. Due to chemistry independent, this milling method can be applied to pattern a wide variety of materials, including the compounds and alloys. The physics of the milling process is entirely similar to the sputtering. The directionality and applicability are two additional advantages of this technique which make it superior compared to the wet etching[111].

The directionality of the FIB is attributed to the fact that ions are accelerated in low chamber pressure by a strong vertical electrical field. As a result, atomic collisions are improbable, and hence ion's velocity with which they impinge on the surface of the target is entirely vertical. The sputtering rate of the different surfaces does not vary by much more than a factor of three[111]. Due to this ion milling is used prevalently for patterning ternary and quaternary systems like YBaCuO and InAlGaAs etc. These are the main advantages of FIB that motivated the author to use as a tool to mill down the LaB_6 microtip to less than 100 nm.

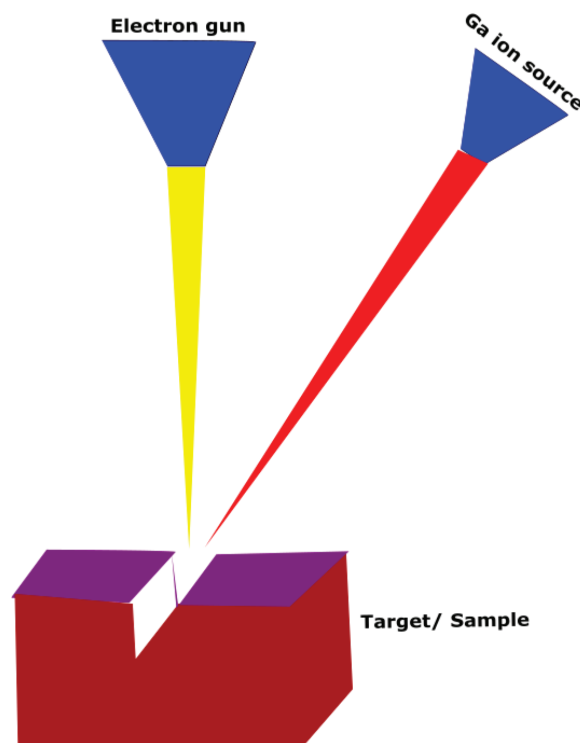

Figure 3.4 Schematic of the focused ion beam (FIB) milling process. An ion beam is used to modify the target surface and an electron beam to monitor the milling process.

The above advantages of the process come at the cost of a significant disadvantage: throughput. Combined with the low sputtering rate and need for a high vacuum, FIB becomes impractical to mill the large targets. In chapter 4, it is mentioned how the strength of the wet etching and FIB milling was used in this work to mitigate the weakness of these individual processes in the LaB_6 tip fabrication.

3.3 Test chamber

The test chamber acted as a spine of this whole Ph.D. work. Almost all the experiments were performed in this setup. An interesting historical fact about this chamber is that the pioneering work of Siwick *et al.*[112], on ultrafast melting of aluminium [112], was performed in a setup built around this chamber. This is a commercial vacuum product purchased from Kimball Physics Inc. The flanges of the same diameters are placed symmetrically by the manufacturer.

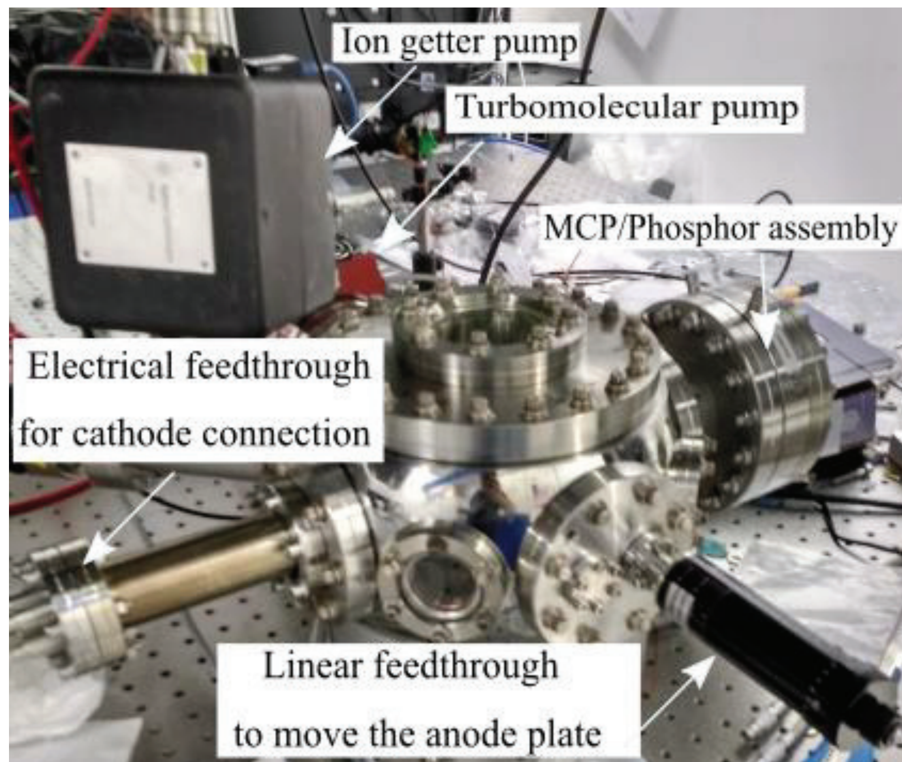

Figure 3.5 Photograph illustrating the different components of the test chamber used to characterize the fabricated electron (LaB_6 and W) source

As it can be seen from Figure 3.5, it has a circular shape and features four CF63 (one is hiding) and four CF36 (only one is visible) horizontal vacuum flanges. The top and the bottom flanges are circular CF160. The height of the chamber is about 120mm. Irrespective of which experiments were performed with this chamber, a few standard parts have always been part of the setup and will be enumerated here. The required vacuum is achieved by using a combination of turbo-pump (Pfeiffer HIPace 80) and ion getter-pump (Agilent VacIon 75 SEM). The turbo-pump and ion-getter pumps are mounted in parallel on CF63 and CF36 flanges respectively. A base vacuum level down to $5 \times 10^{-9} – 5 \times 10^{-10}$ mbar could be achieved after baking at 100-120 ºC, depending on the parts placed inside the chamber and the duration of the baking. The vacuum level in the set-up was monitored using a Bayard Alpart (hot-ionization) gauge purchased from Agilent.

The electron beam imaging was performed using a micro-channel plate (MCP), and phosphor screen assembly mounted on a standard CF100 flange purchased from MDC Vacuum. The CF100 flange has four high voltage (HV) feedthroughs with SHV connectors. Two or three of which were needed to power the MCP, depending on whether single MCP or chevron MCP was used. The fourth feedthrough being used to bias the phosphor screen. A rotatable extension tube was used to connect the MCP mounted CF100 flange to one of the CF63 flanges on the vacuum chamber.

The cathode or electron source was powered by the two-channel bipolar 6kV power supply (SHQ 226L) purchased from iseg. The voltage supplies (PS350 and PS365) purchased from Stanford Research Systems (SRS) were used to bias the MCP and phosphor screen. The voltage on the phosphor screen and MCP was never increased beyond 3.5KV and 700V respectively.

In the present work, the emission current measurements were done by using two means. The first method was the direct measurement using an anode plate connected to the pico-ammeter (Keithley 6487). The second method was the indirect measurement of current using the microchannel plate and phosphor assembly. In the calibration method, first, the current was measured directly by blocking the beam with the picoammeter connected anode plate. Then, the anode plate was removed from the beam path, and at different current values, a series of images of the beam spot on the phosphor screen was captured by the CCD camera. Using the image processing software (ImageJ), the current was translated into an average integrated intensity of the beam spot. This method was based on the assumption that no electron was lost between the anode plate and the MCP/Phosphor assembly. This assumption was very well valid in the test chamber as the distance between the anode plate and MCP/Phosphor assembly was kept only 3-5 mm. Furthermore, no other electrode was present between them.

3.4 Energy Analyzer

To experimentally realize the energy spread of the electron source developed in this Ph.D. work, it was necessary to design an energy analyzer. Its working principle was based on the retarding potential method[89][113]. Figure 3.6 depicts the design of the energy analyzer used. The schematic and operation of the analyzer are discussed in section 5.5.1. The design of this analyzer is motivated by Simpson's and Holscher's works[114][115]. However, it was modified according to the limitations posed by the limited space available in the test chamber and the compatibility of the electron source mount. All the four electrodes of the energy analyzer are made up of titanium. To electrically isolate them, all the electrodes are assembled using screws and spacers made up of polyether ether ketone (PEEK). It is a polymer with excellent mechanical and chemical properties. Its melting point is 343 ºC that helps to use it in an ultra-high vacuum (UHV) chamber that needs a baking process. The results of the energy spread are included in section 5.5.

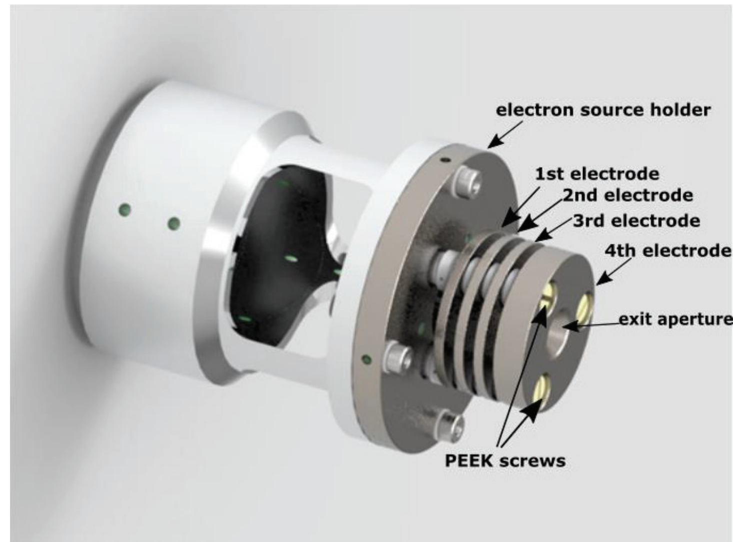

Figure 3.6 Illustration of the Computer-aided-design (CAD) of the in-house developed retarding potential energy analyzer. The schematic and working of this device is explained in chapter 5

4 Fabrication of Tungsten (W) Lanthanum Hexaboride (LaB_6) cold field emitter and their characterization

The first idea of using field emitter electron sources to be used in electron microscopes dates back to the 1930s when a student of physics at the Berlin institute of technology obtained high electric fields using metal nanotips. This student was later known as the father of field emission microscopes [55]. His name was Professor Erwin W. Mueller. To observe the mechanism by which the electrons are emanating from a sharp tip, he used a willemite coated glass bulb and applied an electric potential to the tungsten tip that was placed at the center of it. This was the first radial projection field electron microscope [56]. Mueller, in his lifetime, not only figured out the possible complications in the applications of the field emitters but also suggested some crucial solutions. He showed the effect of the cathode surface adsorbates on the field emission current stability and demonstrated that it can be avoided by heating or flashing the tip. Mueller further developed the field emitters and also suggested their wide applications e.g. field ion microscopy. The latter [57] is a technique in which an imaging gas is used to image the surface atoms of sharp conductive tips. In the previous studies concerning the cold field emitter sources, two essential results were demonstrated. First, the emitter source exhibits electrical stability in the sense that the relationship between the field emission current and the applied voltage remains unchanged with time, even at the emission current densities as high as 10^7 Amp/cm^2, provided that its surface can be maintained smooth and clean[108]. Second, techniques have been developed and used in field emission guns to maintain a clean and smooth emitter surface during extended operation[116]. The conditions for an excellent performance of the cold field emitters (W, Mo, Au, Ag, etc.) at emitted current densities in the order of ~ 10^7 Amp/cm^2, reduce in effect to a single requirement: an ultra-high vacuum (in the order of 10^{-12} mbar) must be achieved and also maintained during the operation. This has been obtained in the practical field emission guns by the effective evacuation using the modern vacuum pump technology. However, there may be some modern electron microscopes where the distinctive properties (high brightness, low energy spread, less energy consumption, etc.) of the cold field emitter sources could be used to advantage, but where the conditions for longevity and stability of the field emitters are not readily reconciled with a practical and economical design. The heated field emission cathode [117] or the "Schottky emitter" (Section 2.1.3) has been developed at a commercial level in the mid-twentieth century for use in such cases; as described in Section 2.1.3 it retains the essential properties and advantages of the field emission cathode. Also, it exhibits useful electrical stability at residual pressures (~10^{-9} mbar), but at the cost of the brightness of the field emission which is very crucial in the high-resolution phase-contrast imaging experiments and one of the requirements for the in-liquid single-shot experiment as discussed in section 2.4.

This chapter begins with the fabrication steps of W and LaB_6 emitters Section 4.1. In section 4.2, the surface studies of the fabricated LaB_6 tips are included. Section

4.3 concludes the chapter with the Gallium implantation issue and the surface damage due to the ion implantation is addressed. The W emitters were fabricated in Hamburg and the Universite Claude Bernard Lyon, France in collaboration with S.T. Purcell group. The electrochemical etching of the LaB_6 was performed on a home-built electrochemical set-up described in 3.1. The Focused ion beam (FIB) milling was performed in Hamburg in collaboration with Miriam Barthelemess (Henry Chapman group, DESY), and in Juelich with Maximilian Kruth (Rafal Borkowski group, Jülich Forschungszentrum).

4.1 Fabrication of emitters

4.1.1 Tungsten (W) emitter fabrication

The W emitters have consistently been one of the best choices for the field emitters ever since the discovery of the field emission. The reason for this is the inherent properties of the W - it is the hardest of all the metals as well as being a refractory material (with a high melting point of about 3600K)[118]. Well-established fabrication steps of the wet etching protocols for tungsten emitters abound in the literature[119],[120],[121],[122],[123],[124]. In this thesis work, we implemented the classical electrochemical etching method of the W tips [10].

A 0.125mm diameter, 5mm long tungsten wire piece was spot welded on a wedge shape of a tantalum wire using a welding station (Figure 4.1).

Figure 4.1 Photo of the spot-welding machine in S. T. Purcell group in Lyon, France

The legs of the tantalum wedge are then spot welded on the pins of a ceramic mount (Figure 4.2 a) & b)). After mounting the Ta wire carrying the W wire, the mount was fixed on the electrochemical etching station (Figure 4.3). The electrolytic solution was prepared in two simple steps. First, 1M NaOH aqueous solution was prepared by mixing 4g of sodium hydroxide granules in 100mL of deionized water. Subsequently, 60mL of prepared 1M NaOH solution was mixed with 40mL glycerol to prepare a 100mL electrolytic solution. The primary reason for using glycerol is to increase the viscosity of

the electrolytic solution, which helps to form a stable meniscus and etch the W wire smoothly to a fine W tip as observed by the researchers with gold tip etching[125].

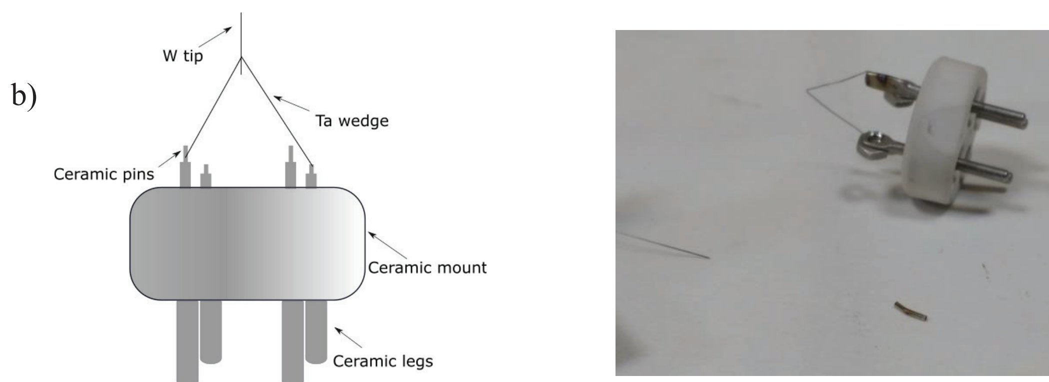

Figure 4.2 a) Schematic of tungsten (W) wire mounted on a ceramic mount, b) Photo of Tantalum wedge welded on ceramic to make an electrical connection between W wire and ceramic legs or pins

Using the translation stages, 0.2-0.5 mm of the electrically grounded tungsten wire was immersed in the solution and the D.C voltage (3-5 V) pulses were applied on the counter electrode.

The following reactions take place:

At the anode:

$$6H_2O + 6e^- \longrightarrow 3H_2(g) + 6OH^-,$$

At the cathode:

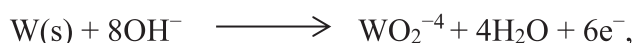

$$W(s) + 8OH^- \longrightarrow WO_2^{-4} + 4H_2O + 6e^-,$$

Although electrochemical etching takes place over the entire surface of the immersed tungsten wire, the reaction near the surface of the electrolyte solution is crucial to fabricate a sharp tip. The meniscus of the solution around the tungsten wire plays an important role in determining the final shape and aspect ratio of the emitter tip apex[126]. Since the OH^- ions concentration near the top of the meniscus is lower than that of the bulk electrolytic solution, the etching rate decreases along with the meniscus. On the other hand, the etching process of the tungsten wire produces soluble tungsten anions (WO_2^{-4}) that migrate downwards along its surface. This layer of the tungstate anions over the immersed tungsten wire hinders the etching of the immersed wire below the meniscus, causing the etching rate to be reduced for the lower portion of the wire.

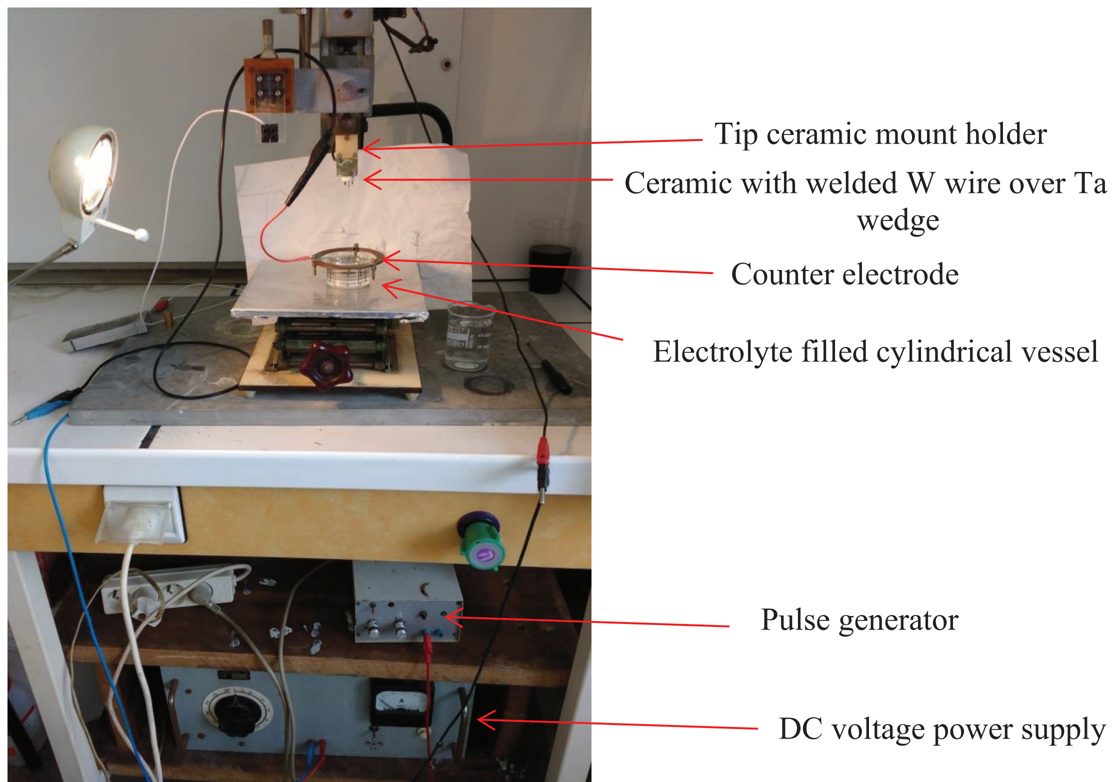

Figure 4.3 Snapshot of Electrochemical etching set up in S.T. Purcell group in Lyon showing electronics (labeled) associated with the setup

As a result, a "neck-in" phenomenon occurs close to the bottom of the meniscus, where the etching rate is the highest. When the tensile strength cannot sustain the weight of the immersed portion of the tungsten wire, a "drop-off" occurs. The tungsten probe with a sharp tip is then located at the breaking point.

The electrochemical reaction is the consequence of the flow thickness gradient along the axial direction, and it is substantial in the meniscus area. The gradient of the flow thickness and streamline of the anodic flow define the profile and tip apex radius of the probe[127] as shown in Figure 4.4.

Another etch parameter that is usually varied is the length of the wire immersed in the electrolyte. It was found by lbe *et al*.[128] that this parameter has a direct effect on the tip geometry, with greater lengths causing the stub to drop off much sooner due to the increased weight. Since the drop off occurs when less of the wire has been etched away, these tips have a correspondingly larger radius of curvature [119].

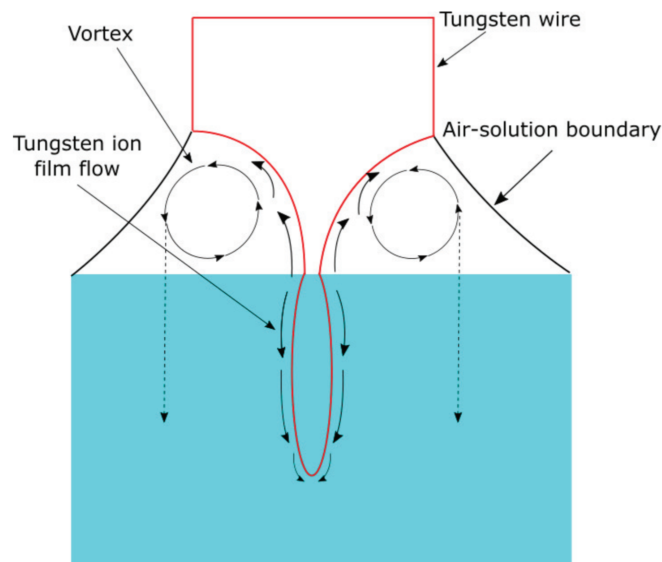

Figure 4.4 Schematic of the vortex flow during the electrochemical etching that regulates the flow of the tungstate ions and determines the shape of the tip

In this thesis work, the tip profile was changed by controlling the immersed length of the tungsten in the solution. As shown in the scanning electron micrographs (SEM) (Figure 4.5 a) and b)), two tips of the different profiles were fabricated using immersion lengths of 1mm and 0.5 mm, respectively. It can be seen that the tungsten wire immersed deeper in the solution yielded a completely different tip in terms of the radius of curvature as compared to the tip having less immersion length. Although the tip with a small radius of curvature would start to emit at a lower voltage as compared to the tip with a large radius of curvature, the emission current from the former is more limited by its comparatively high electrical resistance.

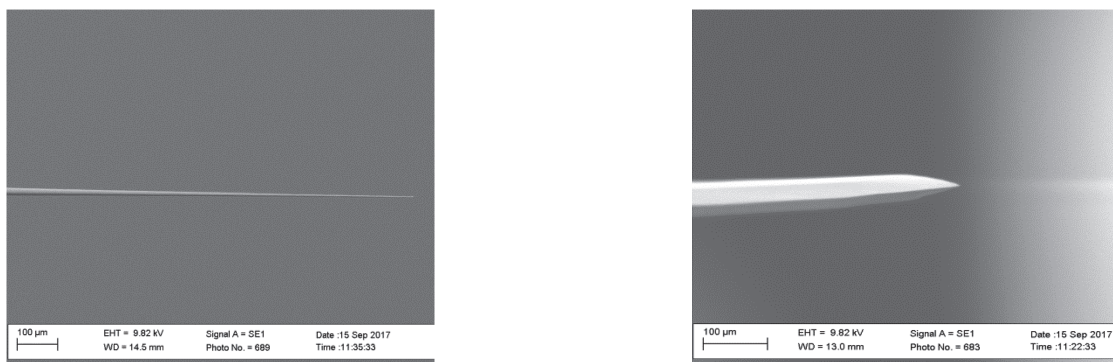

Figure 4.5 Tungsten tip fabricated by immersing tungsten wire a) 0.5mm and b) 1mm in an electrolytic solution (1M NaOH)

Due to the resistive current limitation, these tips exhibit a very low emission current in the few hundreds of pico-amperes (pA) range, typically 200pA-400pA. On the other hand, tips with a low radius of curvature as shown in (Figure 4.5 b)) can emit current around 10-20 times more than the former. Field emission measurements of the fabricated W tips are presented in section 5.1.

4.1.2 Lanthanum Hexaboride emitter fabrication, challenges and solution

Lanthanum Hexaboride (LaB_6) is one of the intermetallic compounds which has been used as a thermionic electron emitter[129] for many decades. LaB_6 is a refractory material forming a simple cubic lattice (shown in Figure 4.6) in the space group O'k – Pm3m. It shows metallic conductivity and has been one of the most widely used thermionic electron sources in a large variety of devices.[64]

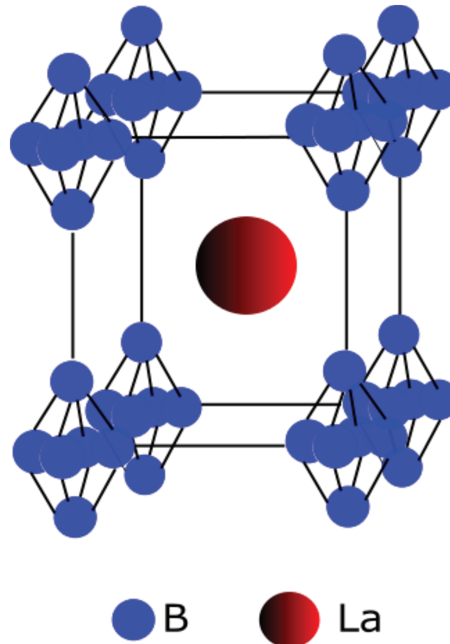

Figure 4.6 Simple cubic structure of Lanthanum Hexaboride (LaB_6) with one Lanthanum in the middle surrounded by Boron octahedra structures

Its inherent properties of low work function (2.7eV), low vapor pressure[130], chemical inertness[131] and high mechanical robustness [132] would make it a superior field emitter as compared with the W in transmission electron microscopy (TEM) and scanning electron microscopy (SEM) applications. Earlier work in the LaB_6 tip preparation has included electrochemical etching to produce the field emitter arrays (FEAs) [133], the CVD method[131] to fabricate the LaB_6 nanowires and the metal flux techniques[132] to yield the single tips. However, complexities in these methods make them time-consuming as well as challenging to use as practical field emitters due to many transferring steps from fabrication to mounting.

The LaB_6 rods of diameter 0.60 mm and 5mm long, <100> direction oriented were purchased from APTech. The <100> alignment is chosen because of its low work function and volatility compared to the other orientations[134]. Direct welding of the LaB_6 rods with W wire was attempted but resulted in shattering of the LaB_6 rod due to their low ductility. This made it challenging to fix the LaB_6 rods on the commercial ceramic mounts. The LaB_6 holder made of a material having a melting point higher than the LaB_6 with the high thermal conductivity for flashing of the LaB_6 tips was required.

Another demand made on the material was high ductility such that it can be welded to the ceramic pins and have a similar thermal expansion coefficient as that of LaB_6.

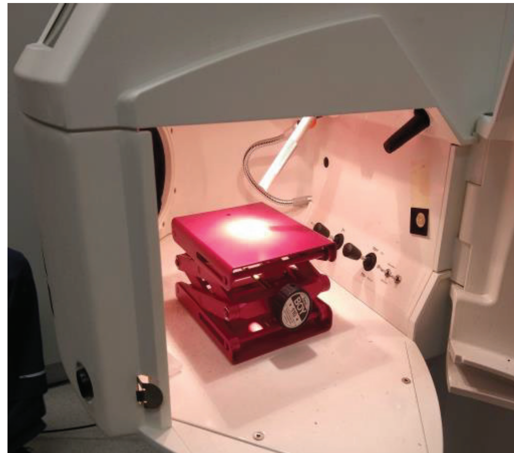

Figure 4.7 The photograph showing inside view of the laser welding facility located in the University of Hamburg workshop located on the DESY campus

This is so that during flashing at high temperatures, the LaB_6 does not detach from the holder or shatter due to the difference in expansion. Tantalum is a material that fulfils all these requirements. Tantalum (Ta) tubes 10 cm long with an outer diameter of 0.8 mm and an inner diameter of 0.7 mm were purchased from Goodfellow and cut into 6mm long pieces. From one end, the Ta tube piece was divided symmetrically (2mm along the length) into two semi-cylindrical shapes. The LaB_6 rod was then inserted in between the semi-cylindrical part and pushed manually to another side (full cylindrical part) of the Ta tube such that only 2mm of LaB_6 rod remained outside of the semi-cylindrical part. The semi-cylindrical piece was then wrapped and welded with the W wires to hold in the direction perpendicular to the surface of the ceramic plate with firm support. These W wires were then spot-welded using the laser welding (Figure 4.7) on the legs of the ceramic mount (Figure 4.8). The laser welding facility was provided by the University of Hamburg workshop located on the DESY campus.

The mounted LaB_6 was then fixed on the electrochemical polishing set up (Figure 3.2). Wang *et al.* demonstrated the electrochemical etching of the LaB_6 single crystal field emitter arrays (FEA)[135]. Although the same etching process was employed, some optimizations were required to decrease the diameter of one end of the LaB_6 rod from mm range to µm range such as variation of the etching parameters (e.g. electrolytic solution concentration) and the variation of the DC voltage pulse width. Initially, the electrolyte was prepared using 30% phosphoric acid and 15% glycerol in the water. Then the concentration of the phosphoric acid is reduced to 5% in steps while maintaining the same glycerol concentration.

Because of the complex molecular structure of the LaB_6 compared to the metallic field emitters, it is challenging to shape it using a simple electrochemical etching technique. To date, only one article in the late 1970s was published regarding

electrochemical etching of lanthanum hexaboride [136]. Local humps were observed on the fabricated tip, and it was argued by the author that those humps were due to the

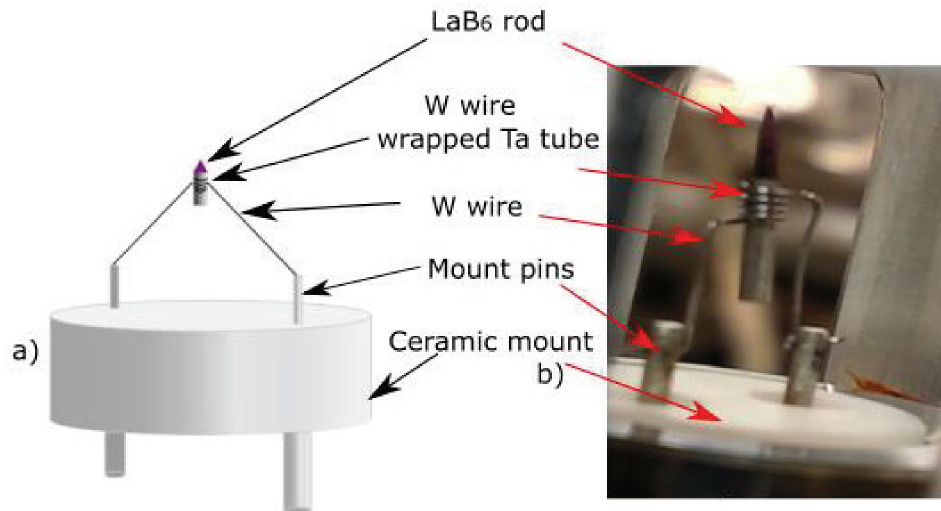

Figure 4.8 a) Schematic and b) photo of LaB_6 mounting assembly showing LaB_6 rod inserted inside the W wrapped Ta tube

stoichiometric changes in the emitter surface. It was claimed that those stoichiometric changes were due to the non-uniform thermal evaporation of surface atoms. This might be possible due to the high temperature (above 1600 ^{0}C) flashing used by them to clean the LaB_6 surface. To the best of the author's knowledge, at the time of writing this thesis, there is no published article on the fabrication of LaB_6 based single tip field emitters from an mm size rod (top-down approach). The results showing stoichiometric changes in lanthanum hexaboride right after electrochemical etching as well after FIB milling are presented in section 4.2.

To understand the complexities of the etching process of the LaB_6 its reaction process must be understood. On immersion in the electrolytic solution, the following reactions take place:

Due to the positive potential, the anode (graphite electrode) dissociates the phosphoric acid into the oxonium (H_3O^+) ions and the phosphate ions[137].

$$H_3PO_4 \longrightarrow 3H_3O^+ + PO_4^{3-}$$

The negative potential at the cathode (LaB_6) attracts the positively charged oxonium ions resulting in the lanthanum ion formation. In the presence of the excess water, the lanthanum ions form lanthanum hydroxide and hydrogen. As a by-product, hydrogen evolves in the form of bubbles as shown (Figure 4.9)

$$La + H_3O^+ + 2H_2O \longrightarrow La(OH)_3 + H_2 + 2H^+ + 2e^-$$

Figure 4.9 Photograph showing Hydrogen bubbling around the LaB_6 surface on reacting with phosphoric acid

Simultaneously, upon coming into contact with water, boron produces boron hydroxide, also known as the boric acid (H_3BO_3) around the tip apex.

$$B + 3H_2O \longrightarrow H_3BO_3 + 3H^+ + 3e^-$$

The boric acid then reacts with the phosphoric acid, and a white layer or particles of the boron phosphate (BPO_4) appeared around the tip. A white particle around the tip can be seen in Figure 4.10.

$$H_3PO_4 + H_3BO_3 \longrightarrow BPO_4 + 3H_2O$$

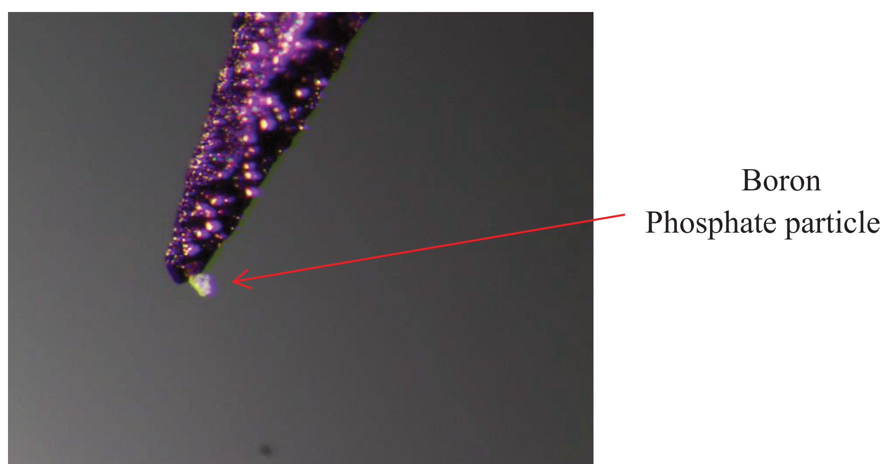

Figure 4.10 Optical microscope image showing boron phosphate particle around the tip, uneven bright and dark spots are due to uneven surface resulting in partial shadowing

The right-hand rule states that the higher (positive) value of the electrochemical potential of an element shows the less chemical reactivity (or nobility) of the element [138]. The electrochemical reduction potential of the lanthanum is more negative (E_0 = -2.38 V) than that of boron (E_0 = - 0.89 V) [137]. Due to which, the phosphoric acid

dissolves the lanthanum in a larger proportion in comparison to the boron, which brings in the stoichiometric inhomogeneity as observed by the previous researchers[136].

On using the DC voltages with the 1st generation electrochemical etching set up, *in-solution etching mode* (Figure 3.1), no etching was observed. This leads to the conclusion that DC voltage is not suitable to etch the LaB_6 tips. The reason could be that due to the continuous production of the hydrogen bubbles, the oxonium (H_3O^+) ions and phosphate (PO_4^-) ions (Figure 4.11) have insufficient time to dissociate the lanthanum and the boron respectively.

To address this problem, the 2nd generation electrochemical etching set up (Figure 3.2), was developed. To provide sufficient time of reaction and to avoid the pile-up of oxonium and phosphate ions around the tip, D.C. voltages pulses (3-6 V) were applied using a pulse generator. The rectangular pulses of width 200ms were employed with a repetition rate of 1 Hz. Initial etching of the 0.6mm LaB_6 rod started with 6V pulses. After 20 minutes, a reduced diameter (around 0.2mm) of the rod could be observed through the eyes. At this point, the voltage amplitude was reduced to 4V for the next 5 minutes. To give it a final shape, the tip was etched at 3.4V for 5-10 minutes, and then a sharply pointed apex of diameter 1-10 µm was obtained (Figure 4.12(left)). To avoid further etching of the apex, which results in a blunt end tip, the electrochemical etching process was observed continuously and stopped as soon as the apex is observed(Figure 4.12(right)).

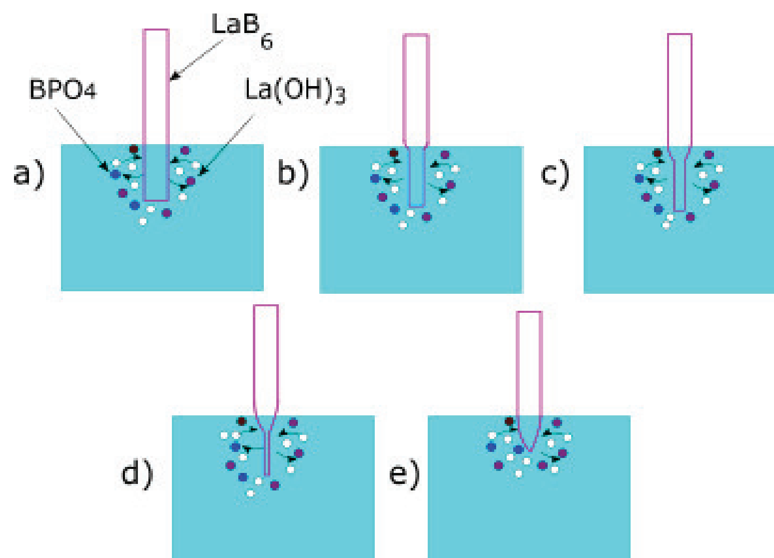

Figure 4.11 Schematic showing the immersed LaB_6 in electrolytic solution a) that results in the formation of boron phosphate (BPO_4) and Lanthanum hydroxide ($La(OH)_3$), intermediate steps b), c) d) shows the thinning down of the tip apex resulting into 1-10µm sharp tip e)

As mentioned in 4.1.1, the immersion length of emitter material determines the tip shape. The author found 0.5mm to be the most optimized immersion length for LaB_6.

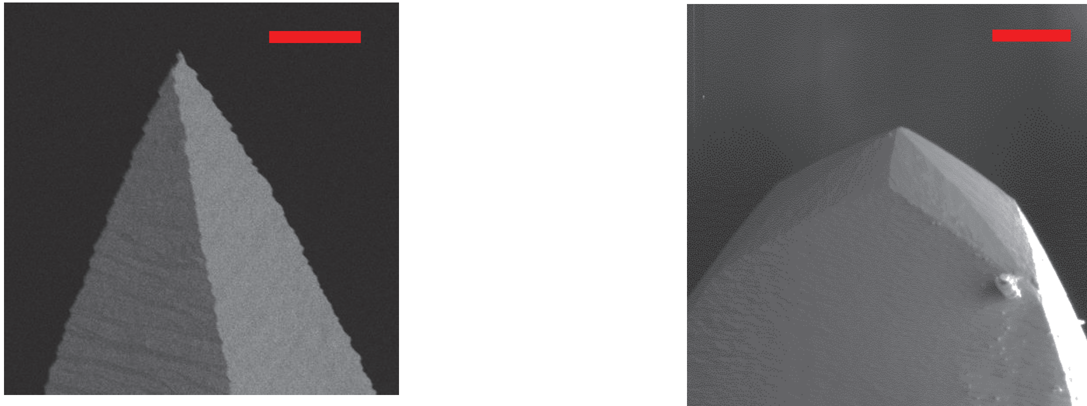

Figure 4.12 SEM image showing the morphology of LaB_6 electrochemically etched emitters with 40 minutes (left) and 60 minutes (right). (Scale bar represents 20μm) (Images were captured by the author in Henry Chapman's FIB/SEM lab located in CFEL)

The mechanism that can explain the reason for the bluntness of the tip is explained in Figure 4.11. In the presence of externally applied electric potential, the oxonium and phosphate ions reach around the LaB_6 rod. In order to get a well-shaped nanometer tip each layer of La and B should ideally be removed by the etchant upon coming into contact with the oxonium and phosphate ions respectively. Etching of each La or B layer produces the bubbles of hydrogen gas that disturb the distribution of the etchant ions (PO_4^- or H_3O^+) for the next layer (B or La). Initially when the rod is in the sub-mm range (Figure 4.11a), b) & c)), these ions get enough surface area to perform the etching process even with this non-uniform distribution of ions. This results in the small pits along the length of the rod immersed into the electrolyte (Figure 4.10). With further etching, the depth of the pits increases. This makes the pits filled region (below the apex) so delicate that it can't hold the apex weight anymore, resulting in the dullness of the tip. This process takes place very quickly that makes it beyond the capability of the human eyes to observe this phenomenon. To some extent, from SEM images (Figure 4.12) it can be estimated that the tip apex reaches a sub-micron regime before the dullness starts. This explains why the tip diameter below 1-10 μm was never achieved after the electrochemical etching.

The etching process described above clearly outlines the difficulties of the LaB_6 etching process where the two different elements (La & B) are present in comparison to W etching where only a single element needs to be etched. To understand the elemental composition of the tip after etching energy-dispersive x-ray spectroscopy (EDX) was performed on the tip by Arno Jeromin at NanoLab in DESY.

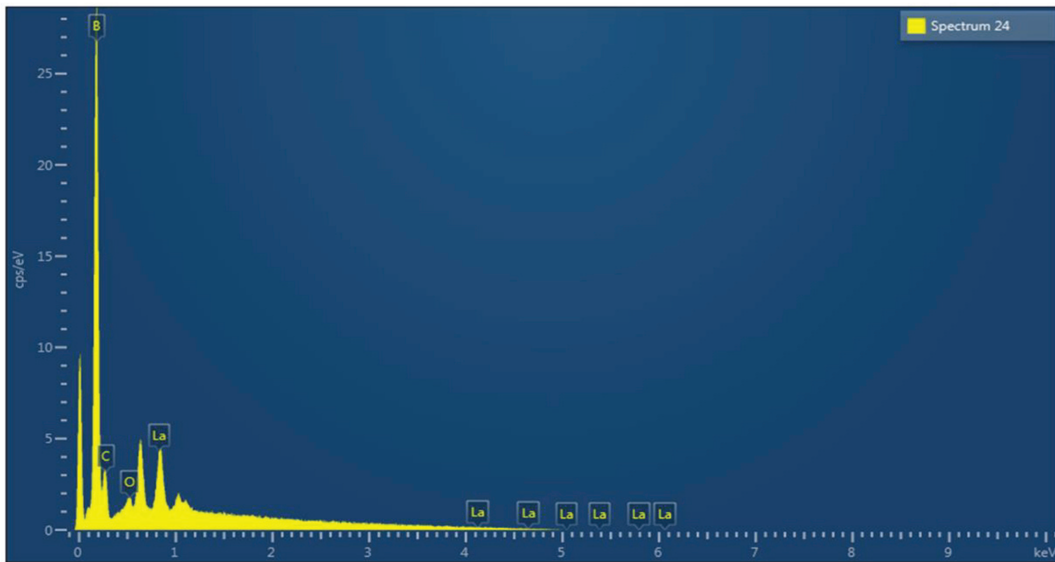

Figure 4.13. EDX spectrum shows sharp peak of La and B after chemical etching

EDX spectrum of electrochemically etched tip shows sharp peaks for B and La. The quantification of elemental composition in the EDX spectrum for elements having atomic number < 10 is not very reliable, which makes it very difficult to comment on the composition ratio of B in the etched tip because of its low atomic number (Z = 5). Lanthanum relative concentration, however, was found to increase by approximately 10% (from 68% to 78%). With the reasonable assumption that only La and B were present in the rod, it can be concluded that B concentration reduced by 10%.

As mentioned above in the current section, the chemically etched tips were not sharp enough in order to be useful as a field emitter, and hence further sharpening of the LaB_6 tips was performed using focused ion beam (FIB) milling as shown schematically in Figure 4.14 (left). The working principle of FIB milling is discussed in section 3.2.

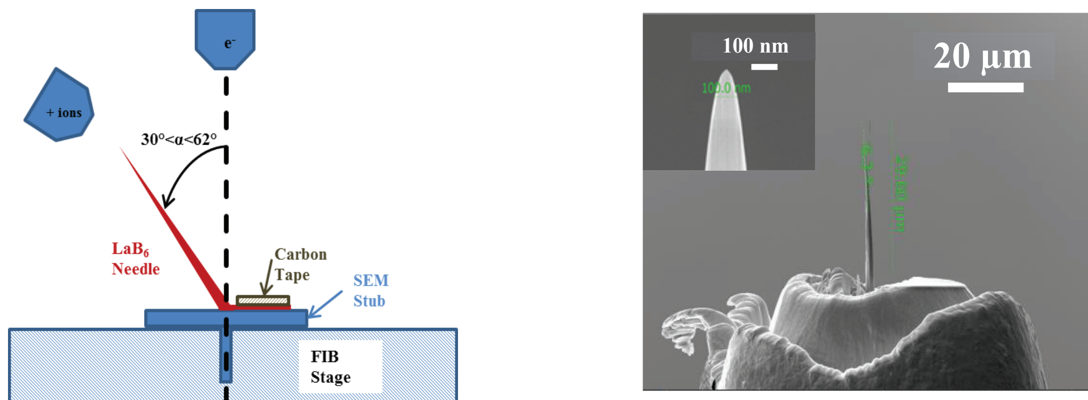

Figure 4.14 Schematic of FIB milling of LaB_6 needle (left), LaB_6 tip after FIB milling (right), inset is showing apex of the tip. Images are taken from Singh *et al.*[150]

The LaB_6 rod was attached to a standard SEM stub using conductive carbon tape. The rod was then tilted to an angle α ($30° < \alpha < 62°$) with respect to the normal direction of the stub. This was the optimized tilted position assured the access of the positions required for the milling and in-situ imaging during the whole FIB milling procedure. The electron beam was set at 90° to the stub surface, as shown in Figure 4.14 (left).

To initiate the milling process, the rod was aligned on-axis with the ion beam using nano-manipulators. At this time the milling position, imaging position, and finishing position were defined. The milling position was the spot where the needle was aligned with the ion beam (tilt angle = $52° - \alpha$) for the rough milling. The imaging position was the place where the rod was positioned perpendicular to the electron beam and therefore it was used for the imaging and measurement of the apex dimensions (tilt angle = $90° - \alpha$). The finishing position was the spot where the rod was perpendicular to the ion beam, which was used for the fine milling of the tip to smooth the surface (tilt angle = $(52° + \alpha) - 90°$).

The LaB_6 microtip milling procedure was motivated by the annular milling method used for the preparation of the atom probe tomography specimens by researchers [139]. The rough milling (with a beam current of 21–60 nA at 30 kV) was used to sharpen the electrochemically etched microtip by iteratively removing ring-shaped areas, thereby decreasing the inner diameter. This step was followed by finer milling, involving gradual reduction of the ion current (typically from 2.5 nA to 80 pA), as well as the outer (usually from 20μm to few μm) and inner diameters of the milling pattern (typically from 2-5μm to few tens of nm). Finally, a polishing step using an ion beam of 5 kV and a current of 40 pA for approximately 20 s with an inner diameter mask setting of zero was applied to reduce the level of gallium implantation. Figure 4.14 (right) shows one of the etched tips after FIB milling. This process resulted in the conical structures with lengths of approximately 20–30 μm and base diameters of 2–5 μm. The apex diameters were chosen in the range of 10nm to 100nm during this thesis work because of the reasons discussed in chapter 2. The combined LaB_6 fabrication procedure (electrochemical etching and FIB milling) yielded field emission structures with large bases (tens of μm) and good mechanical stabilities and electrical conductance. The FIB milling eliminates potential surface contamination and chemical changes caused by electrochemical etching. A high degree of reproducibility is also ensured by this process[140]. A possible concern is the destruction of the LaB_6 crystallinity due to ion bombardment during FIB milling. In the upcoming section, gallium implantation issues and morphology of the fabricated LaB_6 tip are discussed in detail.

4.2 Surface study of the fabricated tip

A high-resolution transmission electron microscope (HRTEM) image (captured by Dr. Zheng, Rafal Borkowski group, Jülich Forschungszentrum) of the apex of the tip is shown in Figure 4.15. Although an amorphous layer with a thickness of around 7 nm

is surrounding the LaB_6 tip, the crystal planes can be seen clearly. To confirm the crystallinity of the sample, electron diffraction in TEM was performed. Figure 4.15(inset) shows the electron diffraction pattern of the sample. Sharp spots in the diffraction pattern confirm the crystallinity of the sample after the FIB milling. There are two possible reasons for the amorphous layer formation. One could be the damage of the tip surface due to the energetic Ga ions. Second could be the oxide layer that is covering the tip and observed before in other fabricated metal tips[141]. To determine the elemental composition of the LaB_6 tip, energy dispersive x-ray spectroscopy (EDX) was performed (Figure 4.16). It can be observed that there is a sharp peak of oxygen that was not there before FIB treatment (Figure 4.13), confirming that the amorphous layer contains the oxides. The EDS spectra, however, do not provide the information about the Ga implantation and the region of damage, it can confirm that the surface of the tip apex is covered with an oxide layer.

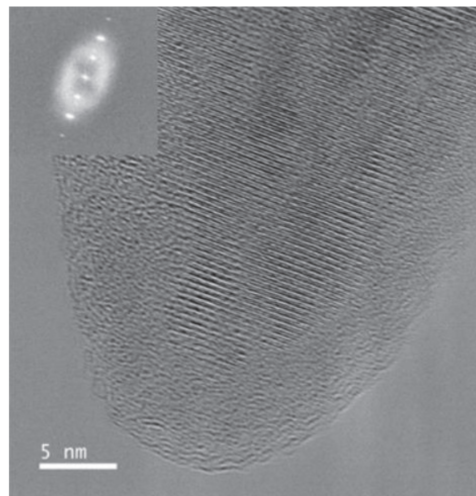

Figure 4.15 HRTEM image of the FIB milled LaB6 tip apex, inset is showing the electron diffraction pattern. Image taken from Singh *et al.* [150]

One more interesting observation in the EDX spectra is that after the FIB milling boron peak vanished from the spectra. There could be two reasons for this. First, due to the isotropic nature of FIB milling surface atomic smoothening took place resulting in the exposure of underlying (100) oriented planes that are La terminated planes[142]. The second reason could be that the EDX-SEM can only give information about the surface elements. Due to 7-8 nm thick amorphous layer, it would be difficult for the low energy excited X-rays from the boron ($E_{\mathrm{Boron}}^{5\,\mathrm{keV}} = 183$ eV) could reach the detector. This also provides the reason for the signal from the La ($E_{\mathrm{La}}^{5\,\mathrm{keV}} = 883$ eV) being attenuated in comparison to the signal from freshly etched LaB_6 tip (Figure 4.13).

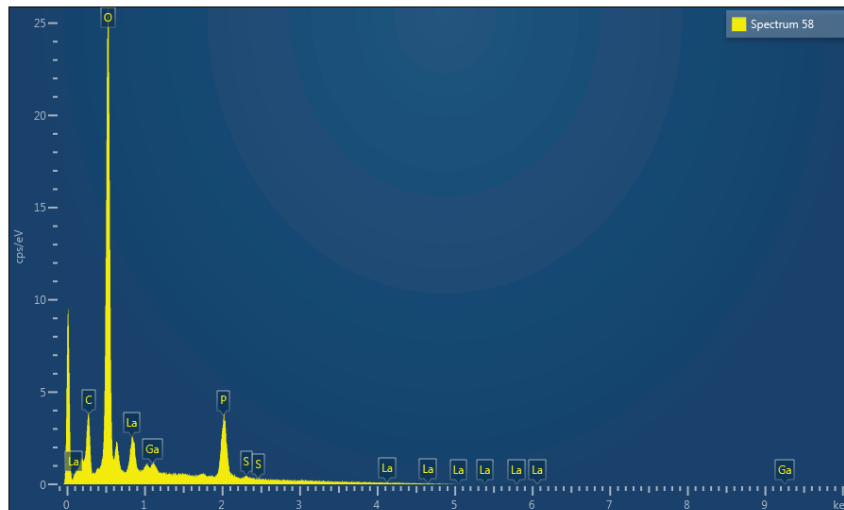

Figure 4.16 EDX spectrum of LaB_6 tip at accelerating voltage of 5 keV

Due to limitations of EDX and STEM, no information about the Ga implanted region and the damage of the crystallinity of the sample (tip) could be obtained. To understand this stopping and range of ions in matter (SRIM) software was used to simulate the FIB milling process of LaB_6 and to address the Gallium implantation issue and its effect on the crystallinity.

4.3 Gallium implantation issues and the damage of the LaB_6 surface

It is well known that the FIB-based fabrication implant gallium into the surface of the specimen and can produce damaged regions and amorphization of crystalline materials[143]. Gallium implantation also puts atom probe specimens under additional stress due to the large size of the gallium atoms compared to most of the elements. This additional internal stress can promote failure in brittle materials under the application of the high field necessary for field emission. Therefore, steps are normally taken to minimize the level of gallium implanted into the specimen[144].

It is evident that the gallium or the damage due to gallium is located in a thin shell around the edge of the LaB_6 tip apex (Figure 4.15). The range of the gallium ions for different accelerating voltages and incident angles may be predicted with the stopping and range of ions in matter (SRIM) simulation[145]. SRIM simulations were performed to understand the implantation of gallium ions as well as the damage which occurred inside the fabricated LaB_6 tips.

When the energetic ions penetrate a solid, they lose energy in two ways. First, by collisions with the nuclei, called nuclear stopping power, create lattice disorder and may eject surface atoms. Second, the loss of the energy to the electron cloud in the solid, called electronic stopping power, results in a uniform drag and may break some chemical bonds. For a heavy and low energy ion, nuclear stopping power dominates; while for a light and high energetic ion, electronic stopping dominates. In our case, Ga (atomic mass – 69 u) was used as a milling ion which acts as a heavy-ion for boron hexagonal structure (molecular mass-66 u) and as a lighter ion for lanthanum (atomic mass-139 u) in LaB_6.

Due to this non-uniformity in masses of the constituent (La and B) atoms in LaB_6, both elastic and inelastic collisions are possible during ion milling. Depending on the energy of the incident ion numerous interaction events such as backscattering, sputtering, and implantation occur (Figure 4.17). Every time a Ga ion strikes the LaB_6 surface, it transfers a significant portion of its momentum to boron hexagonal structure due to the small mass difference. On the other hand, small momentum-exchange occurs between Ga and La due to the significant difference between their masses. Hence, La is sputtered less in comparison with the hexagonal boron structure.

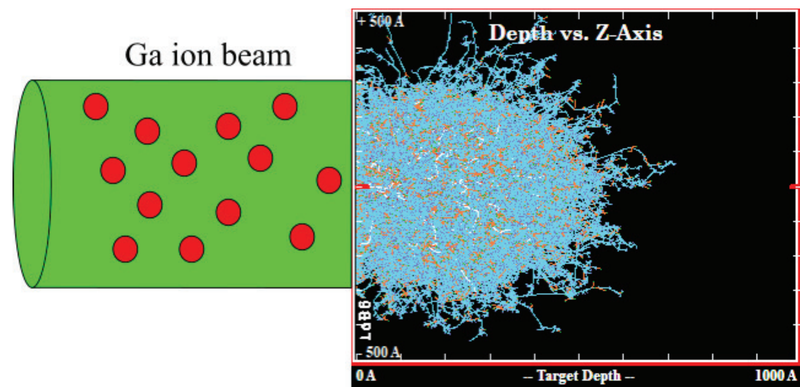

Figure 4.17 Simultation results of Ga ion trajectory (sky blue) inside the LaB6 and red dots showing the defect (vacancies) created during FIB milling

This might be one of the explanations for B deficiency observed in EDX measurement above. To quantify this non-uniform sputtering of the constituent atoms their corresponding sputtering yield needs to be considered.

The sputtering yield, which is the mean number of sputtered target atoms per incident ions is very sensitive to surface binding energy (SBE). The SBE of the material changes due to the surface stoichiometry for compounds. It is possible that some of the recoil cascade atoms of La and B which exit the target have originated from deeper subsurface layers inside the target than just the surface of LaB_6. The average surface binding energy E_{surf} of LaB_6 is 5.1 eV (Figure 4.18). Upon impact, each energetic Ga ion produces a cascade of recoiling atoms with energies E_{recoil}. Of these recoiling atoms those with recoil energy $E_{recoil} < E_{surf}$ are not sputtered, and those having $E_{recoil} > E_{surf}$ sputtered from the surface. In Figure 4.18 it can be seen that the number of La atom reaching to the surface with energy higher than E_{surf} is 0.5 to 0.6 and the corresponding number of B atom is 4. This result shows that B is preferentially sputtered in comparison to La in a ratio of 8:1 or 7:1. This implies that after the end of FIB milling, there will be a slight B deficiency in contrast to actual LaB_6 structure as observed by other researchers experimentally[142]. In previous studies, it was found that the work function of lanthanum borides stays nearly constant (2.7eV-2.9eV) in the region between LaB_4 and LaB_6 [146]. So, there should be no change in the electron emission property of the fabricated tips due to this change in stoichiometry.

The Ga ions distribution in the fabricated structure with FIB milling helps in predicting the range of the affected or damaged region inside it. The Ga implantation can be predicted by observing the Ga ions distribution inside the LaB_6 tip (Figure 4.19). The distribution curve shows that the Ga ion reached depths up to 13 nm, however, their concentration peaks at 8.9nm. This is in close agreement with the thickness of irregularities (7-8nm) observed in the HRTEM image (Figure 4.15).

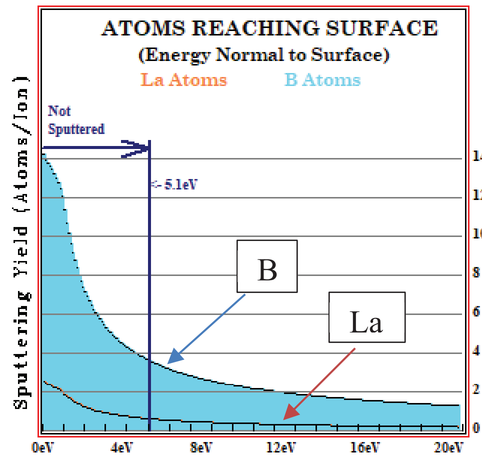

Figure 4.18 Sputtering yields of La and B atoms on hitting with energetic 30 keV Ga beam

The unit of the y-axis of the distribution plot is in (atoms/cm^3)/(atoms/cm^2). Multiplying this unit with implantation dose (atoms/cm^2) gives the impurity or ion concentration inside the ion milled structure, which is the LaB_6 tip in our case. The typical dose value of 1×10^{15} Ga ion/cm^2 was used for each fabricated tip. On multiplying this value with the peak value of the ion distribution gallium ion concentration, 7×10^{20} ions/cm^3, is obtained. It follows that there must be a high concentration of Ga ions present around 10nm below the surface of the tip. It can also be argued that such a high concentration of the implanted ions can create the amorphous layer of Ga in LaB_6. To address that point we need to examine the collision events happening inside LaB_6 subject to the energetic Ga ion bombardment. As the incident Ga ion is different than the constituent atoms of the target (La and B), the collision causes only the formation of the vacancies in the target (LaB_6) besides those atoms that are knocked out of the sample. Figure 4.20 shows the vacancies formation in the LaB_6 at different depths. It shows that at the peak of the damage, at around 7-8 nm from the LaB_6 surface, vacancies are forming at a rate of 1.25 per incident ion per Angstrom. It means at an implantation dose of 10^{15} /cm^2 there would be 1.2×10^{15} /Å-cm^2 vacancies in this region. That means that the layer near the fabricated tip surface is an amorphous layer of Ga. To avoid this, the tip was annealed at high temperature (~800 ^{0}C) after fabrication as discussed in Chapter 5. It is known that after annealing, 99% of the damage anneals out. This means that after annealing 1.2×10^{13} / Å-cm^2 or 1.2×10^{21} / cm^3 stable vacancies remain in the LaB_6 damaged region.

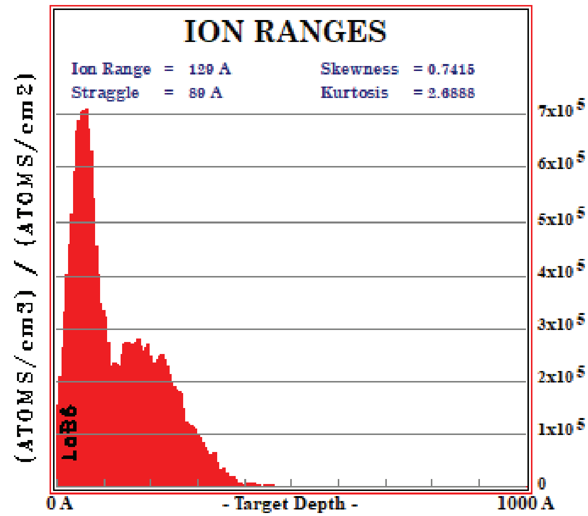

Figure 4.19 Gallium ions distribution inside the FIB milled LaB_6 tip showing a peak at 8.9nm

The density of LaB_6 is 1.5×10^{22} / cm^3, and thus only 8% of the region (7-8 nm) near the tip is damaged, and the rest of the region is the oxide layer. The characterization results of the LaB_6 tips are presented in Chapter 5.

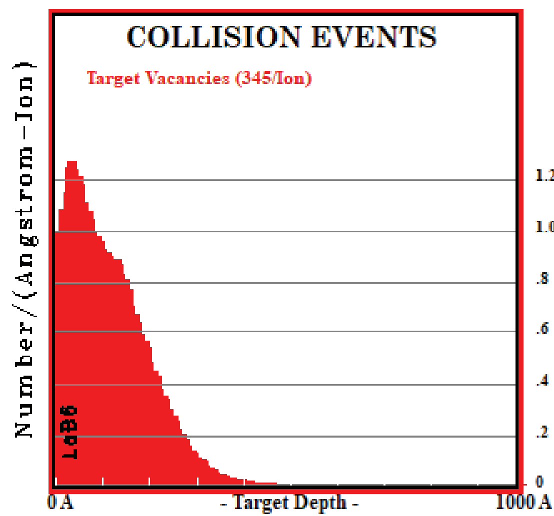

Figure 4.20 Graph showing the number of vacancies formation inside the fabricated LaB_6 tip per target atom

5 Characterization of the fabricated electron sources

This chapter is about the characterization of the fabricated electron sources (W and LaB_6 CFE) in this thesis. It begins with the I-V results of the fabricated sources followed by the stability test of field emission current and energy spread measurements at the same vacuum level of 5×10^{-9} mbar. Due to the poor emission stability of W, studies of the angular current density and energy spread were not carried out for W. Furthermore, simulated results on thermal effects of the emission current as a function of the tip apex temperature are discussed. The study of the temperature profile is crucial not only to understand the relation between emission current, Nottingham effect, and energy spread but also to realize the benefits of using the low work function materials as a field emitter.

After characterizing the continuous electron beam, electron pulses of the required temporal regime (1-10 μs) were generated, and the characterization results are presented. This chapter concludes with a summary of the results obtained with the fabricated LaB_6 tip. Some images of this chapter were published already by the author and are cited wherever required.

5.1 Field emission measurements of W and LaB_6

Fabricated W and LaB_6 tips have a radius between 15-100 nm. The reason for limiting the radius to this range was to keep the ratio of brightness to energy spread sufficiently large, as discussed in chapter 2. Field emission current measurements of both the emitters with approximately the same apex radii were performed in the test chamber (Figure 5.1).

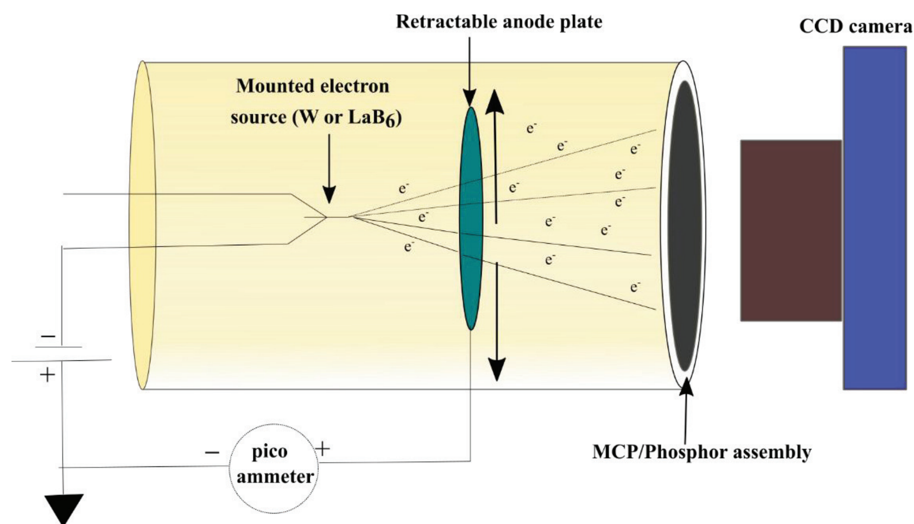

Figure 5.1 Schematic of the test chamber (photo shown in Chapter 3) used to measure the field emission current

The SEM image of the tested tungsten tip and its field emission micrograph is shown in Figure 5.2. The bright spots in the FEM image are due to the low work function regions, with dark areas corresponding to higher work function regions on the tip.

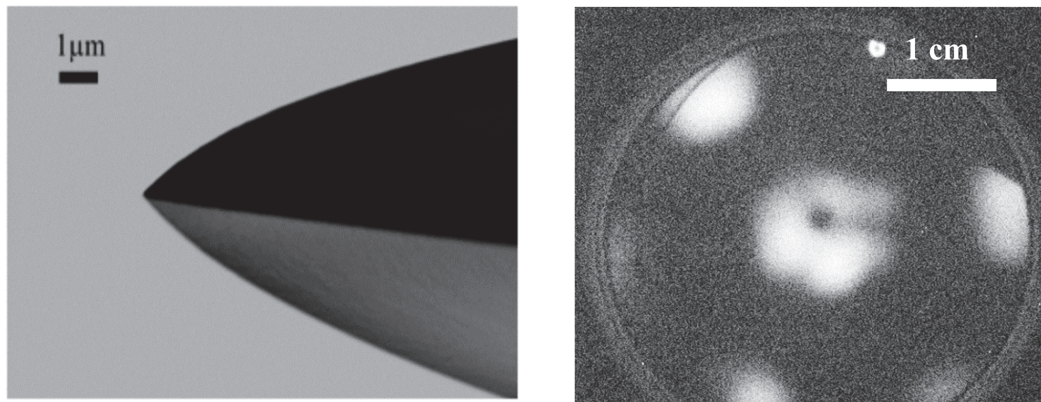

Figure 5.2 a) SEM image of W(111) tested in the vacuum chamber for its I-V characteristic, b) field emission micrograph (FEM) of W(111) tip

With a vacuum level of 5×10^{-9} mbar, it was difficult to get a stable emission current from the W(111) tip. Hence, to record the current versus voltage data, the vacuum level was brought down to 7×10^{-10} mbar. The I-V measurement and Fowler-Nordheim (F-N) plot of the W(111) are shown in Figure 5.3

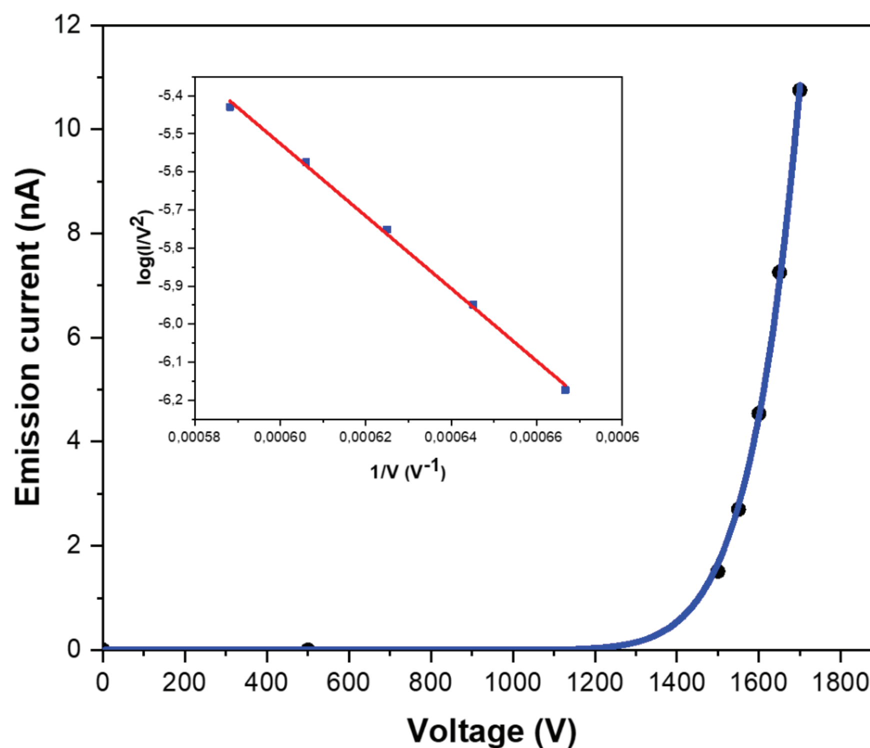

Figure 5.3 Graph showing experimental I-V data (black dots) of W tip fitting very well with theoretical F-N model (solid blue line), (inset) showing F-N plot of the same tip, straight-line fit confirms the emission of electron from the localized state of W

The Fowler Nordheim (F-N) equation (Eq. 2.36) written in a more straightforward form as:

$$I = AV^2 \exp\left(\frac{-B}{V}\right) \quad 5.1$$

where

$$A = 1.5 \times 10^{-6} \frac{S\beta^2}{\emptyset} \exp\left(\frac{10.4}{\sqrt{\emptyset}}\right) \quad 5.2$$

$$B = \frac{6.44 \times 10^9 \emptyset^{\frac{3}{2}}}{\beta} \quad 5.3$$

V the applied voltage, I the emission current, S the emitting area, and β the field enhancement factor. All of the quantities are in S.I. Units, while the work function $\emptyset$ is in eV. From Equation 5.1, a high emission current can be achieved by choosing a material that has a low work function, as well as by fabricating a sharper tip, as the field enhancement factor is typically inversely proportional to the tip apex radius, and hence, $\beta \propto S^{-1/2}$. The fabricated W tip was cleaned using thermal flashing (resistive heating) at 1500°C. Subsequently, the I-V curve and F-N plot were recorded and shown in Figure 5.3. Least-square fits of Equation 5.1 are in excellent agreement with the data for $B = 2.1 \times 10^4$ V. On using Equation 5.3 this gives $\beta \sim 2.9 \times 10^6$ m^{-1}. Using the value of β in Equation 2.15 provides the radius approximately 70 nm at the time of the test.

The LaB_6 tip (Figure 5.4) with approximately the same radius was fabricated with our controlled and reproducible method of fabrication (discussed in Chapter 4), and its I-V characteristic was recorded as shown in Figure 5.5. The field emission current was quite stable at 5×10^{-9} mbar vacuum level. No significant jumps in the current profile were seen for 30-35 minutes after thermal flashing (conditioning) at approximately 1200°C, after which I-V data was recorded.

The image of the emission pattern is shown in Figure 5.4. A beautiful single and almost symmetrical beam spot is suggestive of the presence of a single emission site on LaB_6 electron source.

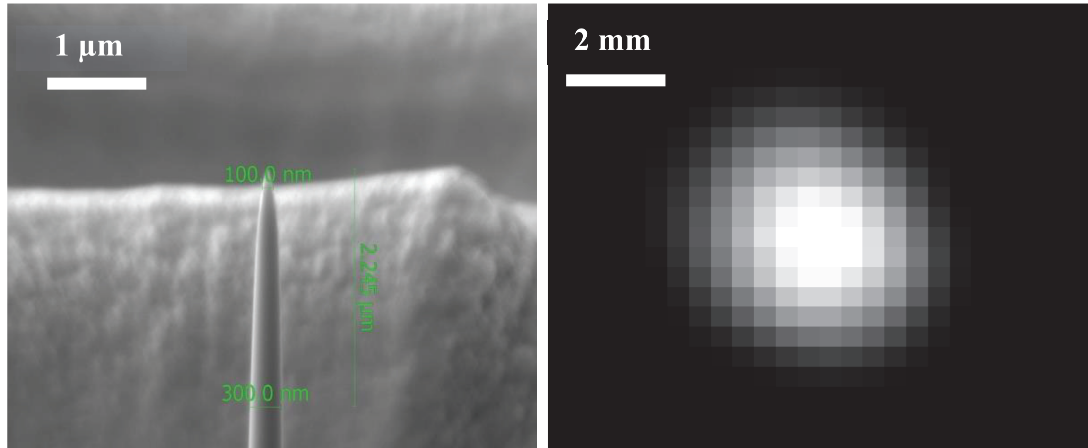

Figure 5.4 (left) SEM image of LaB_6 (100) tip before testing for field emission test, (right) FEM image of LaB_6 oriented along (100) direction

The lower onset voltage of field emission for LaB_6 than the W, even having the same radius of both, is due to the low work function. The onset voltage in our measurements was defined as a voltage at which 100 pA emission current was observed. A least-square fit to Equation 5.1 is in excellent agreement with the data for $B = 9.7 \times 10^3$ V. Equation 5.3 then yields $\beta \sim 2.9 \times 10^6$ m^{-1} which implies that the radius of the LaB_6 tip is approximately 70 nm (Equation 2.15).

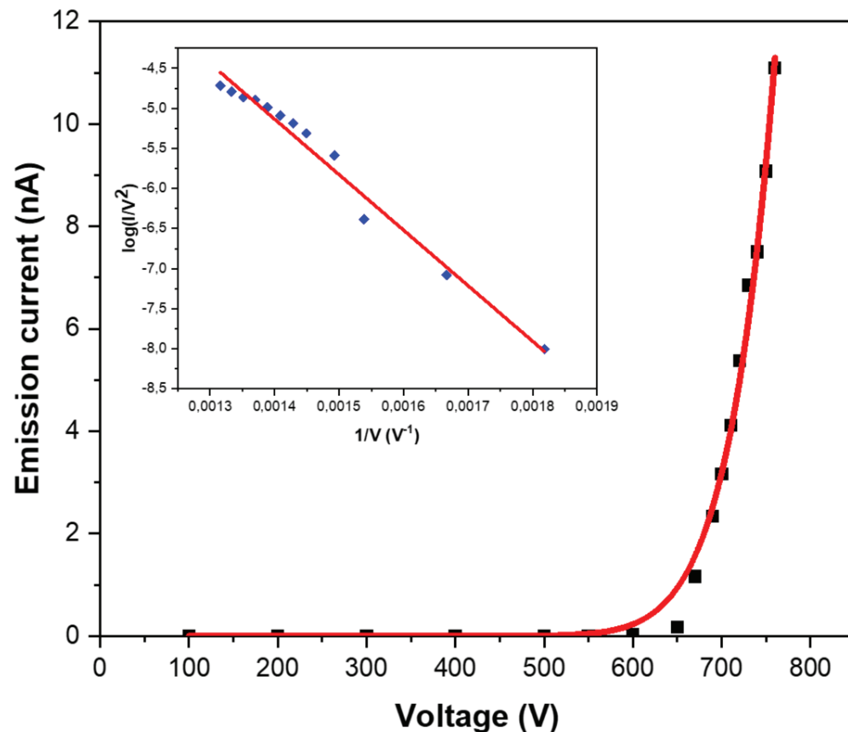

Figure 5.5 Experimental I-V data (black squares) of LaB_6 tip orientated along (100) direction with theoretical model fit (solid red line), inset showing linear F-N plot of the tip

5.2 Reproducibility test of our method of fabrication

The shape of tip apex can be altered smoothly using thermal or field assisted atomic diffusion conditioning[78]. However, the final form of the tip is completely dependent on the tip profile before conditioning[147]. The lack of reproducibility in the fabrication of tips in terms of shape and size makes field emitters an impractical electron source despite having many useful properties compared to thermionic and Schottky electron sources. Usually, an electrochemical etching (top-down approach) or chemical synthesis (bottom-up approach) does not give control over the shape and size of nano-emitters[148][111]. Hence, emitters fabricated by these approaches have a wide distribution of sizes and shapes[148].

Tip No.	Diameter after electrochemical etching (µm) ± 1µm	Diameter after FIB milling (nm) ± 5nm	Results
1	4	70	Successful
2	7	85	Moderately Successful
3	10	75	Successful
4	9	80	Successful
5	15	120	Fail
6	3	15	Fail
7	8	67	Nearly Successful
8	5	75	Successful
9	23	78	Successful
10	13	83	Successful
11	17	70	Successful

Table 2 Statistics of the diameters of LaB_6 tips after electrochemical and subsequently FIB milling step. Out of 11 attempts to control the size in the narrow range of 70-80nm around 9 were successful.

Previously employed methods of fabrication[148][141] are not suitable when there is a requirement for emitters to have almost the same diameters or shape within an acceptable tolerance of ± 10 nm. Due to this, researchers are still looking for the best methods of fabrication that give them control over these parameters. For field emitters made up of compound materials like LaB_6, it is even more difficult[149]. As explained in chapter 4 (see section 4.1.2), due to the stoichiometric composition, the author also failed to fabricate the LaB_6 tips using electrochemical etching.

To test the reproducibility of the method of fabrication used in this thesis (section 4.1.2), 11 attempts were tried to replicate the tips with the diameter in the range of 70-80 nm. Out of which, 9 times tips of similar conical shape and approximately the same size (70-80 nm) were produced (Table 2). It implies that the success rate of the present method of fabrication is better than 80%.

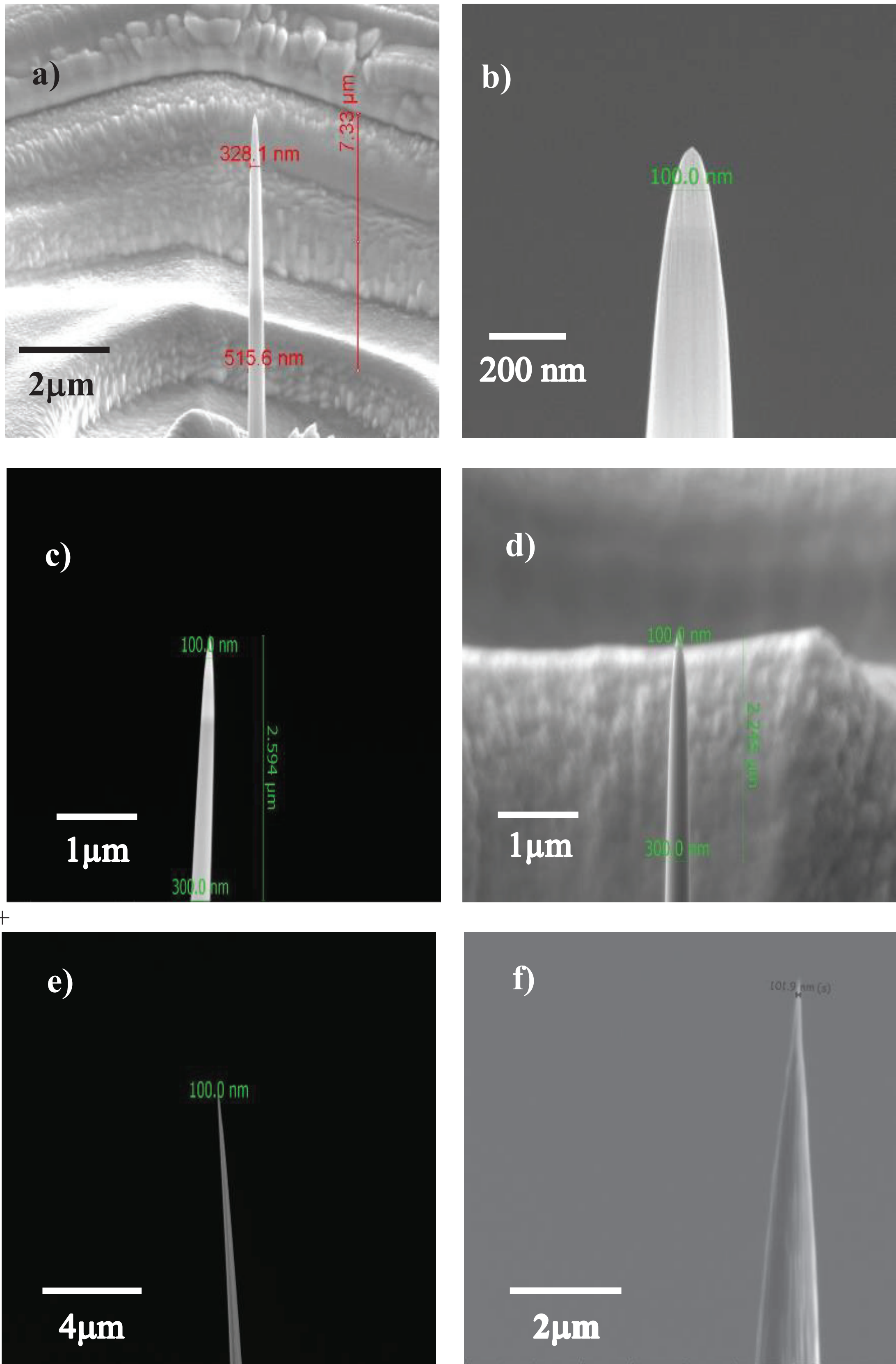

Figure 5.6 SEM images of some of the fabricated LaB_6 tip right after FIB milling process, it can be seen that the shapes (conical) of all the emitters are almost identical (Image (b) is taken from Singh *et al.* [150]**)**

After the FIB milling step, the tip was transferred to the test chamber (Figure 5.1) for the invaccum-cleaning process. In the vacuum, the tip surface was cleaned using resistive heating so that dirt or adsorbates could be removed. An electric current (2-2.5 A) was passed through the Ta wire loop that generated heat and raised the temperature of the attached tip to 800℃. The current was switched-off after 2 mins. This process of resistive heating has two advantages: a) cleaning of tip surface and b) smoothening of tip surface by melting the tiny protrusions that were created during the fabrication. Five cycles of thermal conditioning were then applied to one pair of the tip (Figure 5.6 c and d) to achieve approximately 10 nA emission current (Figure 5.7). On fitting to the F-N equation, the tip radius was estimated to be 410 ± 8 nm and 390 ± 7 nm, respectively. It shows that the initial profiles of the tips were quite similar (~ 70nm), resulting in a very close resemblance in the shapes after identical cycles of conditioning[147]. It is one of the most significant achievements in the fabrication of field emitters based on LaB_6 that was not possible before this work[151][152]. It demonstrates the superiority of our approach for LaB_6 field emitter fabrication.

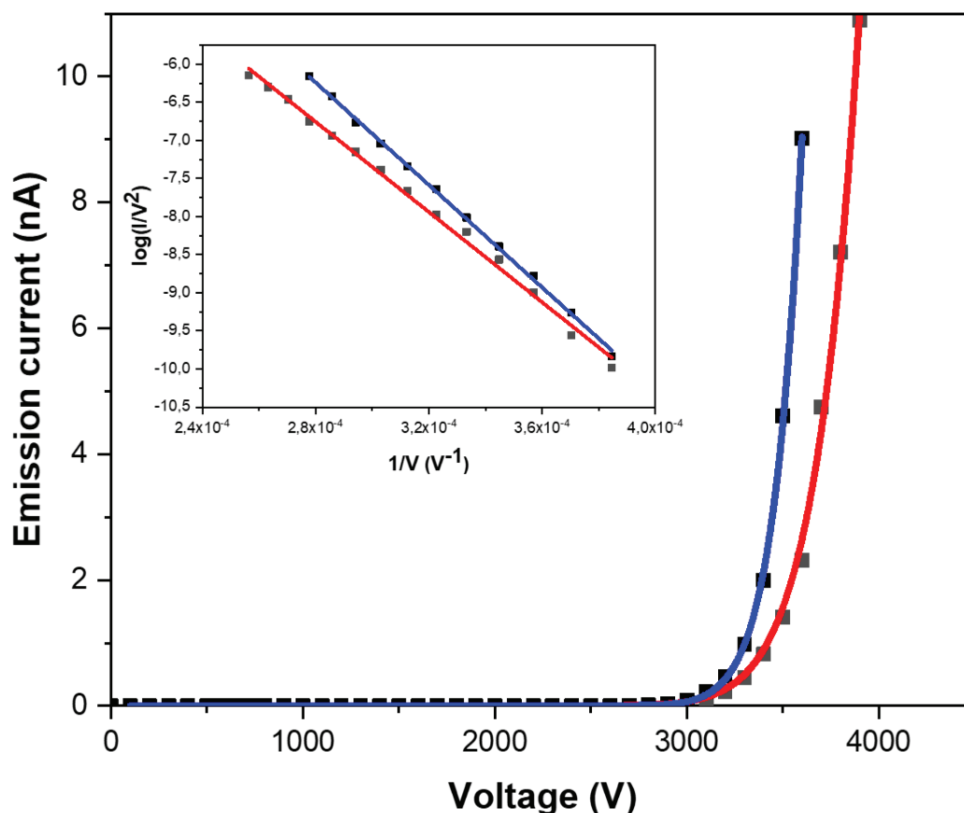

Figure 5.7 I-V curves of two tips (with approximately the same initial diameter 70nm) after thermal conditioning cycles

5.3 Temporal stability of fabricated tips

5.3.1 W tips

The temporal stability of the fabricated electron sources was the next concern following the reproducibility test. As mentioned in section 5.1, the emission current from W tips showed very high fluctuations. To record the I-V characteristics, the base pressure was reduced to 7×10^{-10} mbar after a high temperature (120 °C) bakeout for 7-10 days. Temporal stability measurement was performed at the same vacuum level. However, W tips exhibited a rapid decay in emission current. After 5 minutes of operation, the emission current reduced from 700 pA to less than 100 pA (Figure 5.8). This drop-in current is due to the coverage of the W surface with adsorbates that increase its work function[153]. The random behaviour of W tip above 100 pA is attributed to the movement of adsorbates on its surface or the sputtering phenomenon (discussed later in this section) that has also been reported previously by researchers as well[154][108].

The origin of these fluctuations is the gas adsorption phenomena that occur at the metal surface. There are two types of gas adsorption: physical adsorption (physisorption)[155] and chemical adsorption (chemisorption)[155][89]. The former occurs on all solid surfaces with all gases. The physisorption assisted forces are of the van der Waals type, long-range, and weakly attractive[75].

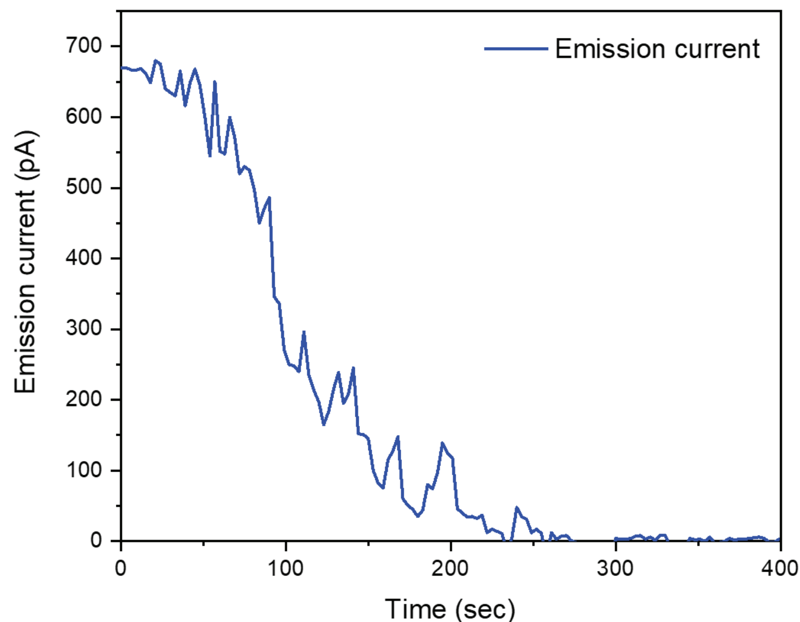

Figure 5.8 Emission current temporal profile of the W (111) tip at 7×10^{-10} mbar

For a metal surface with a homogeneous distribution of atoms, the physisorption potential (U) is shown in Figure 5.9. Localized and mobile adsorption is determined by the difference between maxima and minima of the adsorption potential, which is defined as $2\Delta U$. ΔU is known as the barrier to the translation path. If $\Delta U \ll kT$, the adsorbate

translates parallel to the metal surface and adsorption is mobile. On the other hand, if $\Delta U \gg kT$, the adsorbate stops moving and stays in one of the minima, resulting in localized adsorption. In the intermediate stage, when $\Delta U \sim kT$, adsorbed molecules start translating[155]. However, they jump from one potential well to other only at a particular temperature known as the transition temperature T_i.

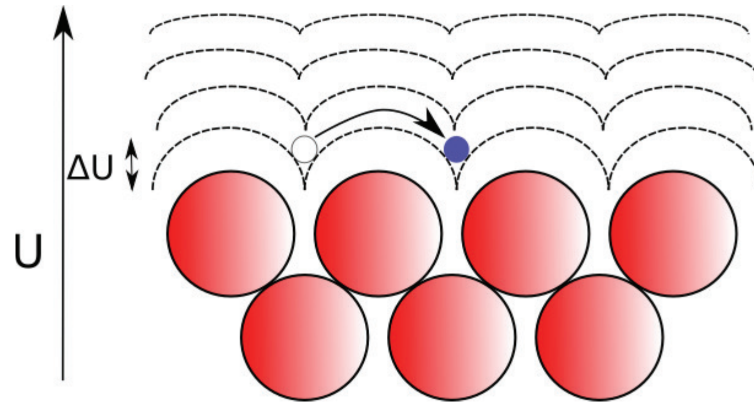

Figure 5.9 Schematic of physisorption potential at the emitter (metal) surface, dotted curves represents the variation in adsorption potential. An adsorbate (blue dot) can cross the barrier ΔU only when its thermal energy kT> ΔU

In other words, localized adsorption on the surface occurs at $T_i < \frac{\Delta U}{k}$ and mobilized translation occurs at $T_i > \frac{\Delta U}{k}$. The value of ΔU for the adsorbates (nitrogen, hydrogen and oxygen) present in the vacuum chamber remains in the range of $10^{-2} - 10^{-3}$ eV/atom, resulting in a low value of T_i, approaching the condensation temperature of adsorbed gas [156][157]. Usually, multilayers of adsorbates stick on the metal surfaces in physisorption.

Chemisorption is a much stronger phenomenon than physisorption. Energies of adsorption vary from 1-10 eV/atom[155]. This tight binding of adsorbates is confined to one or at most two layers[75]. Chemisorption is accomplished at the cost of dissociation of adsorbed molecules or by the chemical reaction with the substrate. Strong adsorption is possible only if the substrate (or emitter) has partially filled bands to which electrons can be transferred to adsorbates (from the emitter) or vice versa. Transition metals like W, Ni, Mo, Au, and Ag that are commonly used to make field emitters fit particularly well into the roles of both donor and acceptor because of their partially filled *d*-bands. The *d*-electrons experience a reduction in energy through bond formation, with a resultant reduction in bond length. Studies indicate that approximately 80 per cent of the chemisorbed layer of nitrogen, hydrogen and oxygen on W can be formed even at 4-20 K[155]. At such a low temperature the negative enthalpy of adsorption drives the chemisorption.

Gomer *et al.* [75] suggested the following mechanism to explain the fluctuations of the field emission current due to the chemisorbed and physisorbed layers: At low temperatures the chemisorbed layer forms on the field emitter and is immobile. However,

physisorbed gas molecules on top of this layer are mobile. These gas molecules migrate from the point of physisorption and are eventually trapped at the edge of the chemisorbed film. This process continues until the chemisorbed layer entirely covers the emitter surface. These movements of the physically adsorbed molecules are the cause of fluctuations, as shown in Figure 5.8. Once the collective thickness of the adsorbed layers (chemisorbed and physisorbed layers) exceeds the length of the tunnelling barrier seen by electrons near the Fermi level, reduction in the applied field as well as emission current is observed.

Classic work by Langmuir[122] indicates that nitrogen, hydrogen and oxygen are chemisorbed on W and can be desorbed at sufficiently high temperatures. However, once a clean surface has been obtained, its continued purity depends on the pressure in the vacuum chamber. For the metal emitters, at $1 \times 10^{-6} - 1 \times 10^{-7}$ mbar and a sticking coefficient of 0.1-1, monolayer formation takes one second. Hence, the pressure of 1×10^{-10} mbar or lower is necessary. It is one of the reasons why in Figure 5.8 fluctuation and dropping of the emission current were observed even after flashing at high temperatures.

Another factor that also contributes to these instabilities and reduction in the emission current is the change in the field enhancement factor β due to electron-induced desorption. These ions are the result of electron impact desorption [158] from the anode shown in Figure 5.10. It is partly related to the vacuum environment or number of gas species present inside the field emission chamber.

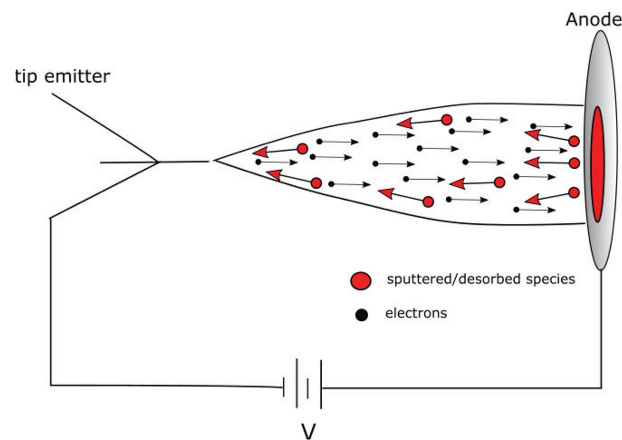

Figure 5.10 Schematic showing the anode sputtering and ion desorption phenomenon, arrows depicting the direction of ions (red) and electrons (black)

Electrons emanate from the tip emitter and are collected by the anode. Due to the applied voltage V, the total energy just after emission is eV. These energetic electrons, when received by the grounded anode, transfer their kinetic energy to the latter. When the deposited energy exceeds the binding energy of the adsorbed gas species on anode or surface atoms of the anode, they start to get desorbed or sputtered respectively. Out of these gas species, some are ions, and some are neutral atoms. Previous studies conclude

that only those ions formed in the cylindrical volume of radius $3r$ (r is the tip radius) can strike the cathode[159].

By rigorous outgassing of the anode surface and keeping the base pressure below 1×10^{-10} mbar throughout the operation, the electron-induced desorption, and resulting instabilities can be mitigated. However, there is another smarter way to reduce the irregularities: using a low work function and robust electron emitter. A smaller work function material lowers the required extraction voltage for the same emission current compared to a higher work function material. It results in a lower acceleration voltage of desorbed/sputtered ions from the anode and hence less energy deposition due to bombardments on the electron emitter. The robustness implies the bond nature or strength of the emitter material. In the next subsection, 5.3.2, the kind of bonding in LaB_6 is explained in detail. Robustness of material aids in bearing the damage without any reasonable alteration of emitter shape. The above two properties of LaB_6 (low work function and high robustness) compared to W[160] are the reasons that motivated us to develop a field emitter based on this material.

5.3.2 LaB_6 tips

The temporal stability of LaB_6 was recorded at pressures of 5×10^{-9} mbar. The results obtained with LaB_6 are shown in Figure 5.11.

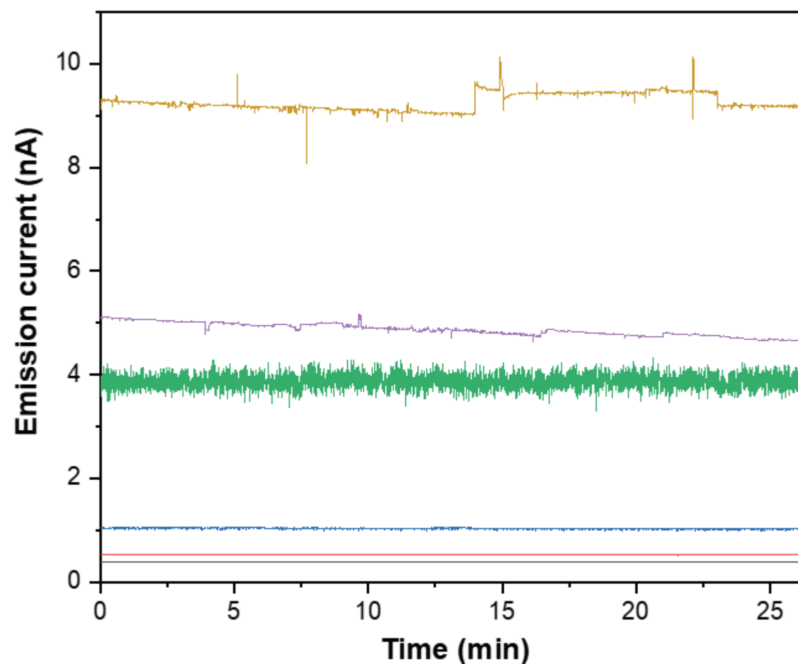

Figure 5.11 Temporal stability of LaB_6 tip1 (black, red and green), tip2(blue and violet) and tip3 (yellow), recorded at 5×10^{-9} mbar chamber pressure, for 30 minutes. Negligible drop in current was observed. Some fluctuations were observed at around 10 nA emission current, which might be due to enhanced ion collision events at higher extraction voltage (Image taken from Singh *et al*. [161])

Horizontal lines in Figure 5.11 depict much better temporal stabilities of LaB_6 compared to W (Figure 5.8). The vital point to be noted is that these longer temporal stabilities were observed at 4-7 times higher pressure and at 2-10 times higher emission current than W. Slight jumps were observed at currents around 10nA due to ionization events explained in subsection 5.3.1. These advantageous properties of LaB_6 lie in its molecular structure. As shown in Figure 4.6, LaB_6 has a simple cubic structure comprising a La atom surrounded by a B-octahedral structure located at the corner of the cube. In this thesis work, a LaB_6 single crystal oriented in (100) plane was used to fabricate the source. It is necessary to elaborate on the molecular structure of (100) terminated planes to comprehend the inherent properties (bonding nature and work function) along (100) orientation.

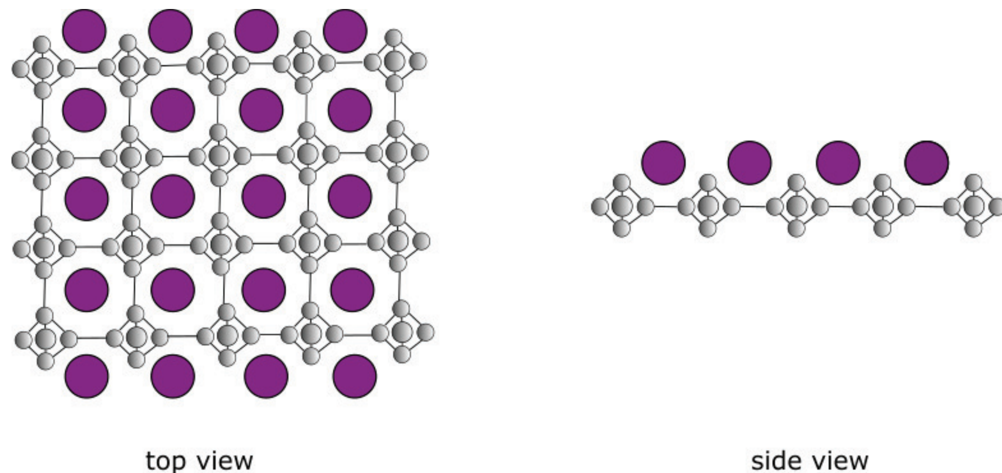

Figure 5.12 Top and side view of LaB_6 bulk with (100) terminated plane

Figure 5.12 shows the top (left) and side (right) view of LaB_6 bulk (100) terminated plane with boron (B_6) octahedron structure (grey spheres) at the cube corners. This interconnected B_6 octahedron structure provides robustness to the LaB_6 structure. Previous studies [162] showed that there is a deficit of two electrons per B_6 octahedron unit. In each unit cell, the La atom sitting at the centre transfers two electrons to B_6 octahedron. As La is a trivalent metal, the third valence electron shifts into a band formed by hybridization of B-*sp* and La-*d* states[163], hence, giving rise to the metal-like properties to LaB_6. It was stated by previous researchers that due to the transfer of electrons, dipole layer formation between positively charged La and negatively charged B_6 takes place[164]. Due to La termination, the LaB_6 (100) is the lowest work function (2.3eV) plane in the crystal compared to others because of the outward direction of dipole moment (negative B_6 to positive La)[164]. For this reason, (100) oriented LaB_6 rods were used to fabricate the electron source in the present study.

The second valuable property of the LaB_6(100) plane is its chemical inertness at room temperature that keeps surface chemical contamination low, resulting in stable field emission current, as shown in Figure 5.11. Researchers used vibration spectroscopy and x-ray photoelectron spectroscopy (XPS) to understand the cause of this directional property of LaB_6 [165]. It was observed that when oxygen (O_2) comes into contact with

$LaB_6(100)$, it gets adsorbed at La sites. When the surface gets heavily oxidized, O_2 gets bonded with both La and B sites. Desorptions of the resulting oxides BO, LaO, and B_2O_2 were detected below 1200ºC even when the surface was heavily exposed to O_2. On increasing the temperature, B_2O_2 was found to be the most dominant desorbed species. This process increases the La concentration in LaB_6 due to the prominent desorption of the abundant boron oxides[166]. Hydrogen (H_2) usually forms bonds rapidly with transition metals such as W due to *d*-shell electrons. In the LaB_6 (100) oriented planes, the deficiency of the electrons in the La-B bond makes it impossible for H_2 to bond with the surface. The LaB_6 surface is quite resistant to nitrogen (N_2) as observed by Gallagher [167] even at pressures up to 10^{-4} mbar. Carbon monoxide (CO) and water (H_2O) are the next most common background gases in the vacuum chamber. These gases also get desorbed below 500 ºC [166]. Therefore, to keep the chemical composition of LaB_6 intact, we didn't use a flashing temperature above 1200°C to remove the adsorbates.

The study of emission current noise was performed on our fabricated LaB_6 field emitter. The emission current was recorded at a level of 1.5 nA with a sampling rate of 3 Hz for 24 hours. A Fast Fourier transform of the signal was performed and the value was normalized with mean value of the emission current, I_p and sampling rate to obtain the normalized spectral density defined as $(\frac{\Delta I_p}{I_p})^2 \frac{1}{f}$ as shown in Figure 5.13.

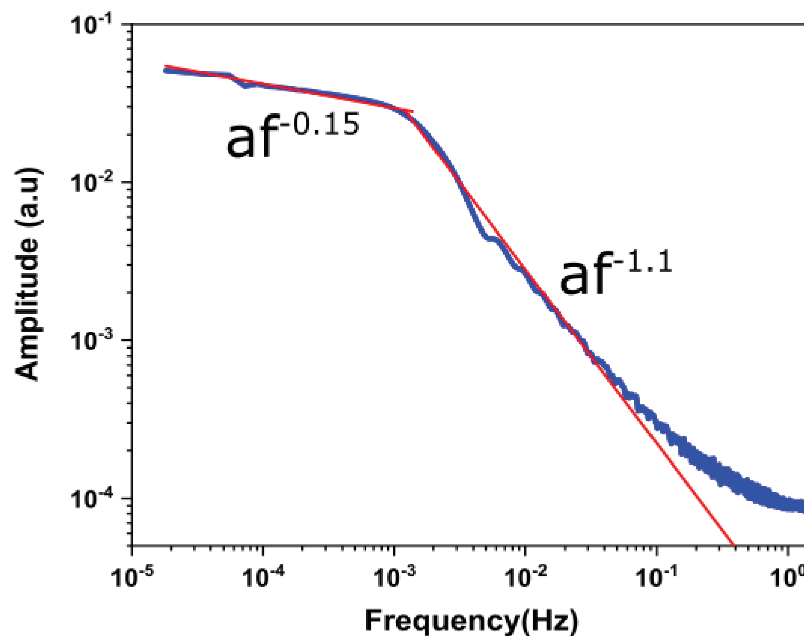

Figure 5.13 Power spectrum of the noise in emission current during 24 hours operation, in 10^{-3}-1 Hz ranges the noise magnitude is diminishing (Singh *et al.* [150])

It can be observed that there are two linear regions in the power spectrum. The first region is for the fluctuations observed at frequencies in the range of 10^{-5}-10^{-3} Hz. These fluctuations are insignificant in magnitude and may be due to movements of the

physically adsorbed gases after a very long operation of the field emitter in a vacuum environment of 5×10^{-9} mbar, as discussed above. The noise is well fitted by a power law of the form af^{-n} with a small exponent of $n = 0.15$, which indicates that these fluctuations are weakly dependent on frequency and hence present there due to complete coverage of emitter with adsorbed gases. As discussed in this section above, these physically adsorbed gases can be removed easily by flashing the cathode at temperatures (500 ºC – 1200 ºC). However, the magnitudes of fluctuations are very low ($2\% - 5\%$), so it can be concluded that there is no significant problem in a very long period of operation without flashing. The second region of the spectrum spread from 10^{-3} - 1 Hz fits very well to the power-law with $n = 1.1$. Two factors can contribute to the instabilities in this region of spectra. One is the switching of electron emission from two or more states of individual atoms (or molecules) present on the surface of the emitter[168]. Second is the transport of adatoms in the presence of field that results in 'build-up', and 'dulling' processes explained previously by researchers[154]. These processes are prominent if microprotrusions are present on the surface of the emitter. The fluctuations in the second region drop very quickly to an insignificant magnitude with an increase in frequency (Figure 5.13). It gives an insight that at a higher rate of recurrence (greater than 1 Hz) stable current pulses can be generated with this electron source. Results on pulsed-field electron emission from LaB_6 are included in section 5.7.

This section can be summarized as follows: we were able to fabricate LaB_6 tips with a novel top-down approach without disturbing its inherent properties (low work function, robustness, and chemical inertness). The temporal stability measurements for more than 30 minutes at approximately 10 nA emission current confirmed the robustness of the fabricated tip. Besides, the noise power spectrum study confirmed that weak adsorption (physisorption) is the only cause of slight disturbances that proves that chemical inertness of surface was intact even after fabrication steps and thermal flashing.

A base pressure of less than 1×10^{-10} mbar is needed for W to avoid any current emission fluctuations during measurements[108][169][159]. This level of vacuum was challenging to attain in our test chamber because of its pumps capacity. Hence, measurements like energy spread, and pulse measurements could not be performed on W. However, theoretical insights and comparison of W results obtained by previous researchers with our novel LaB_6 electron source is included in this thesis.

5.4 Angular current density

The angular current density of an emitter is defined as the emission current per solid angle. Mathematically, it can be written as[170]:

$$j_a = \frac{\Delta I}{\Delta \Omega} \qquad 5.4$$

where $\Delta\Omega$ is the solid angle subtended by the electron beam carrying current I. In this thesis work, aperture scans (of different diameters) were performed to measure the angular current density. Figure 5.14 shows the schematic of the arrangement for the

corresponding measurement. The multi-aperture plate is loaded with the apertures having different diameters ranging from 50 µm to 500 µm. The distance between the LaB_6 cathode and the aperture plate was fixed at approximately 5-10 mm due to restrictions of 2D movement of aperture plate and limited manual movement in the small chamber.

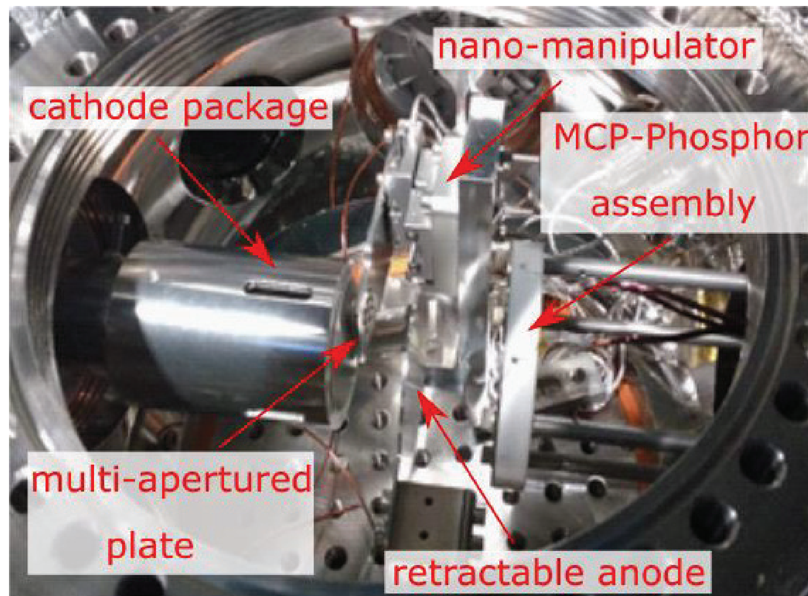

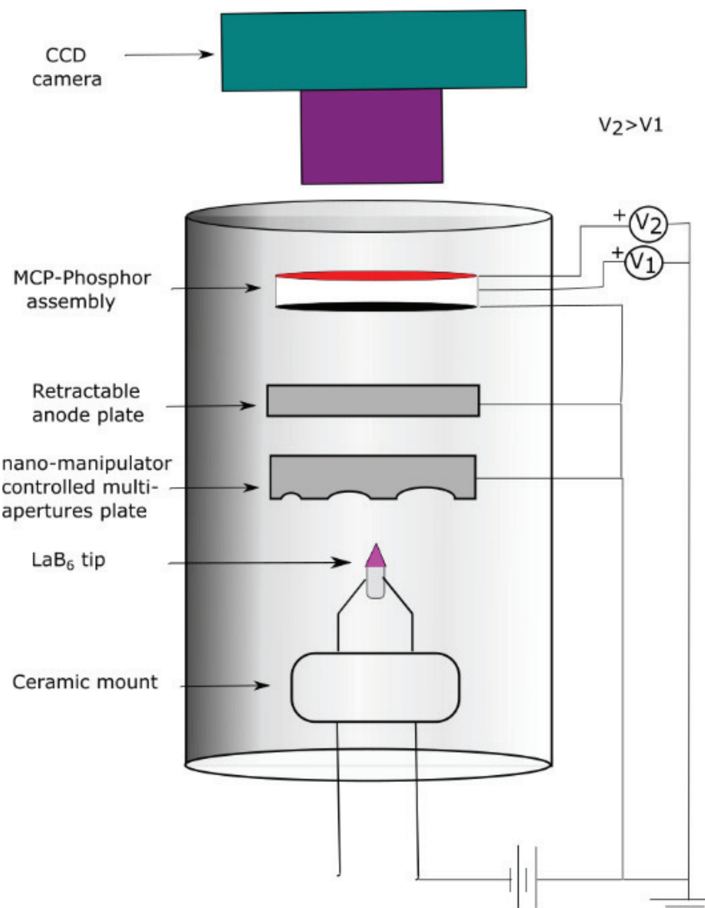

Figure 5.14 (top) photo of the arrangement of the ultra-high vacuum chamber to measure the angular current density (bottom) schematic showing a detailed configuration of the chamber

The diameters of the apertures limit the amount of beam current passing through them. The current passing through the apertures was measured using the indirect calibration method (see section 3.3). At a fixed voltage on MCP/phosphor assembly, the integrated intensities of the beam spot corresponding to emission current were calculated using ImageJ software. The ratio of emission current value to the corresponding integrated intensity value gives a calibration factor ψ. Error minimization was assured by calibrating the system before the experiment each time.

The plot shown in Figure 5.15 is the result of the scan performed with 50 μm aperture. The solid angle for this measurement is defined by the opening that allows passing half of the total integrated intensity (FWHM) as described previously[81]. The maximum value of the intensity was then multiplied with ψ to calculate the corresponding current value.

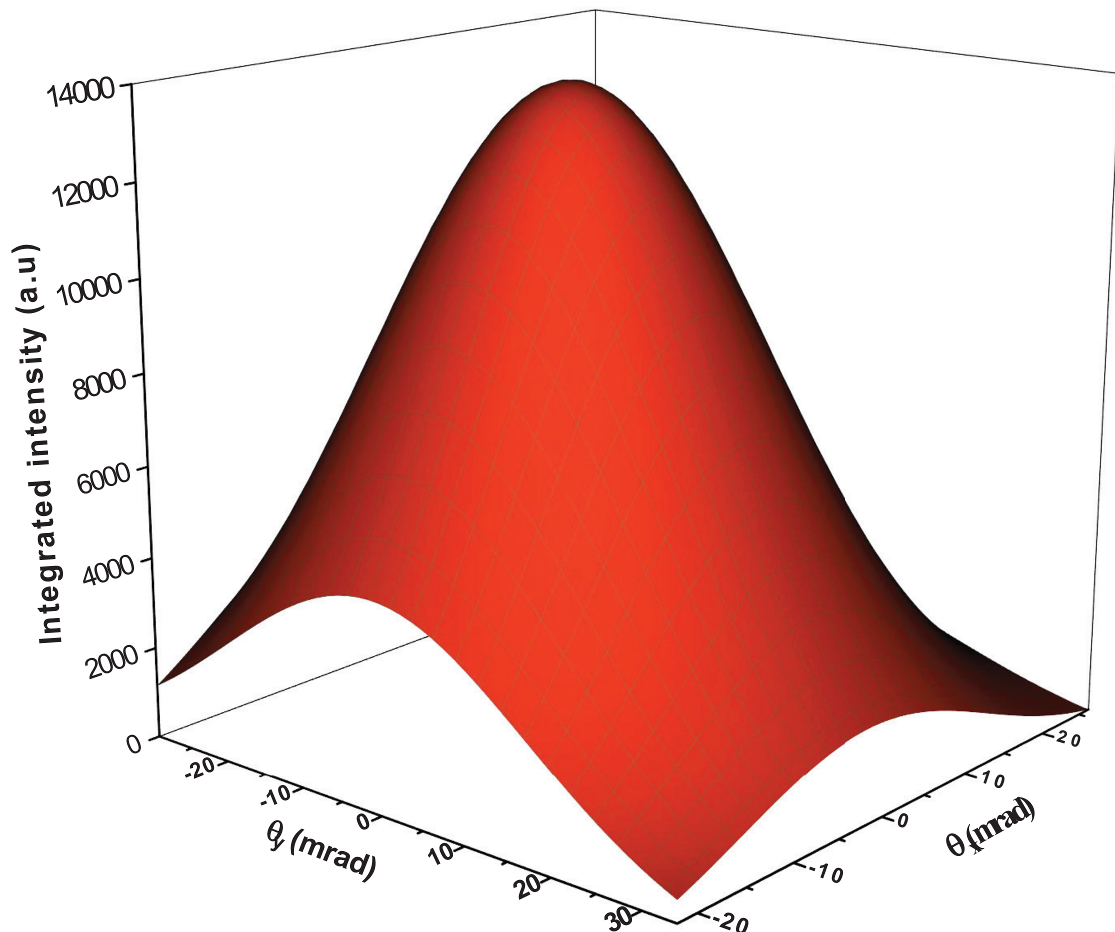

Figure 5.15 3D plot showing the variation of integrated intensity along semi-angles θ_x (along the x-axis) and θ_y (along the y-axis) for 50μm aperture

The maximum angular current density was found in the range of 4-8 ± 0.1µA/Sr at extraction voltages up to 3.7 kV. Figure 5.16 illustrates that the values of maximum current density first upsurged with aperture diameter up to 200 µm and then declined at 500 µm. It indicates that the maximum beam current with the highest current density was confined to a solid angle of 0.30 mSr correspondings to 200 µm aperture. The reason for this trend is that below 200 µm, the beam current was cut down by the polluted aperture holes. Whereas, with an aperture diameter greater than 200µm, the solid angle increased while the current comparatively remained constant or slightly enhanced (Equation

5.4). These observations and angular current density values are in the same ranges as observed by the earlier scholars[47][103][171].

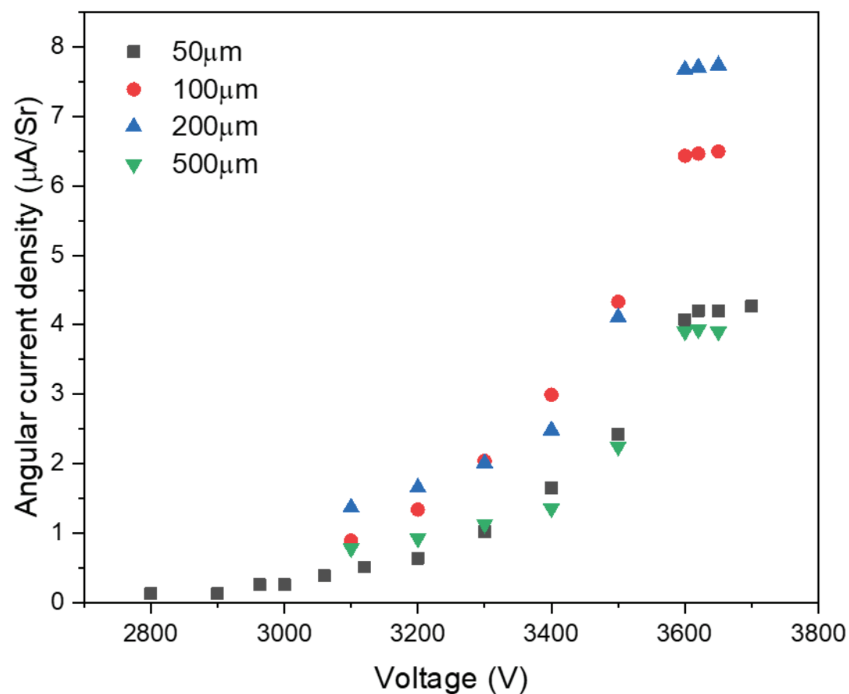

Figure 5.16 Plots showing the variation of angular current densities with applied voltages for different aperture diameters

5.5 Energy spread measurements

As discussed in section 2.2.4, energy spread is one of the most fundamental properties of an electron source that tells not only the monochromaticity of emitted electron but also gives an estimation of brightness to some extent. In the same monograph, the relation between the maximum brightness and energy spread of the beam is derived (see section 6.1).

The energy spread measurements were performed using an in-house developed retarding potential analyzer. In the upcoming subsections, the design, operation, and results of this electron energy analyzer are described.

5.5.1 In- house built electron energy analyzer

Figure 5.17 displays a schematic of the energy analyzer device (see section 3.4) developed in this thesis work. The design is based on the one suggested by Simpson [114], and some motivation is taken from Holscher's work [172].

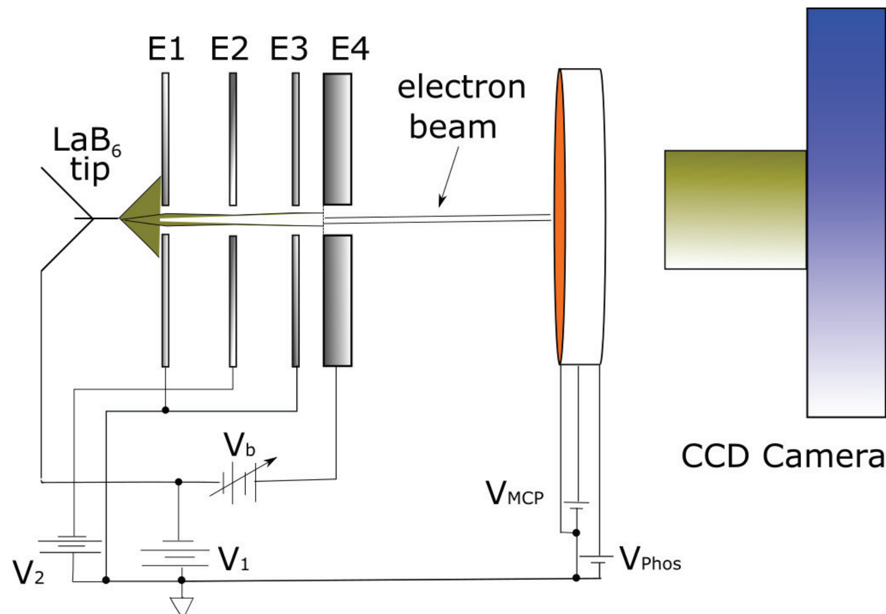

Figure 5.17 Schematic of in-house built energy analyzer showing the electron beam crossing through different electrodes and only filtered out electron having reaching to detector

This device comprised of four parallel plates (E1 through E4) each with a central hole of diameter 2 mm. The first three plates act as an Einzel lens shown in Figure 5.17. Same potentials (grounded) were applied to the E1 and E3 plates, whereas a negative voltage (lower than the emission voltage) applied to E2. The voltage to E2 was varied to achieve the required normal incidence of electrons on the hole of E4. A copper mesh of grid size 40-50 µm was fixed at the hole of E4 to establish the equipotential surfaces to the incoming electrons. The electric potential applied at E4 was regulated using a 16 V battery floating at the same potential as the LaB_6 tip. The battery potential was varied from 0 to +4V in a step of 10meV using a multi-turn precision potentiometer.

The working principle of the device can be understood in terms of Fermi levels. The Fermi level of the unbiased (0V) LaB_6 emitter remains lower to the Fermi level of E4 because of the difference of their work functions ($\Delta\Phi$). Hence, no electron can pass through E4. The electrons start to flow through E4, as a sufficient positive potential is applied to E4 that brings down the Fermi level of E4 below the LaB_6 tip. After crossing E4, electrons reach to the MCP detector, as shown in Figure 5.17. The energy of these electrons is equal to the difference between the voltage provided by the floating battery and $\Delta\Phi$.

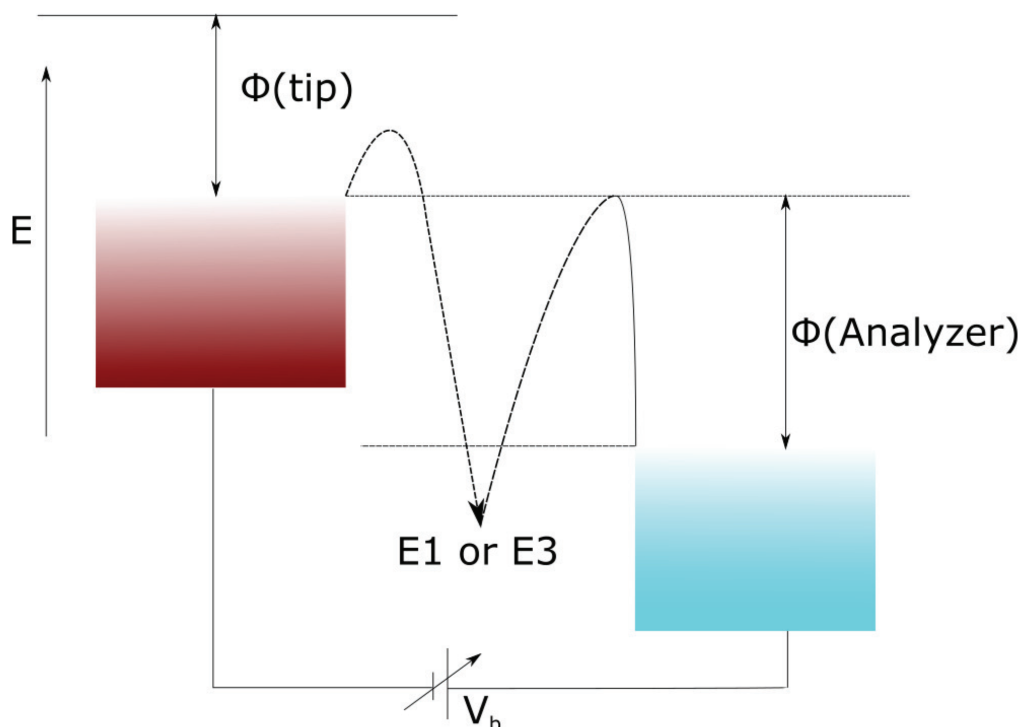

Figure 5.18 Potential energy diagram of the energy analyzer showing the transfer of electron from the tip to analyzer E4

5.5.2 Experimental results and analysis

The method of energy spectroscopy relies on the fact that the emitted electrons have energies affected by the characteristic energy levels present in the emitting material. Hence, energy spectroscopy demonstrates the type of atoms and their energy levels contained in the emitter[74][113]. The energy spread measurements were performed at room temperature to understand the electron energy distribution in our novel electron source.

The collector current is plotted (Figure 5.19) as a function of the voltage difference between the analyzer and emitter. The change in collector current with respect to the change in voltage difference gives the energy distribution of these electrons. The differentiation of data shown in Figure 5.19 was done analytically in Origin software and shown in Figure 5.20.

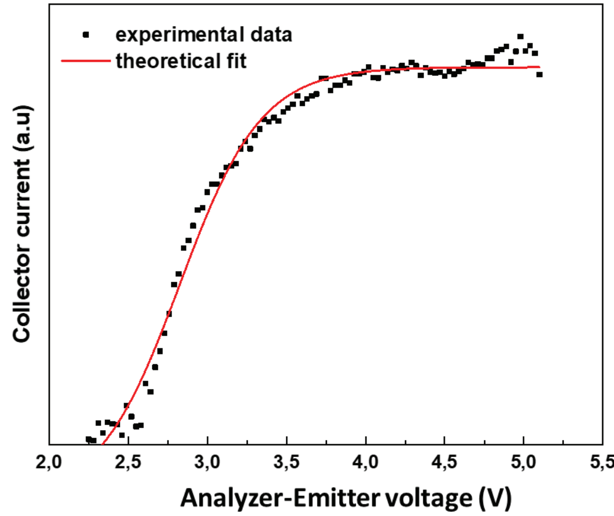

Figure 5.19 Plot depicting variation in collector current with variation in analyzer voltage with respect to emitter voltage, red curve showing the theoretical fit that is in a good agreement with the experimental data

The resultant curve was then fitted to the total energy distribution (TED) formula[113] which is the product of a field-dependent transmission probability and the Fermi-Dirac distribution:

$$\frac{dI}{dV} = A\frac{e^{\epsilon/d}}{1 + e^{\epsilon/kT}} \qquad 5.5$$

where $A = \frac{I_0}{d}$, $\epsilon = E - E_F$, k is the Boltzmann constant and T is the temperature.

The full width half maximum (FWHM) of 0.34 eV was obtained from the resulting energy spread curve. The resulting value is in the range of 0.2-0.4 eV, also obtained by other researchers for different kinds of field emitters[47][98][113]. The high energy spread value calculated in our case is due to the high emission current (1 nA), which agrees with previous studies[88].

The slope of the low energy side is proportional to $1/d$ (d is the tunnelling parameter), whereas on the high energy side it is proportional to $1/_{kT}$. In other words, the increase in width of the spectrum to the lower energy side is because of the enhanced tunnelling events below the Fermi level (Figure 5.21). Whereas, the heating effects at the tip surface explain the increase in width of the spectrum to the higher energy side [89].

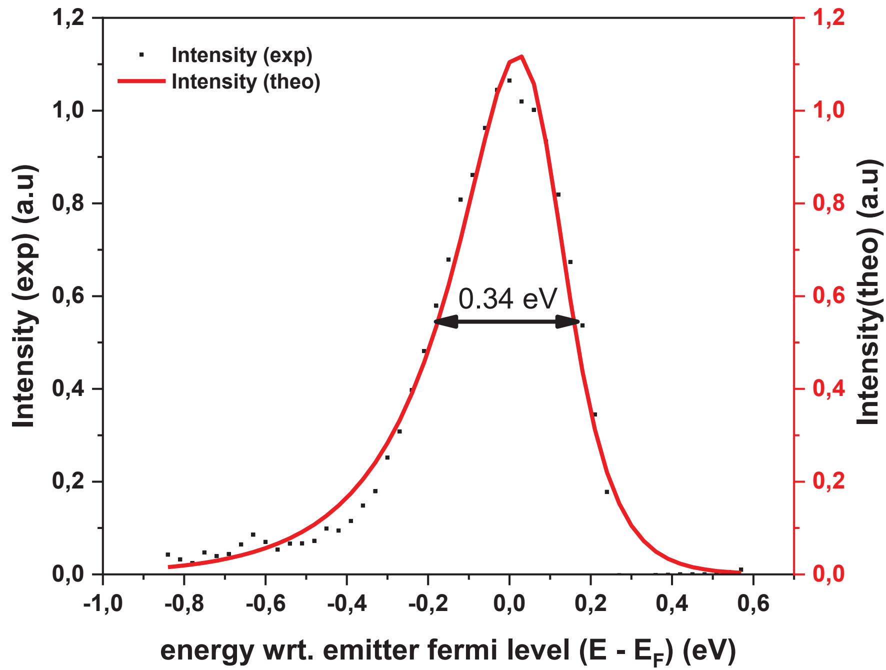

Figure 5.20 The total energy distribution (FWHM = 0.34 eV) of electrons emitted by the developed LaB_6 electron source. Theoretical model (Equation 5.5) fits (red curve) well with the experimental data (black dot)

Least-square fits of Equation 5.5 are in excellent agreement with the data for kT = 0.04-0.2 eV, which corresponds to the temperatures equivalent to 470K-2300K. However, all the measurements were taken at room temperature 300K (0.025eV). Local increases in apex temperature, analyzer broadening, and the Boersch effect[91] can explain this disagreement in experimental and theoretical values of temperature.

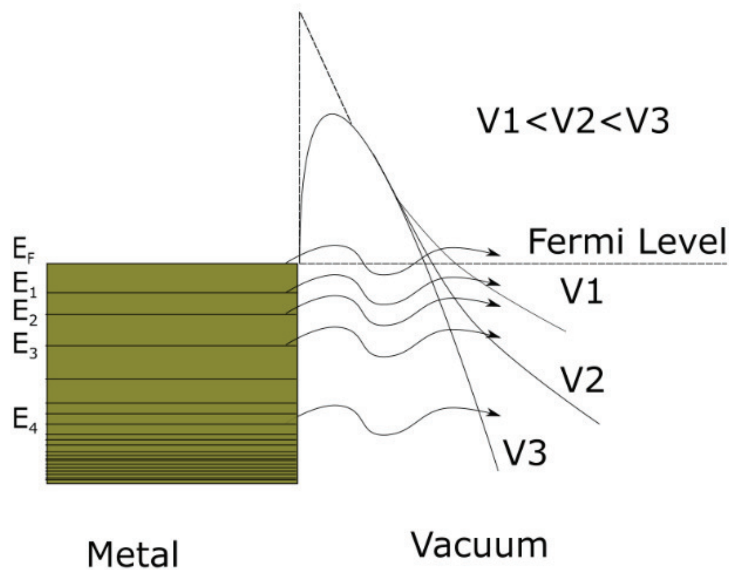

Figure 5.21 Increase in barrier slope with increase in applied voltage at constant work function and radius

The effect of the extraction voltage on energy spread is shown in Figure 5.22. The increase in energy spread with extraction voltage is attributed to the rise in emission current due to deep-lying energy levels[67].

At high current density, the surface heating effects are the main contributor to the energy spread [88]. These effects are dependent on the work function and the emission area of the electron source. The contributions of heating effects are needed to be quantified to understand the trend in Figure 5.22. Hence, numerical simulations were carried out and included in the next section.

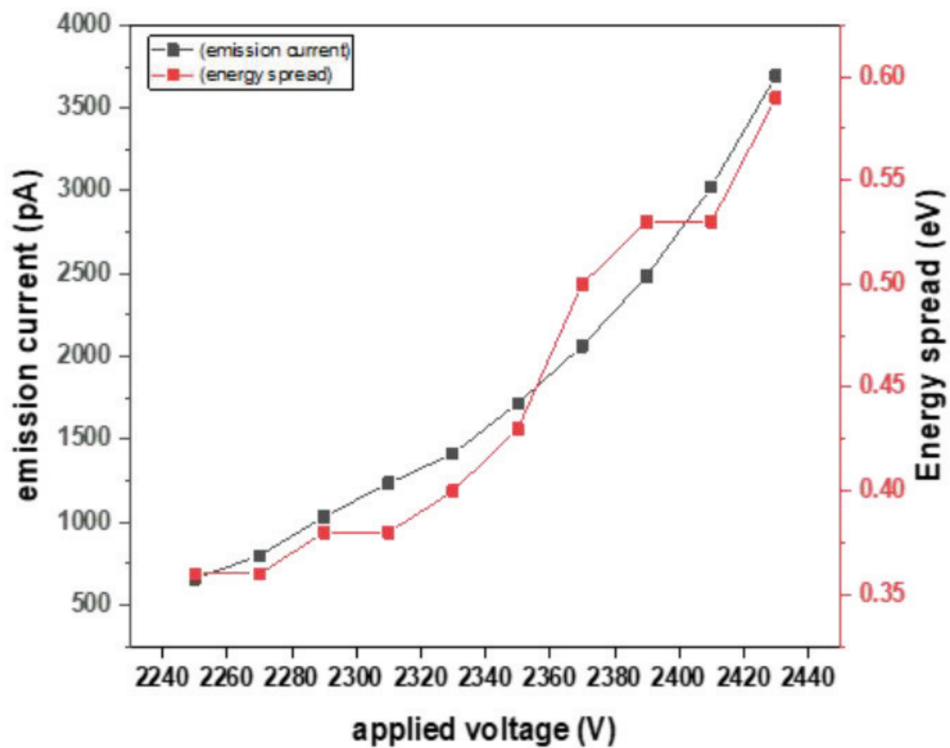

Figure 5.22 Plot showing the energy spread profile at different voltage and emission current

5.6 The temperature profile of fabricated tips during electron emission

During field emission, the temperature of the electron source rises because of the Joule heating induced by the emission current and the resistance of the emitter. The heat transfer to the substrate (conduction) and thermal radiation balances this rise in temperature. Thermal equilibrium among these processes ensures the stabilization of the field emission current. However, this equilibrium can be lost if the emission current increases above a critical value. This non-equilibrium condition then results in a thermal runaway situation that raises the temperature above the melting point of emitter apex

resulting in its destruction[169][108]. Another factor that determines the longevity of a tip is the field stress at the emitter surface. If this stress becomes more substantial than the surface tension of the emitting tip, disintegration can occur below its melting point[174]. In this section, the relation between emitter radius, vacuum environment, surface irregularities, maximum emission current, temperature, and time to reach the melting point of the emitter is established to understand the importance of fabricated LaB_6 tip over W tips in a greater context. Before presenting the detailed simulation results, it is vital to understand the Nottingham effect[175], a phenomenon that is accompanied by Joule heating during the electron emission.

5.6.1 Nottingham effect

For many years it was believed by the researchers that the tip emitters get destroyed when the thermal equilibrium between heat gain (Joule heating) and heat loss (radiation and conduction) disrupts during electron emission[67]. However, Swanson and Levine[176] experimentally and theoretically proved that the electron energy exchange mechanism plays a dominant role in thermal equilibrium.

According to Swanson *et al*. [175], in-room temperature field emission, the electrons tunnel out from the Fermi level or the energy levels below it. The electrons from the electrical wires connected to the emitter replace those tunnelled electrons and reach to the Fermi level of the emitter. These incoming electrons have the energy (E_F) higher than the electrons tunnelled from energy level (E^{1c}) below the Fermi level, as shown in Figure 5.23. The extra energy ($\Delta E = E_F - E^{1c}$) dissipates near the surface within the range of the mean free path of electrons[175]. This energy exchange is a quantum mechanical phenomenon and is known as the Nottingham effect. At low current density, the contribution of the Nottingham (cooling) effect is not significant. However, at a high current density, this effect dominates over the Joule heating energy dissipation Figure 5.23.

The collective contributions of the Joule and Nottingham heating effects cause a rapid temperature rise in the emitter tip. This upsurge in temperature transports the electrons occupying low energy levels (below E_F) to higher ones (closer to E_F). These processes continuously work together until the inversion temperature (T_{in}) is reached, where the energy of incoming electrons from the external circuit equilibrates with that of energy (E^{2c}) of electrons that are excited by the dissipated heat. This results in the termination of the energy exchange between external and internal electrons, and hence the Nottingham (heating) effect vanishes.

In parallel to the Nottingham heating, Joule heating also contributes to the increment of temperature. It does not depend on the energy exchange mechanism but the magnitude of current and resistance. At higher current density, the Joule heating disrupts the energy exchange equilibrium and hence increases emitter temperature beyond T_{in}. At this point, the Nottingham cooling effect comes into the picture[169][46]. This energy exchange mechanism brings down the temperature of the tip apex to reach back to the thermal equilibrium, which disrupted at higher current density.

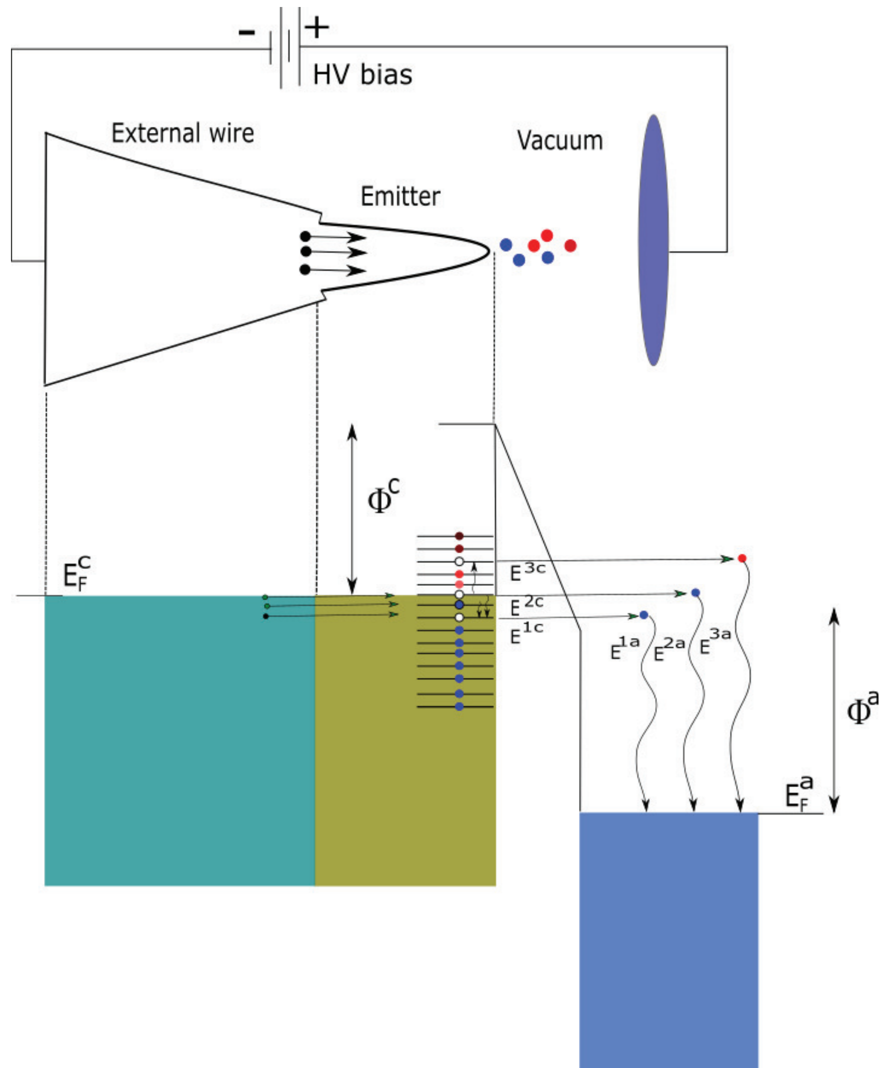

Figure 5.23 Schematic showing Nottingham (heating and cooling) effect during electron tunneling of cold (blue dots) electrons and hot (red dots) electrons. At an equilibrium temperature T_{in}, electrons are released from fermi level and Nottingham effect vanishes. The extra energy carried by hot electrons (red dots) is released to the anode that act as a sink.

At temperatures, $T > T_{in}$, the energy levels above E_F also become available to the electrons, as shown in Figure 5.23. The electrons that reach E_F from external wires have energy less than newly available energy levels. These newly arriving electrons get scattered to E^{3c} from E_F and hence lower the overall energy by E^{3c} - E_F resulting in cooling down the emitter, as shown in Figure 5.23.

Levine [176] derived expressions for inversion temperature T_{in} (K) and average exchange energy per emitted electron ∈ (Joule) as follows:

$$T_{in} = 5.8 \times 10^{-5} \frac{F(in \frac{V}{cm})}{\sqrt{\emptyset(in\, eV)}} \tag{5.6}$$

$$\in = -\pi kT \cot\left(\frac{\pi T}{2T_{in}}\right) \quad 5.7$$

where the symbols have their predefined meanings. The Nottingham effect is included (Equation 5.9) in the simulations used to study the temperature profile in the apex region.

5.6.2 Theoretical study of fabricated tip emitter temperature profile

Figure 5.24 shows the nanotip model used in the simulation to understand the thermal effects. This geometry resembles the fabricated field emitters in the present work. Identical model for both W and LaB_6 tips were used for normalizing the field enhancement factor that strongly depends on the radius of the tip apex and geometry of the shank at the same voltage[75].

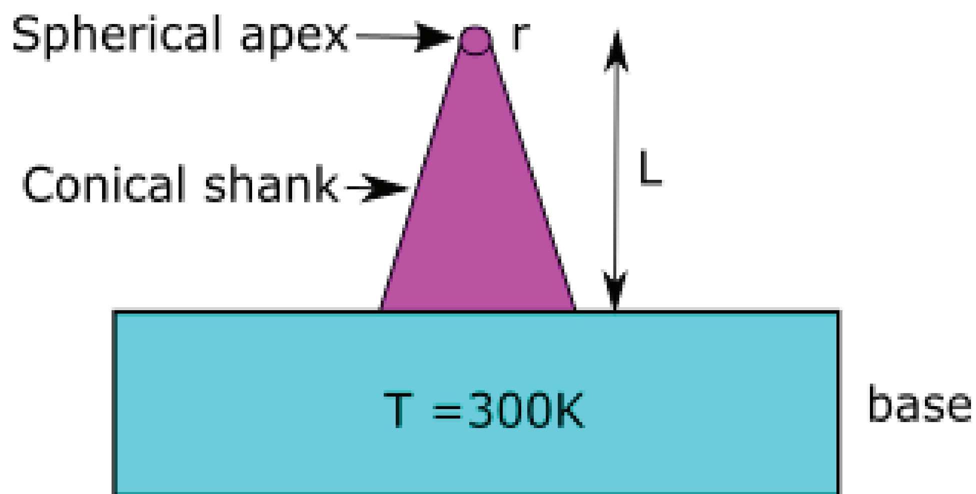

Figure 5.24 Field emission model of fabricated W and LaB6 tips

In this study of the fabricated emitter temperature profile, the following assumptions are taken into account:

1. The temperature of the base (several microns away from tip apex) consisting of bulk LaB_6 is assumed to be 300 K.
2. The classical hemisphere-on-conical-shank geometry[75] is assumed to approximate the fabricated field emitter geometry.
3. The shape of the emitter is assumed to remain intact at a very high (10^9 V/m) electric field.
4. Whole tip surface is contributing to electron emission.

1D time-dependent heat equation with a heating source term and dissipation terms can be expressed as follows[67][117]:

$$\delta C_p(T)\frac{dT}{dt}dx = \rho(T)j^2\,dx + k\frac{d^2T}{dx^2}dx - \frac{2}{r}dx\sigma(T^4 - T_0^4) \qquad 5.8$$

where the terms and their values for both (W and LaB_6) are shown in Table 3. The left side of Equation 5.8 describes the rate of change of temperature. On the right-hand side, the three terms correspond to the Joule heating, heat conduction, and heat loss due to radiation, respectively. As mentioned in subsection 5.6.1, the energy exchange mechanism (Nottingham effect) plays a vital role in setting up a thermal equilibrium at a high current density. This effect is included in the boundary condition (Equation 5.9) for the tip apex to solve the time-dependent heat equation.

$$\frac{dT_A}{dx} = [-\frac{\sigma({T_A}^4 - {T_0}^4) + \frac{j}{e}\in}{k}] \qquad 5.9$$

For W, using 5.7 and Table 3, this becomes:

$$\frac{dT_A}{dx} = \left[-2.9\times10^{-10}\times T^4 + 2.34 + j\times1.6\times10^{-6}\times T\times\cot\left(1.6\times\frac{T}{T_{in}}\right)\right] \qquad 5.10$$

and for LaB_6:

$$\frac{dT_A}{dx} = \left[-3.4\times10^{-9}\times T^4 + 27.55 + j\times1.8\times10^{-5}\times T\times\cot\left(1.6\times\frac{T}{T_{in}}\right)\right] \qquad 5.11$$

From Equation 5.10 and 5.11 it can be observed that at a particular current density, the temperature gradient at both the tip (W and LaB_6) apex will differ significantly only because of the $\cot\left(1.6\times\frac{T}{T_{in}}\right)$ term. Equation 5.8 was solved with *MATLAB pdetool* for both emitters and is plotted, as shown in Figure 5.25. The code is included in *Appendix 2*. It can be observed from the simulated results that for the same

geometry and radius, the LaB_6 tips should emit around 18 times more current than the W tips before thermal imbalance initiates.

Property (unit)	Symbol	W	LaB_6
Density (*kgm*$^{-3}$)	δ	19250	4720
Heat capacity (*Jkg*$^{-1}$*K*$^{-1}$)	$C_p(T)$	$135 - 6.5 \times 10^4 \times T^{-2} + 9.1 \times 10^{-3} \times T + 2.3 \times 10^{-9} \times T^3$	$0.18 \times T + 1.3 \times 10^{-3} \times T^3$
Resistivity (*Ω-m*)	$\rho(T)$	$2.3 \times 10^{-10} \times T - 2.2 \times 10^{-8}$	$3.3 \times 10^{-10} \times T - 9.7 \times 10^{-8}$
Thermal conductivity (*Wm*$^{-1}$*K*$^{-1}$)	k	173	14.7
Emitter apex radius (*m*)	r	7×10^{-8}	7×10^{-8}
Room temperature (*K*)	T_0	300	300
Inversion Temperature (*K*)	T_{in}	$2.5 \times 10^{-5} \times F(in \frac{V}{cm})$	$3.7 \times 10^{-5} \times F\ (in \frac{V}{cm})$

Table 3 Parameters of W [177]–[179] **and LaB_6** [180]–[185] **used for simulating the temperature profile at the emitter surface**

Such a high maximum emission current with LaB_6 tips is attributed to its relatively low work function compared to W. To understand this, let us recapitulate that the F-N equation can be written in a modified form as:

$$I = a * F^2 * \exp\left(-\frac{b\emptyset^{3/2}}{F}\right) \quad 5.12$$

where $a = \frac{A}{\beta^2}$ and $b = \beta B$. Rest of the symbols have predefined meanings (see Chapter 2). Equation 5.12 shows that for a constant current the exponential factor must be constant i.e.

$$\frac{\emptyset^{3/2}}{F} = C \quad 5.13$$

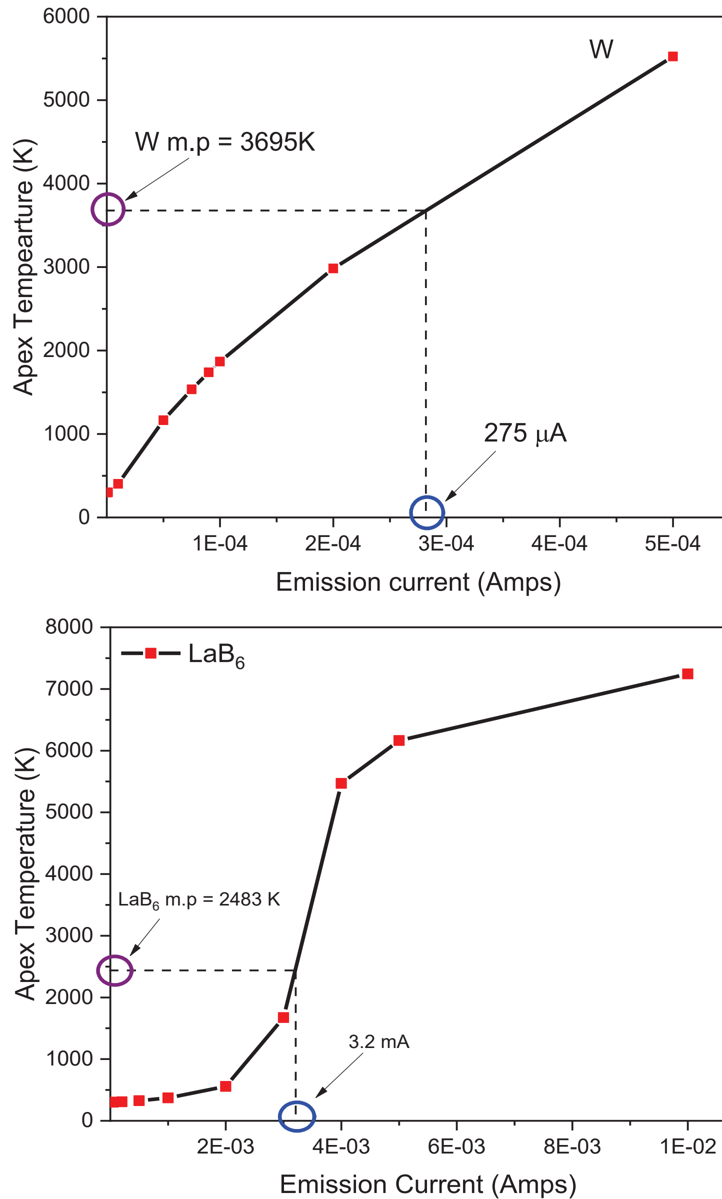

Figure 5.25 Plots showing the rise in apex temperature of W emitter (top) and LaB_6 emitter (bottom) during field emission and the blue and purple circles depicting the maximum emission currents before melting of tip starts, respectively

Combining equation (5.1) and (5.2) gives the following expression:

$$T_{in} = 5.8 \times 10^{-5} \frac{\emptyset}{C} \quad 5.14$$

Equation 5.14 implies that a low work function material has a low T_{in}. In other words, the Nottingham cooling mechanism turns on at a much lower temperature compared to the material having high work function. Hence, thermal equilibrium establishes before the emitter temperature reaches its melting point.

The melting point of LaB_6 (2483 K) is lower than that of W (3695 K). At a particular voltage (or field), for the safe field emission operations of both tips, their corresponding T_{in} must be lower than their melting point. The voltage (or field) at which T_{in} becomes just higher than their melting point, sets the maximum current limit of that particular field emitter. Figure 5.26 depicts that at approximately 2000 V, LaB_6 can comfortably emit 200 μA as the corresponding T_{in} is 2050 K which is lower than its melting point. However, for roughly the same emission current value W requires 5695 V at which the T_{in} value is 4100 K which is much higher than the melting point. Hence, for W tip with the same shape and size of LaB_6, it is not possible to emit the same current before its destruction.

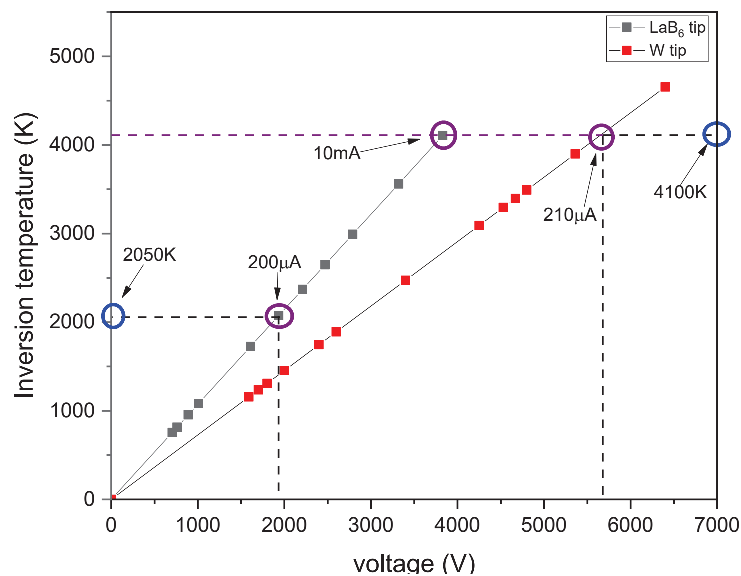

Figure 5.26 Plots showing that with same geometry for LaB_6 (black dot) and W (red dots), it is impossible for W to emit approximately 200 μA current before its destruction that LaB_6 can comfortably emit

In this thesis work, the field emission current from the developed LaB_6 electron sources is limited to the range of 100 pA to 10 nA. Two processes always work together to destroy the field emitters. First is the sputtering of the electron source by the desorbed ions from the anode, as discussed in 5.3.1, also found by previous researchers[186]. These ions change the apex structure by deposition of the energy proportional to the applied voltage. The ion collisions form craters and sharp asperities on tip apex results in local field enhancement. The local field enhancement at these nano-structures increases the emission current density exponentially, which results in a thermal runaway within a short time. Once the apex temperature goes beyond the melting point of the emitting material, the tip melts and halts the emission. Second is the buildup process, in which the electric field gradient force drives the adatoms[76]. It results in the formation of nanoprotrusions, and hence thermal runway occurs due to very high emission current from these structures.

The covalent bonding in boron octahedral structures provides enhanced robustness to LaB_6 [187][188][160] compared with the metallic bonding in W[160]. This unique structure of LaB_6 makes it's surface 5-10 times harder than W. In addition to this, the low work function of LaB_6 allows the same current as W at a lower extraction voltage. The ion sputtering of the cathode depends proportionally on the extraction voltage. It implies that for the equal emission current value, LaB_6 experience less destruction than W. The combination of inherent properties (high surface hardness and low work function) gives an advantage of less destruction to LaB_6 over W at low vacuum (or higher pressure) environment. That's why it was possible to operate LaB_6 at 5×10^{-9} mbar, which is not possible for W.

All the above points can be summarized as follows:

a) Due to low work function, the Nottingham cooling mechanism in LaB_6 starts much sooner than for W.
b) Due to low work function and covalently bonded boron structure in LaB_6, the damage due to ions in the vacuum chamber is also less compared to W at the same current density.

These inherent advantages of LaB_6 make it a practical field emitter electron source that can be operated in less stringent vacuum conditions unlike W. The aim of this thesis was not just the development of an electron source but also to generate microsecond electron pulses. Hence, the potential of the developed source was tested in pulse mode. The resulting electron pulses were characterized, and the results are included in the upcoming section.

5.7 Generation and characterizations of microsecond pulses from fabricated LaB_6 emitters

As discussed in section 2.4, high-resolution single-shot phase contrast electron microscopy demands a pulsed bright electron source. Every electron microscopy application has some electron source requirements which must be fulfilled for getting promising results (see section 2.4). In the case of single-shot phase-contrast imaging, there is the requirement of an electron source that can supply 10^8 e^- per pulse, while maintaining a reduced brightness in the range of 10^7 - 10^8 $Am^{-2}Sr^{-1}V^{-1}$ to get a high-resolution image on the detector. The purpose of this thesis is to develop an electron source to probe μs processes in biological samples. Hence, the capability of the established LaB_6 electron source was tested in the μs regime to recognize its limit to which it can fulfil the requirement of the needed electron source.

5.7.1 Enhancing the longevity of the electron source

The developed LaB_6 electron source was pulsed electronically using an in-house developed pulse generator (see section 5.7.2). Field emitters have an advantage of an inherent cooling effect (Nottingham cooling) that helps mitigate failure at higher current density as discussed in 5.6.1. The Nottingham effect, however, is confined to the region close to the apex of the field emitter whose thickness is in the order of the electron-

phonon mean free path Λ [67]. It is important to note that this effect can prevent failure of the tip apex only if it overcomes the heating effects such that thermal equilibrium is achieved below the melting point. In the high current density regime, however, some other processes which hamper the establishment of this thermal stability are discussed below.

In the presence of high field strength, minute surface irregularities like nanoprotrusions and sharp ridges form on the apex surface. These irregularities are the outcome of surface diffusion processes on the emitter surface governed by the migration activation energy of the atoms which is a function of the field gradient, surface tension, temperature and material[189][154]. The protrusion of these atoms results in a localized rise in current density to values up to 10^{12} Am^{-2}, and hence, confined rapid heating occurs resulting in tip failure[67]. Fursey *et al*.[190] demonstrated that under ultra-high vacuum condition (< 10^{-10} - 10^{-11} mbar), the formation of these minute irregularities depends on the magnitude of the current density and time duration of field emission operation. The Joule heating in the emission process provides the activation energy for the surface diffusion of the apex adatoms, and the time duration determines the degree of diffusion induced arrangement of atoms[189]. The electric field together with Joule heating drives the adatoms and initiate the build-up process [76]. These processes can be minimized by a trade-off between emission current and pulse duration for a stable and long-lived cathode operation.

It is important to note that the diffusion processes discussed above are unavoidable even for a clean cathode surface. These processes get enhanced if the emitting surface is prone to adsorption processes and not robust enough to sustain the sputtering events (section 5.6.2) which frequently occur in a relaxed vacuum environment (>10^{-9}-10^{-10} mbar). Hence, the pulsed-field emission from a LaB_6 emitter can make it possible to realize the high currents as achieved previously[67] but also in the degraded vacuum conditions.

In the present work, the pulsed-field emission was realized by the μs train of extraction voltages with 100Hz repetition rate. To this end, a high voltage μs pulse generator was developed as outlined in the next subsection.

5.7.2 In-house developed microsecond high voltage (μs-HV) pulse generator

The extraction voltage of the LaB_6 field emitters was triggered using microsecond rectangular DC pulses with rise and fall times of about 10 nanoseconds, and 0.1% duty cycle. The solid-state HV switch used in this pulse generator was purchased from Behlke power electronics (Model: HTS 121-01-C). The combination of the optimized resistance-capacitance (R-C) network with the switch made it possible to generate μs pulses of 5kV amplitude. The minimum required length (10 cm) of a well-shielded cable was used to avoid the parasitic capacitance effect. The circuit diagram of the developed pulse generator is shown in Figure 5.27.

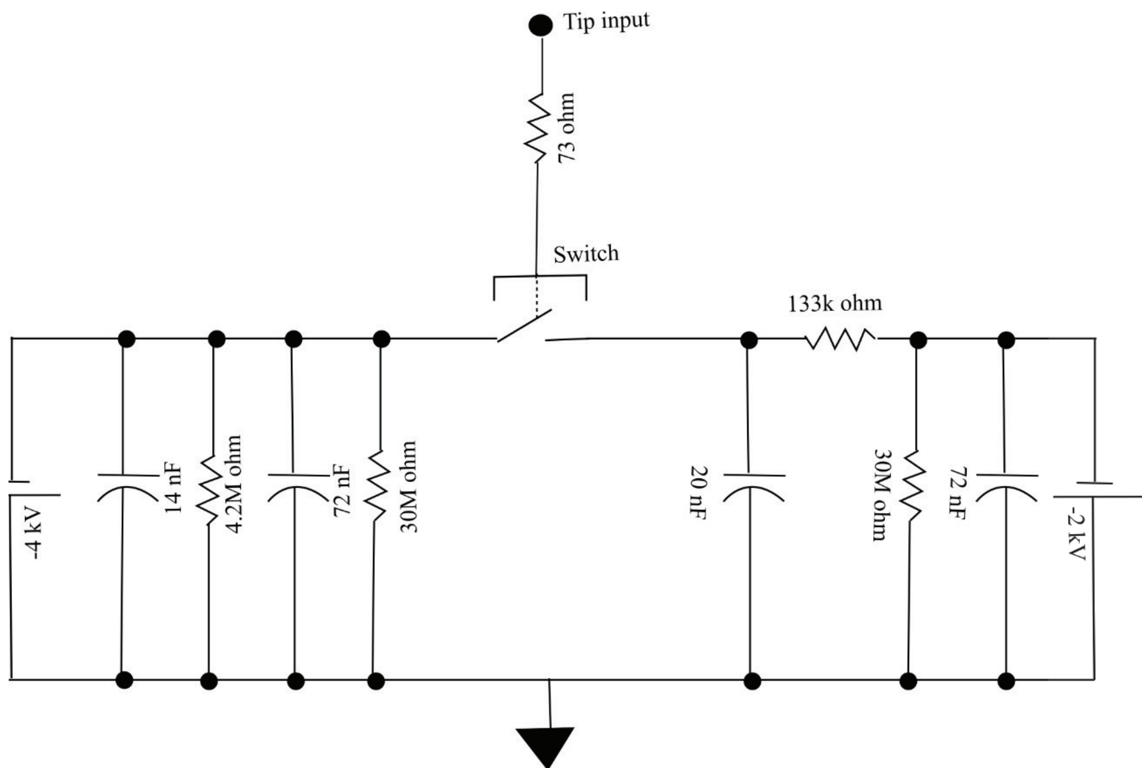

Figure 5.27 Circuit diagram of in-house developed high voltage pulse generator used to produce (1-10) μs pulses

5.7.3 Generation of high current pulses

The internal setup of the test chamber for the generation and detection of the microsecond pulses was kept identical as for the field emission measurements (Figure 5.1). Two modifications in the setup were done externally. First, the voltage supply to power the electron source was replaced with the developed pulse generator. The width of the extraction voltage pulse was varied from 1-10 μs at a fixed repetition rate of 100 Hz to record the data. The continuous monitoring of the output pulse was performed using a high voltage probe (Testec TT-HVP 40MHz) connected to an oscilloscope (Agilent MSO-X 3034A) before being connected to the cathode. Second, to detect the current signal, the picoammeter was replaced with a scheme of transimpedence amplifier (FEMTO DHPCA-100) aided oscilloscope (Figure 5.28). It was assured that the external wires were shielded appropriately to avoid or reduce the effect of electrical noise and electromagnetic interference (EMI) in the measurement. The shape of the tip apex was monitored regularly using the MCP/phosphor assembly, and the CCD camera.

As explained in section 5.7.1, a trade-off between pulse width and maximum extraction voltage was needed to get a stable and long-lived field emission. This trade-off sets the maximum peak current possible from a field emission source. The maximum peak current for 10μs pulses was estimated by fixing the repetition rate to 100 Hz and ramping up the magnitude of the DC extraction voltage to the point at which rapid fluctuations in current were observed. On increasing the extraction voltage beyond that

point resulted in excess emission current (>50-100μA) for a very short time (1-5 sec) followed by the tip failure.

The value of peak extraction voltage and corresponding peak current for the present LaB_6 field emitter was in the range of 4-4.6 kV and 8-11 ± 0.01 μA respectively (Figure 5.29 top). The peak emission current was very stable and the current did not drop more than 10% even after 2-3 hours of continuous operation at a vacuum level of 5×10^{-9} mbar. After 3 hours, however, the reduction in the peak current level was 20-30%. This lowering of peak current was possibly due to the adsorption of residual gas species on the surface by prolonged operation of the tip in a poor vacuum condition[158]. The shape of the tip apex was monitored after every two hours of operation. A beautiful single spot indicates that no new emission regions had evolved and hence the apex shape remained intact at a current of 11±0.01μA (Figure 5.29 bottom).

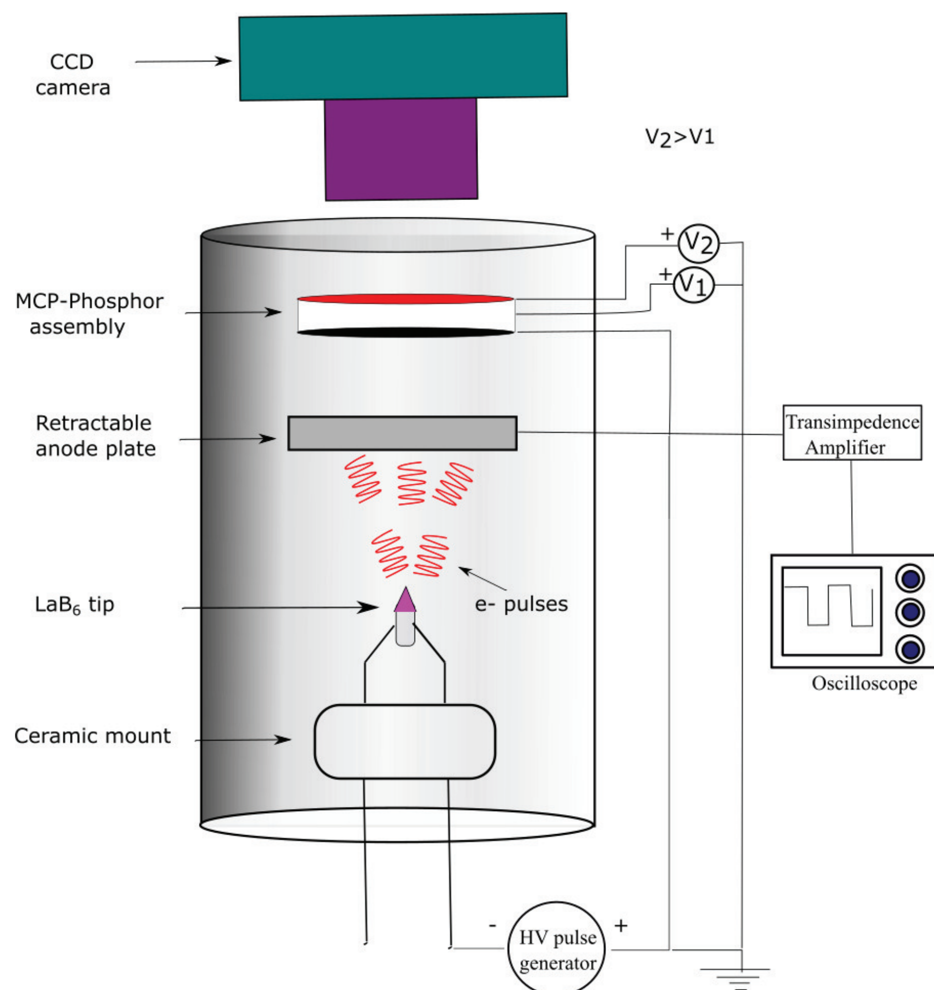

Figure 5.28 Illustration of the experimental setup used to generate and detect microsecond electron pulses

The electronic pulsing of the LaB_6 field emitter combined the inherent advantages of robustness and low work function of LaB_6 with the mitigation of build-up processes

through pulsing. Hence, an emission current over 10µA at a vacuum level of 5×10^{-9} mbar was observed.

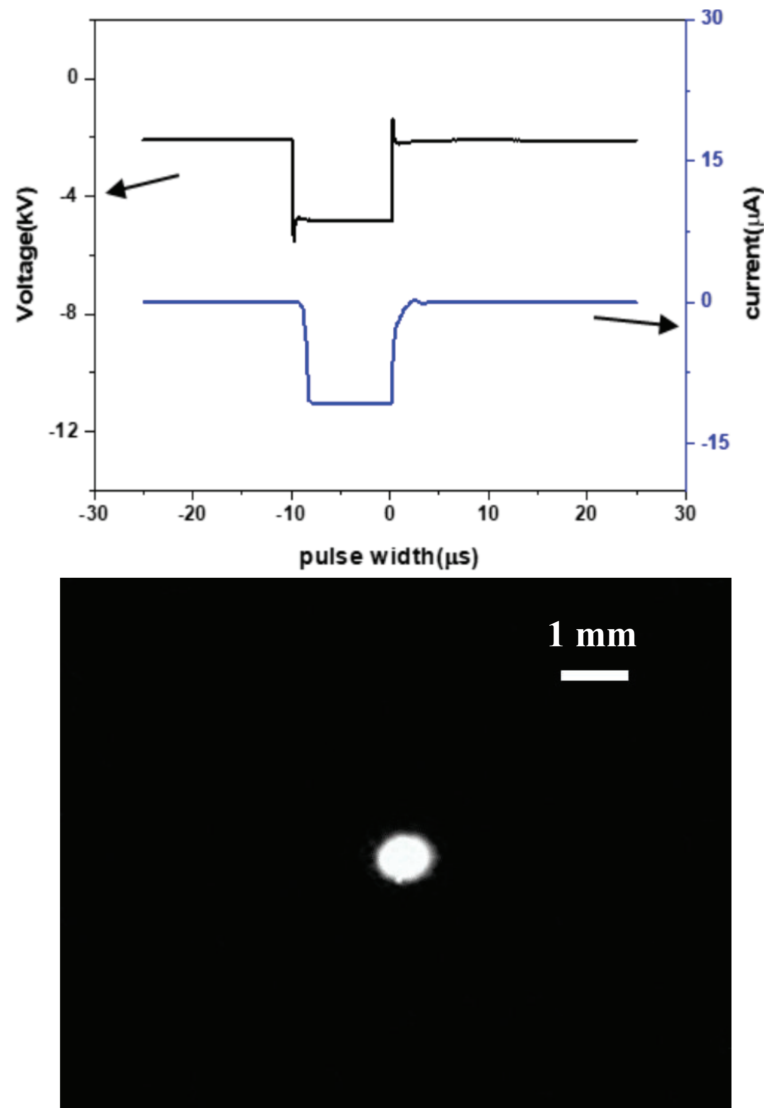

Figure 5.29 (top) Plot of data collected with oscilloscope showing 10µs pulse emitting 11µA peak current at 4.6kV peak voltage, (bottom) phosphor image of 10µs electron pulses carrying 11µA averaged over 1s time

5.7.4 Characterization of the high current microsecond pulses

The high current field emission electron pulses were characterized to quantify the quality of pulses. Similar to continuous field emission characterization, both the fundamental properties: angular current density and energy spread were measured.

a) Angular current density

The experimental setup to record the angular current density was identical to the system used to generate the electron pulses shown in Figure 5.31. The only change was the integration of the nano manipulator controlled aperture plate that was used to measure

the current density of the continuous field emission current (Figure 5.15). The same methodology of measurement was used as with the continuous beam. First, the calibration process was performed, as described in section 5.4. Subsequently, the aperture scan of the electron pulses was done. For the current LaB_6 emitters, in a continuous field emission case, a 200µm aperture delivered the maximum angular current density (Figure 5.16). Hence, the same aperture was used to measure the angular current density of the electron pulses for a better comparison.

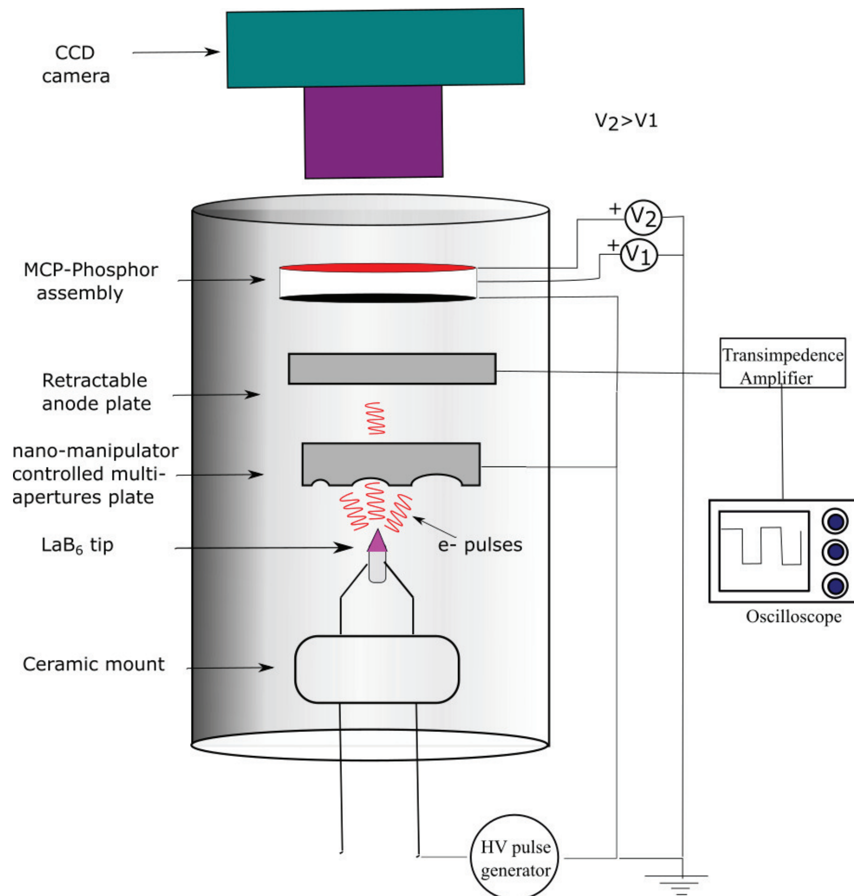

Figure 5.30 Schematic of the setup to measure the angular current density for 10 µs electron pulse. The difference in this arrangment compared to measurements with continuous beam was the incorporation of pulse generator in place of continuous power supply and transimpedence amplifier aided oscilloscope in place of picoammeter

Figure 5.31 shows an angular current density graph using a 200 µm aperture. The angular current density was estimated using the formula stated in Equation

5.4. The resulting value (9.5 ± 0.1 µA/Sr) was found to be in the same order as that measured for the continuous beam (8.3 ± 0.1µA/Sr). Hence, it implies that pulsing has no significant effect on the maximum current density indicating that the high brightness property of the field emitters does not get affected by the pulse extraction voltage, at least in the microsecond regime.

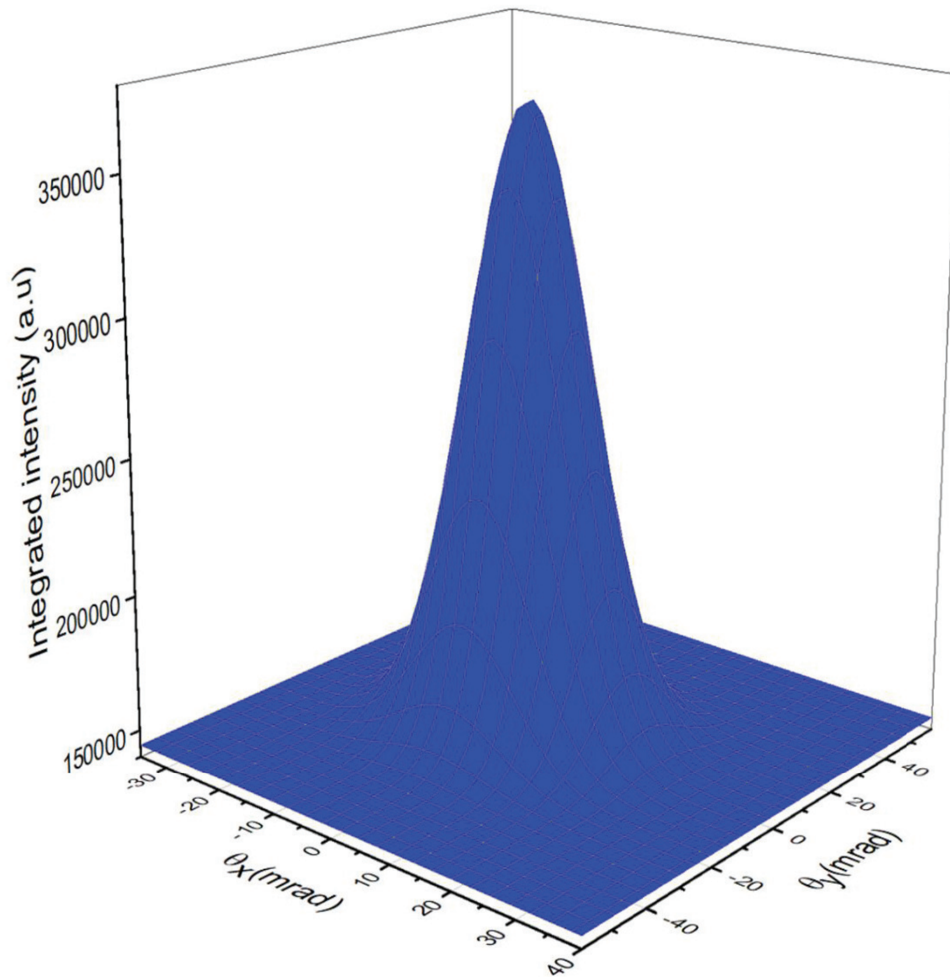

Figure 5.31 3D plot showing the variation of integrated intensity along semi-angles θ_x (along the x-axis) and θ_y (along the y-axis) for 200µm aperture. The peak current was 10-11 µA, at 4.5-4.6 kV peak extraction voltage was applied. The angular current density of 9.5 ± 0.1 µA/sr calculated from this plot shows no significant change compared to continuous field emission beam.

b) Energy spread

The energy spread of the generated pulses was measured using the experimental setup shown in Figure 5.32. The system resembles the arrangement used for energy spread measurement of the continuous beam (Figure 5.17). In the present configuration, however, the cathode was powered using the pulse generator and the generated pulses were detected using the MCP/phosphor assembly. The methodology of the data collection was similar to what was used for the continuous beam(refer section 5.5). The energy spread measurements were performed in the range of 2.8 kV - 3.2 kV (steps of 100V). The maximum energy spread of magnitude 0.9eV was observed at 3.2kV (Figure 5.33), which is about 0.3-0.6 eV higher than the energy spread recorded with the continuous beam (Figure 5.22).

The energy spread of an electron pulse is affected by three components: Boersch effect, instabilities of the voltage source, and the inherent electron energy spread [191] as explained below.

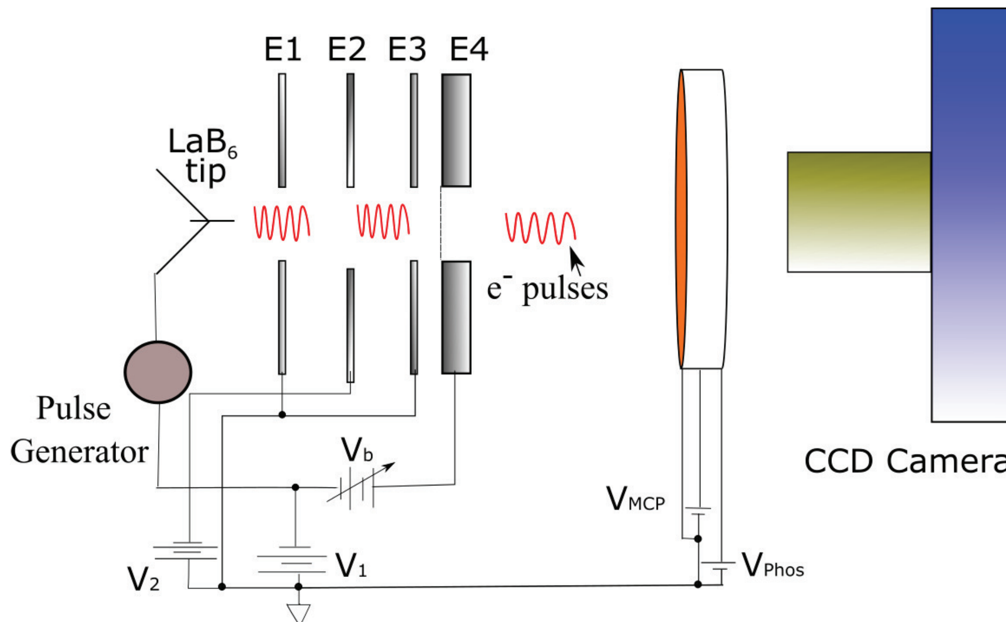

Figure 5.32 Schematic of the arrangement used to measure the energy spread of the generated µs electron pulses

The space charge effect term for an electron pulse of duration Δt accelerated using potential V and having N number of electrons with beam radius r can be expressed as [191]:

$$\Delta E_{sc} = \frac{e^2 N \Delta t}{8\varepsilon_0 \pi r^2}\sqrt{\frac{2eV}{m}} \quad 5.15$$

The extraction voltage pulse of 10µs duration and magnitude 2.8kV-3.2kV produced 100 - 500 nA peak current (~ 6×10^6 - 3×10^7). With the assumption that the beam radius r is equivalent to the apex radius (70 nm), the space charge contribution was estimated by substituting the above values in Equation 5.15. The resulting space charge value was found to be in the range of 10^{-4} – 10^{-5} eV, which is negligible.

The second component of the energy spread is the voltage instability of the pulse generator source. As illustrated in Figure 5.32, the high voltage power supply V_1 (iseg SHQ 226L) connected to the pulse generator was used as an excitation source. The voltage stability of V_1 is 0.003 percent of the input voltage, which is 0.1 eV for the voltage pulses in the ranges of 2.8 kV-3.2 kV. This value is 0.03-0.04 eV higher than the DC energy spread measurements. The ripple/noise contribution is 5mV peak to peak. The capacitor discharge voltage drop is given by:

$$dV = I_{peak} \times \frac{\Delta t}{C} \qquad 5.16$$

where I_{peak} is the peak current and C is the equivalent capacitance of the circuit. From Figure 5.27, C is 84nF which gives dV (using Equation 5.16) equal to 0.01-0.05 mV for 100-500 nA peak current. Hence, the total input of the excitation source in the energy spread is ~ 0.1 eV.

The maximum total energy spread was observed to be 0.9 eV at 3.2kV peak voltage, see Figure 5.33. This implies that the contribution of the third component, the inherent electron energy spread, is ~ 0.8 eV. The magnitude of this component depends on the participation of electrons occupying the energy levels near the Fermi level to the emission current.

The momentarily increased high peak extraction voltage compared to the continuous case enables the electrons present in the deep energy levels E ($E<E_F$) to tunnel out (Figure 5.21). It might explain the increase in the width of the energy spectra towards the low energy side, as observed previously[88].

The contribution of the thermal effect on the energy spectra can be estimated using Figure 5.25. It shows that the rise in surface temperature in LaB_6 is negligible for the 100s of nA current level used in the energy spread measurements which implies that thermal effects are not playing any significant role in the increment of the width of spectra.

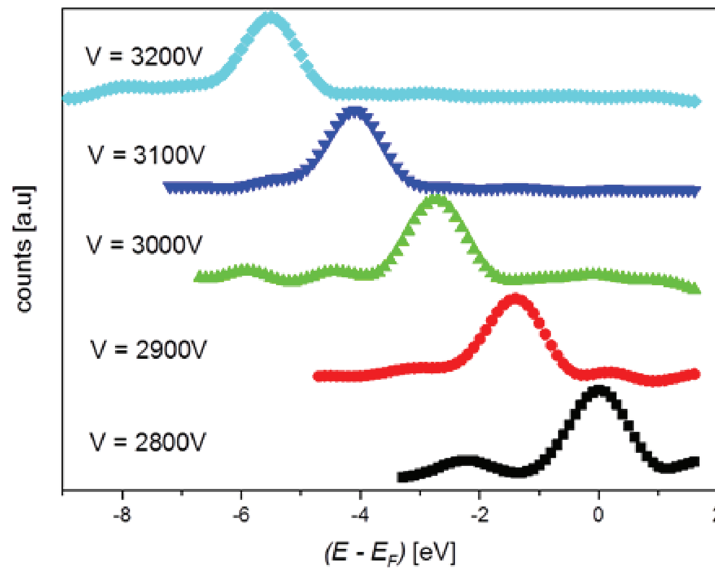

Figure 5.33 Plots of the energy distribution of 10µs electron pulses emitted by the LaB_6 field emitter as function of energy with respect to Fermi level. A shift in the peak towards the low energy side is observed as the extraction voltage is increased.

In addition to the increase in energy spread, an interesting pattern was observed. Unlike metallic emitters, the peak of the distribution does not persist in the vicinity of a

Fermi level, but shifts linearly with voltage, as plotted in Figure 5.34. Linear least-squares fits are in excellent agreement with the data for slope = -14.1 meV/V. The origin of this linear peak shift might be due to the electric field penetration, as argued by Fransen et al. [171]. In the presence of high voltage, the corresponding high local field can evaporate the La atom from the surface of the LaB_6 emitter. It can cause the deficiency of conduction electrons in the boron octahedral network provided by the La atom (refer section 5.3.2). Hence, electric field penetration is quite possible in the LaB_6 through the electron-deficient boron layer as observed previously in LaB_6 nanowires[49]. A detailed surface study could confirm this hypothesis, but is outside of the scope of this thesis.

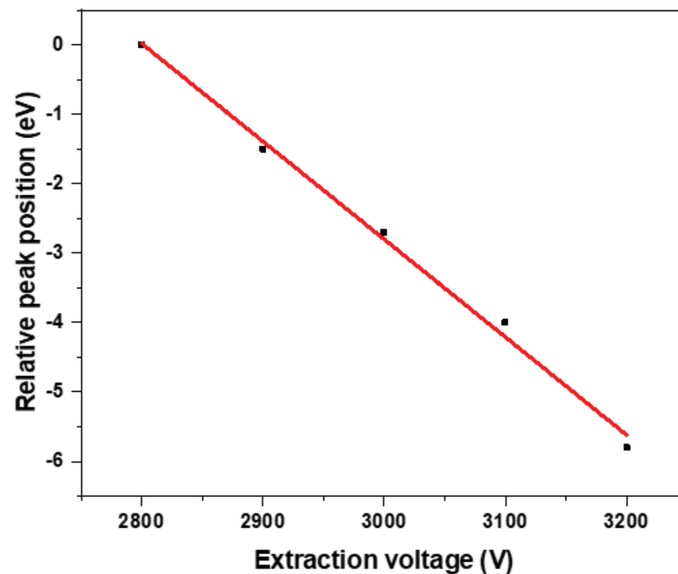

Figure 5.34 A plot illustrating the relative peak position of the energy distribution of electrons emitted by the LaB_6 as a function of the extraction voltage. Unlike metallic emitters, a linear decrease in position is observed as the voltage increases. A linear least-squares fit drawn through the data points. The slope of the fit is −14.1 meV/V

5.8 Summary

In this chapter, the fabricated LaB_6 characterization results were presented. The vital parameters I-V behaviour, temporal stability, angular current density, and energy spread of an electron source were investigated. Furthermore, high current (3 orders of magnitude larger than the continuous beam) μs electron pulses were generated and characterized. It was observed that the angular current density was not affected by pulsing, whereas a wider energy distribution was observed compared with continuous field emission. To further explore the potential of the developed electron source, it is essential to determine the reduced brightness. In the next chapter, the concept and results of reduced brightness are discussed.

6 Development of a coherence measurement setup: towards brightness estimation

This chapter is dedicated to theoretical discussions on brightness and the development of a point projection setup used to measure the electron beam coherence. It begins with a brief discussion on the concept of the reduced brightness[64]. In the same section, parameters like ultimate brightness limit B_{max}, degeneracy δ, and spatial coherence length L_{sc} are included to give the readers an insight into the quantum formulation of brightness. Subsequently, the comparison of present LaB_6 electron source and state-of-art bright field emitters in terms of their reduced brightness, B_{max} and δ are made in this chapter. The chapter concludes with the discussion on the development of an optimized point projection microscope to measure the L_{sc} of the electrons emitted by the present LaB_6 electron source, and the results obtained therewith are discussed in detail.

6.1 Theoretical concepts

6.1.1 Reduced brightness and limitation of its formulation

Brightness is defined as the angular current density j' per unit emission area ΔA. This parameter changes with acceleration voltage V, and hence not the best figure of merit for the electron sources. Normalizing the brightness to the V yields the reduced brightness B_r which can be written as:

$$B_r = \frac{B}{V} = \frac{j'}{\Delta A V} = \frac{I}{\Delta A \Delta \Omega V} \qquad 6.1$$

where I is the emission current, and $\Delta\Omega$ is the solid angle. The definition of reduced brightness involves the area of emission A (Section 2.2.2), which is apparent for Schottky emitters and photoemission cathodes. For Schottky emitters, the confined zirconium oxide (ZrO) layer over W, and for photoemission cathodes, the area of excitation beam determines the area of emission. For field emission cathodes, however, quantify the area of emission is not so trivial. Previous researcher[75][192][64] indicates that for the macroscopic tip (diameter ≥ 100 nm), the emission spot is around 1-2% of the physical diameter. The fact that only a small portion of the physical size contributes to emission must be taken into account, to avoid brightness underestimation. In the present chapter, this point is considered to calculate the reduced brightness value and are presented in section 6.2.

An alternative method to determine the exact emission spot (or effective source size) is based on the interference method. Hence, it is necessary to understand the underlying physics behind this method which is formulated using quantum mechanics.

The next subsection is, therefore, dedicated to explaining the quantum aspect of the brightness.

6.1.2 Theoretical considerations of brightness and its quantum limitations

The formulation of brightness in quantum mechanics is based on phase space and coherence definitions[193]. Phase space is a 6-D (3 dimensions of position and 3 dimensions of momentum) vector space. At a particular instant in time, each electron in a beam is represented by a single point having a position and momentum coordinate as (r, p). The uncertainty principle determines the smallest possible phase-space volume (the cell), which is equal to h^3. The Pauli exclusion principle allows only two electrons (of opposite spin) per cell of the phase space.

The electron beam degeneracy δ is defined as the mean number of electrons (or points) per cell of the phase space. This quantity determines the quantum interference effects in a system with electron correlations[194]. The number of electrons Δn contained in a beam can be written in terms of the phase-space volume ($\Delta^3 p\ \Delta^3 r$) and degeneracy δ as:

$$\Delta n = \delta \times \frac{2\,\Delta^3 p\,\Delta^3 r}{h^3} \qquad 6.2$$

Using spherical coordinates, the momentum volume $\Delta^3 p$ can be written in terms of experimental parameters $\Delta\Omega$ and relativistic momentum p ($=\gamma m v$) and as follows:

$$\Delta^3 p = \Delta p_x \Delta p_y \Delta p_z = p^2 \Delta p \Delta\Omega \qquad 6.3$$

where Δp_x, Δp_y, and Δp_z are the infinitesimal momentum changes along x, y, and z-direction. For any time Δt, the corresponding spatial volume $\Delta^3 r$ of a beam passing through the cross-sectional area ($\Delta A = \Delta x \Delta y$) with velocity v in the z-direction can be written as follows:

$$\Delta^3 r = \Delta x \Delta y \Delta z = \Delta A v \Delta t \qquad 6.4$$

Substitution of Equations, 6.3 and 6.4 into Equation 6.2 one obtains the number of electrons Δn passing through area ΔA:

$$\Delta n = \delta \times \frac{2}{h^3} (p^2 \Delta p \Delta\Omega)(\Delta A v \Delta t) \qquad 6.5$$

The electron current density j is defined as the number of electrons Δn passing through the area of cross-section ΔA per unit time Δt. Using this definition of electron

current density j and substituting it into Equation 6.5 and 6.1, one obtains the expression for brightness B :

$$B = \delta \times \frac{2ev}{h^3}(p^2 \Delta p) \qquad 6.6$$

Clearly, δ is the most crucial factor that determines the brightness at a particular momentum (or accelerating voltage). For photons, there is no limit on δ as no fundamental restrictions apply to them. But for electrons the ultimate brightness limit B_{max} would be for $\delta = 1$ (exclusion principle). This gives:

$$B_{max} = \frac{2ev}{h^3}(p^2 \Delta p) \qquad 6.7$$

The relativistic expression which relates the energy and momentum is:

$$E^2 = p^2c^2 + m^2c^4 \qquad 6.8$$

Differentiation of Equation 6.8 and combining it with $p = \gamma mv$ and $E = \gamma mc^2$, one can get:

$$\Delta E = v\Delta p \qquad 6.9$$

Substitution of the de-Broglie's equation $\lambda = h/p$[13] into Equations 6.9 and 6.7 gives the final expression for B_{max} in terms of experimentally measurable parameters:

$$B_{max} = \frac{2e\Delta E}{h\lambda^2} \qquad 6.10$$

This expression relates the ultimate (quantum) limit of an electron source to the experimental parameter ΔE. The values of B_{max} for the fabricated LaB_6 field emitter is determined (section 6.2.) using the ΔE values that were measured and presented in Chapter 5.

The ultimate or maximum brightness is achieved when two electrons of opposite spin are present in a phase space cell of volume h^3. However, in a practical situation, this does not happen at all. To understand this, it is necessary to comprehend the wave property of the electron and its relation to the phase space volume of the cell.

The concept of wave coherence is divided into two types: longitudinal and transverse. The longitudinal coherence length L_{tc} is also known as temporal coherence length and is defined as the length along the propagation direction over which the electron wave has a phase correlation. It is determined by the wavelength (or velocity v) and the wavelength (or energy) spread of the wave[195][196]. It can be written as:

$$L_{tc} = vT_c \qquad 6.11$$

where T_c is the electron coherence time defined as the time over which electron wave does not lose its phase correlation along the propagation direction. The uncertainty principle relates T_c to the beam energy dispersion ΔE:

$$T_c = \frac{h}{\Delta E} \qquad 6.12$$

The transverse coherence length L_{sc} is also known as spatial coherence length is defined as the length along the transverse direction of the wave propagation over which the electron wave has a phase correlation. It depends on the wavelength λ, distance of the electron source from the specimen L, and the size of the electron source r [194][197]. It can be written as:

$$L_{sc} = \lambda \frac{L}{r} \qquad 6.13$$

Using Equations 6.11 and 6.13, the 3D coherence volume V_c of the electron wave can be written as:

$$V_c = L_{tc} \times L_{sc}^2 = vT_c \times A_{sc} \qquad 6.14$$

where A_{sc} is the square of L_{sc} and is known as the coherence area.

In other words, V_c is the volume ($\Delta^3 r$) in the spatial dimension that an electron wave occupies in the phase space. The uncertainty principle sets the minimal phase space volume of the cell for electrons in 6D phase space to h^3, i.e.

$$\Delta^3 p \times \Delta^3 r \sim h^3 \qquad 6.15$$

Using Equations 6.3 and 6.14 in Equation 6.15 one obtains the volume of the cell occupied by coherent electron wave in phase space as:

$$(p^2 \Delta p \Delta\Omega) \times (vT_c A_{sc}) = h^3 \qquad 6.16$$

Now using Equation 6.16 in Equation 6.5 and on doing some simple rearrangements, an expression for degeneracy δ can be obtained as:

$$\delta = \frac{j}{e} T_c A_{sc} = \frac{jh}{e\Delta E} A_{sc} \quad 6.17$$

From Equation 6.17, it is seen that, except for A_{sc}, all quantities can be easily calculated using experimental parameters. For calculating A_{sc}, the point projection system was developed in this thesis.

Using Equations 6.6 and 6.7, the degeneracy, can also be expressed as a ratio of the actual brightness B to the ultimate brightness B_{max} i.e.

$$\delta = \frac{B}{B_{max}} \quad 6.18$$

The actual brightness B can be expressed in terms of L_{sc} or A_{sc} by substituting Equations 6.17 and 6.10 in Equation 6.18:

$$B = \frac{2jA_{sc}}{\lambda^2} = \frac{2jL_{sc}^2}{\lambda^2} \quad 6.19$$

From this, it is clear that to estimate the brightness B, value of the L_{sc} is required. To measure the coherence length, a point projection microscope was designed and built during the course of this thesis (section 6.3). The width of the Fresnel fringes formed after diffracting at a sharp edge in a point projection microscope can be shown to be related to L_{sc} [194].

6.2 Results and developments

In this section, the value of reduced brightness B_r, ultimate brightness B_{max}, and degeneracy δ are calculated using the experimental data recorded in Chapter 5. In subsection 6.3.3, the development of a point projection experiment and challenges are presented.

6.2.1 Reduced brightness B_r

Equation 6.1, clearly shows that two parameters are needed to calculate the reduced brightness: a) Angular current density at a particular voltage and b) emission area. The angular current density measurements were presented in Chapter 5. The tip radius was estimated at 70 ± 5 nm using F-N plot. However, the emission takes place only from the small region on the tip (Section 2.2.2). Figure 6.1 illustrates that the nanosize tip apex act as a lens. In the absence of any external lenses, the Gaussian beam spot depicts the magnified projection of the effective source size of radius r_{eff}. By calculating the beam opening angle 2θ from the beam spot and substituting it in Equation 2.24, one can get the r_{eff}.

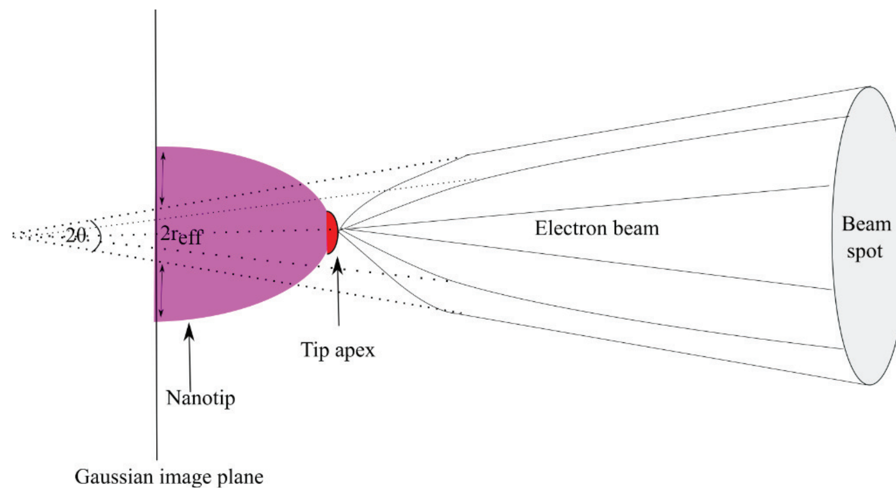

Figure 6.1 Illustration of the lens effect of the tip apex that gives rise to the finite effective source size of $2r_{eff}$. The rearward asymptotic extension (dotted lines) of the electron beam rays from the beam spot is cross the Gaussian image plane at a distance of $2r_{eff}$

Figure 6.2 depicts an FEM of the LaB_6 tip captured at 3.6kV. The beam profile indicates the Gaussian nature of the effective source [102][198][199]. The FWHM of length 0.83 ± 0.02mm corresponds to 1° beam opening angle. Using Equation 2.24, the corresponding r_{eff} is approximately 1 nm, which is 1.5-2% of the physical radius of the LaB_6 tip. This difference between physical radius (~70nm) and r_{eff} is in good agreement as observed theoretically and experimentally by the researchers in past[75][192][64][200][201].

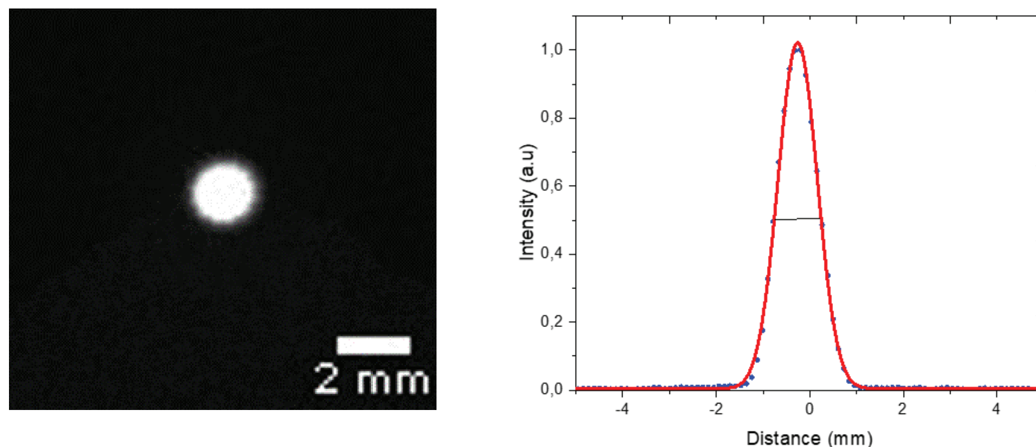

Figure 6.2 (left) FEM of the 70 nm LaB_6 tip at 3600V. A single circular spot on the phosphor screen with (right) the Gaussian beam intensity profile (FWHM ~ 0.8 mm) indicates the Guassian nature of effective source.

The angular current density was measured with 200μm aperture at 3.65kV using the experimental setup shown in Figure 5.14. On dividing the angular current density (=10 ± 0.1μA/Sr) by the effective emission area (3.14 nm^2) , one obtains the brightness value ~3.5×10^{12} A/m^2-Sr with a 200μm aperture at 3.65 kV for the fabricated LaB_6

source. This is equivalent to a reduced brightness $B_r \sim 1\times10^9$ A/m^2-Sr-V. The observed brightness is 5 times higher than the brightest Schottky emitters [62] and comparable to the results from carbon nanotube (CNT) cold field emitters reported so far [103]. It is important to note that the present LaB_6 field emitters can deliver reduced brightness similar to brightest field emitters currently available, but can be operated under poor vacuum conditions than those employed for the Schottky electron sources (10^{-9} mbar).

6.2.2 Ultimate brightness B_{max} and degeneracy δ

The ultimate brightness B_{max} as discussed in section 6.1.1, is the limit on brightness set by quantum mechanics. It can be estimated for a field emitter electron source using energy dispersion (ΔE) measurements. The maximum energy spread ΔE for the present LaB_6 emitter was 0.9eV (sections 5.5 and 5.7) measured at 3.2 kV (λ = 21.6 pm). Substituting the ΔE and λ values into Equation 6.10, one obtains $B_{max} = 1.5 \times 10^{18}$ A/m^2-Sr. The measured brightness value is $B = 7\times10^{11}$ A/m^2-Sr at 3.2 kV for 200μm aperture. This gives the degeneracy δ=5×10^{-7} for the present LaB_6 emitters, which 10-1000 times lower than the reported values for brightest nanotip emitters[103][194][202][203][204][205]. It must be noted, however, that the current (10nA) at which brightness is measured is 10-20000 times higher than in those experiments (0.5 pA-1 nA). The electron-electron scattering at high current density limits the degeneracy of an electron beam, which explains the lower value of the present LaB_6 emitters[206]. Jarvis *et al*. [207] showed resonant tunnelling emission of the electron beam from CNT and diamond field emitters with nearly quantum degeneracy (δ=0.1). However, a short lifetime (1s) of such emission make them undesirable for any imaging application[207]. Recently, two independent proposals were given by Zolotorev *et al*. and Claessens *et al.* to increase the degeneracy to unity by using ultracold plasma-based electron sources[208][209]. However, the compatibility of these electron sources with TEM has not been tested yet.

6.3 Lateral coherence length L_{sc} and the development of a point projection microscope (PPM)

A highly coherent electron wave in both directions, laterally and longitudinally, is provided by the field emitters. The longitudinal (temporal) coherence length (L_{tc} = $2\lambda E/\Delta E$) can be estimated by the energy spread of the beam. For example, in the present LaB_6 field emitter case, for E=3.6keV, ΔE was 0.9 eV, this gives L_{tc} =160 nm. The spatial coherence length, however, is not so easy to compute.

The idea of determining the spatial coherence length led the author to develop a point projection microscope (PPM). The first PPM was put forward in 1939 by Morton and Ramberg [210]. In contrast to a transmission electron microscope (TEM), PPM does not utilize electron lenses. An advantage of this is that chromatic and spherical aberrations of the objective lens are avoided. Only the intrinsic aberrations attributed to the curvature of the tip apex are present in the PPM (section 2.2.2).

6.3.1 Image formation in PPM

A PPM experiment, as shown in Figure 6.3, comprises a negative voltage biased sharp (1-100 nm) field emission tip, a sample consists of e-beam transparent regions with sharp edges and and an MCP/phosphor detector.

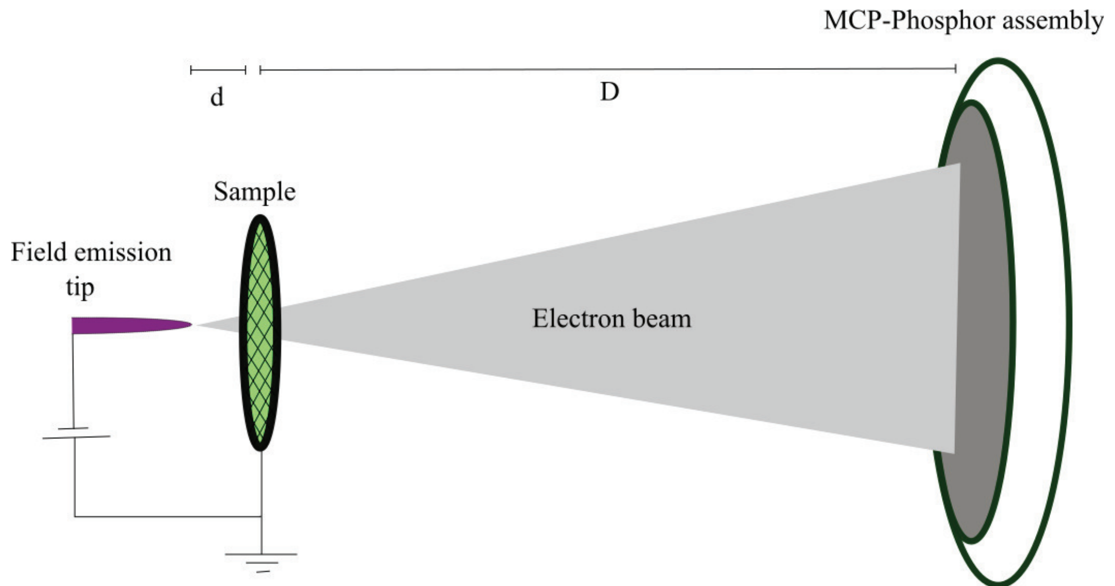

Figure 6.3 The experimental arrangement of the point projection microscope with field emission tip generating electrons that are weakly scattered by the transparent or semi-transparent sample placed at distance *d* from the tip before reaching to the MCP-Phosphor assembly at distance *D* from the sample

Figure 6.4 indicates that the Fresnel fringes formed in PPM correspond to defocused Fresnel fringes in TEM with a defocus value (Δf) equal to d. The magnification M, however, depends on the defocus, unlike TEM, and is given by $M = D/d$. Also, the fringe width, in TEM, is proportional to the square root of the objective defocus (Δf) whereas, in PPM, it is inversely proportional to the square root of defocus [194].

The resolution of PPM is limited by r_{eff}, the blurring effect due to stray electromagnetic fields and the mechanical vibrations [210][211]. As shown in Figure 6.1, r_{eff} is the virtual region inside the emitter from where the electrons seem to originate. It defines the coherence angle θ ($= \lambda/r_{eff}$) over which the phase correlation in an electron wave exist[44][45]. The highest order Fresnel fringe in PPM corresponds to θ, and the width of a full band of Fresnel fringes is approximately equal to the lateral coherence length L_{sc}.

6.3.2 The relation between coherence length and effective radius

According to the van Cittert-Zernike theorem, the light emitted from an incoherent source becomes coherent at large distances from the source[212]. Based on the direct analogy of electromagnetic and matter waves, this theorem based on light

optics is used by researchers to study the coherent properties of the particles[213]. According to the van Cittert-Zernike theorem, the coherence length L_{sc} at a distance z from the source of effective radius r_{eff} is:

$$r_{eff} = \frac{\lambda z}{\pi L_{sc}} \qquad 6.20$$

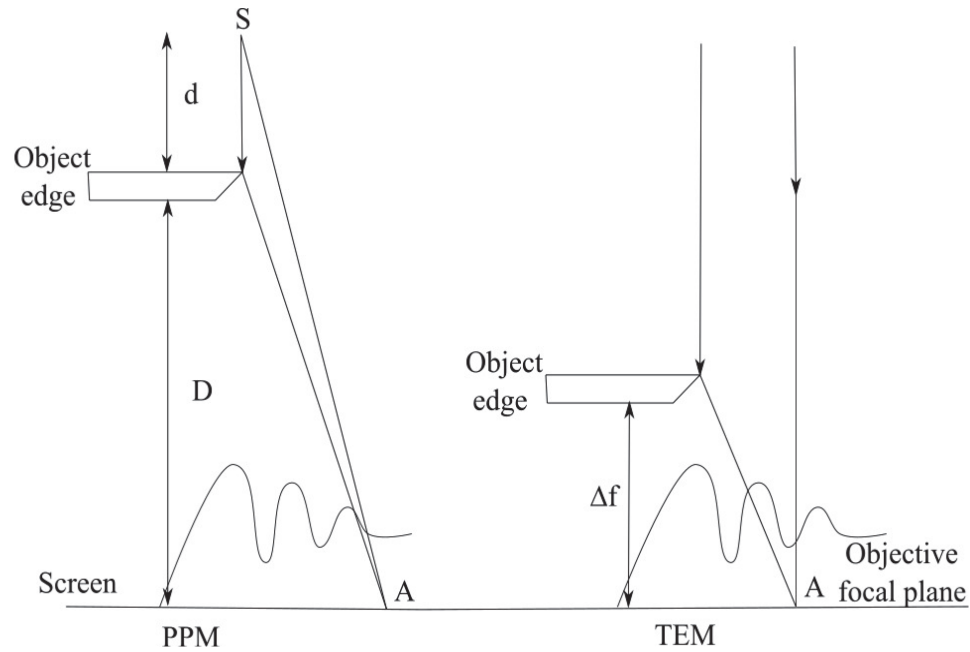

Figure 6.4 Ray diagram of Fresnel diffraction in (left) point projection microscope, where the Fresnel fringes are formed directly on screen and (right) transmission electron microscope, where the fringes are formed at unit magnification on the focal plane of the objective lens and magnified by the subsequent lenses before detector

6.3.3 In-house built point projection microscope and results

The point projection microscope developed in the present work is shown in Figure 6.5. In this PPM set-up, a 400 mesh quantifoil grid with hole radii of 1.2µm and spacing of 1.3µm, purchased from Tedpella Inc, was used as a sample. As shown schematically in Figure 6.5 (bottom), the emitter was mounted manually just in front of the sample (quantifoil) and positioned precisely at a distance of a few µm with a 3D-adjusting system purchased from SmarAct GmbH (Model: SLC 1730). The tip to sample distance d was initially monitored using an optical microscope that was mounted on the top flange (CF160) of the test chamber (Figure 3.5). The viewing range of the objective lens, however, was limited by the viewport (CF40) mounted on the flange. This led the author to use images of the objects of known size to calculate the distance d. The grid bar spacing of the quantifoil was used as a standard.

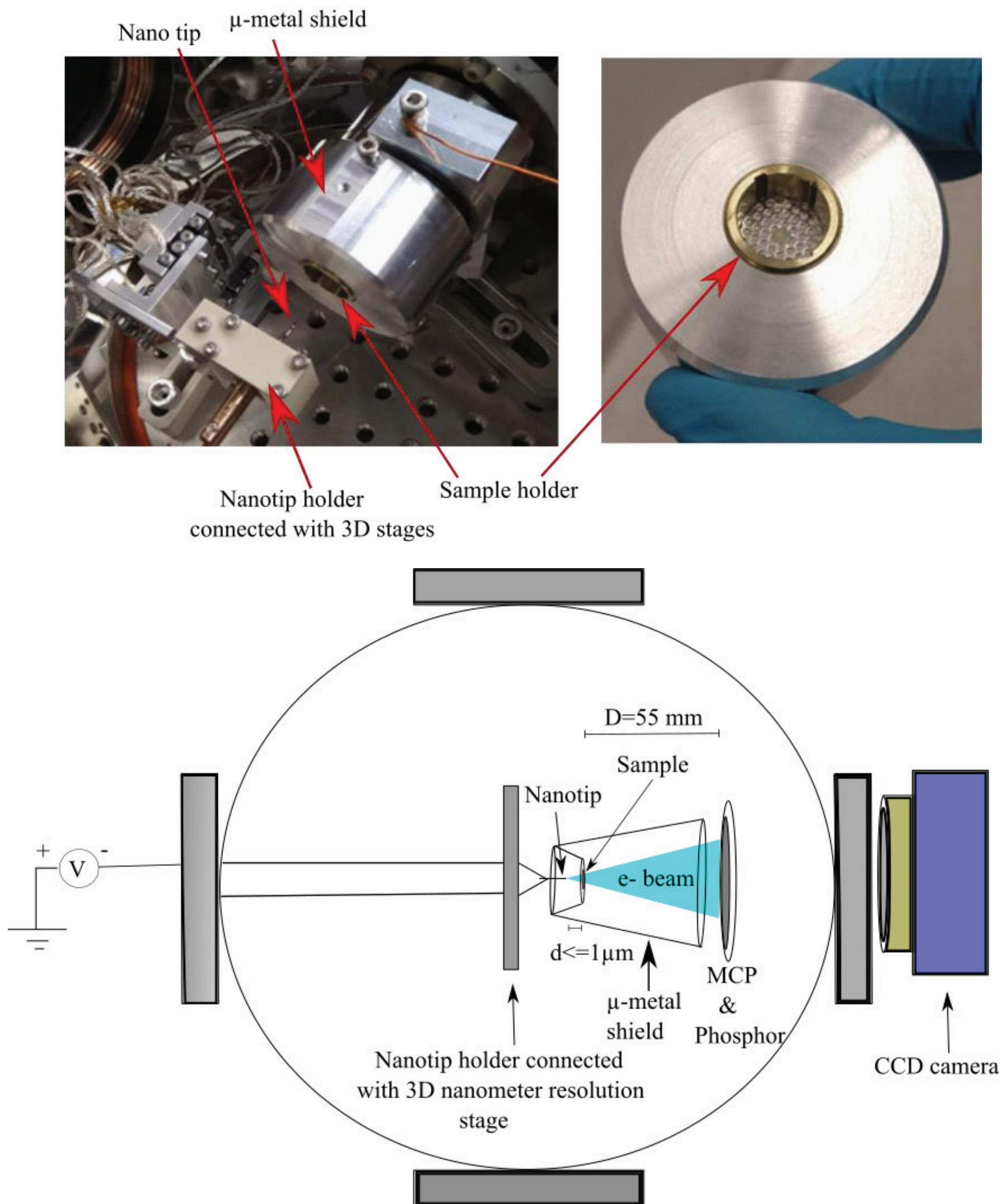

Figure 6.5 (top left) Photograph of in-house built point projection microscope having a nanotip and a µ-metal shield with sample loaded inside it, (top right) Photograph of sample holder showing quantifoil sitting in the middle of holder (bottom) Schematic of experimental setup shown with more detail

The grid was irradiated by electron waves propagating radially from the biased nanotip emitter which results in the magnified images of its features on the MCP screen. Image acquisition started once the copper bars were visible (Figure 6.6 a). The distance *d* was then reduced, initially in steps of a few tens of microns (Figure 6.6 a-c), and then few hundred nanometers (Figure 6.6 d-f), in order to bring the tip cautiously to the proximity of the grid. Simultaneously, the extraction voltage was reduced to ensure that the electric field around the tip, and hence the field emission current, remained under control.

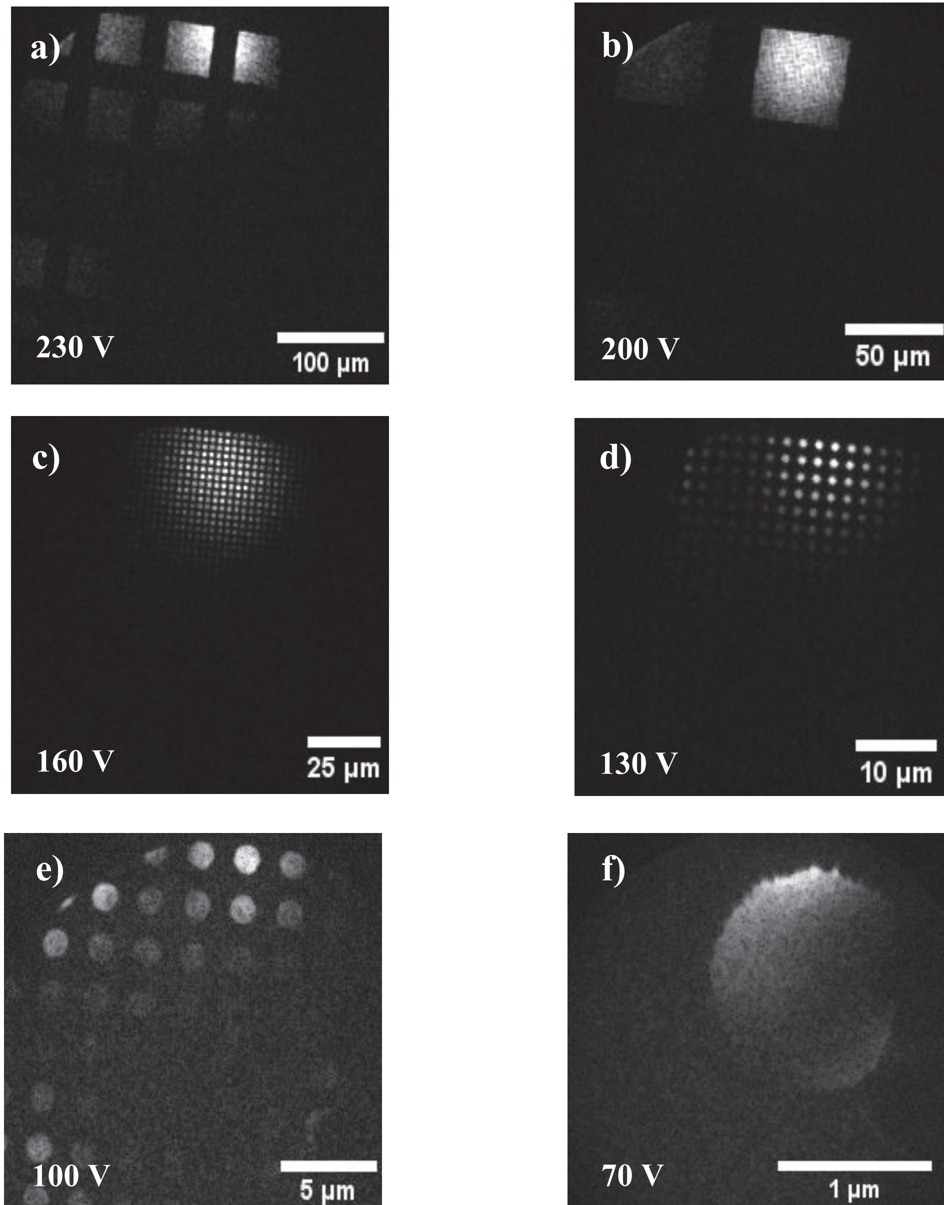

Figure 6.6 The magnified images of the features (in the ranges of several tens of microns to sub-micron) of quantifoil captured using PPM. (inset) showing the voltages at which images are captured.

The magnification M of the PPM can be written as[211]:

$$M = \frac{D}{d} \tag{6.21}$$

Equivalently, M can also be written as :

$$M = \frac{S_{screen}}{S_{actual}} \tag{6.22}$$

where S_{screen} is the size of the known feature on the screen and S_{actual} is the actual size of the same feature. The distance of the tip from the sample (*d*) can then be written in terms of known parameters as :

$$d = D\,\frac{S_{actual}}{S_{screen}} \tag{6.23}$$

In PPM, D (= 55mm) was kept constant throughout the acquisition of images. The ranges of the known feature sizes S_{actual}, as mentioned in the specification sheet provided by the supplier, were from 1 μm (each hole in carbon film) to 45 μm (grid squares). Using ImageJ software, the size of the feature on the screen S_{screen} was measured, and hence the distance of the tip from the sample was calculated using Equation 6.23. It was found to be 2 mm for Figure 6.6 a), 1.5 μm for Figure 6.6 f) and in between these two values for Figure 6.6 b) - e). The expected Fresnel fringes were not observed even at the microscopic proximity of the tip to the grid, as also noticed by other researchers [214][200][215]. The electron emitter was moved further towards the sample to improve the magnification of the PPM, even though no interference pattern was seen, corresponding images can be seen in Figure 6.7. Eventually, the tip collided with the specimen and was destroyed.

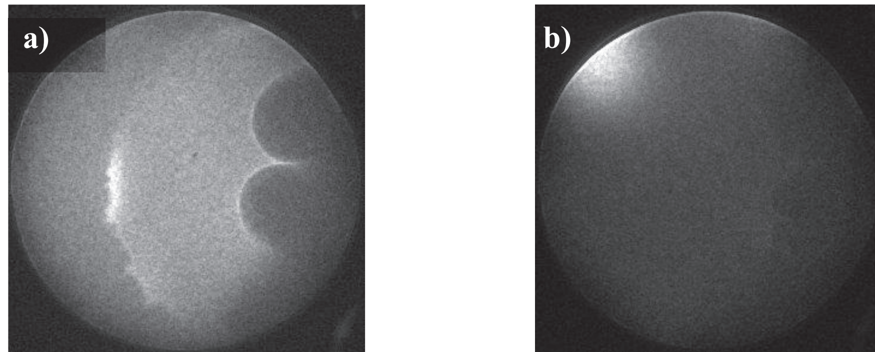

Figure 6.7 Images captured at a) 61V & b) 54V, showing no fringes on decreasing the distance between tip and sample. Half-circular features were observed that might be due to image artefacts or defects in quantifoil (No scale bar due to the absence of reference features in image).

The absence of Fresnel fringes can be explained by three important factors that affect the resolution and must be discussed.

6.3.3.1 Incoherent instabilities

The visibility of the Fresnel fringes may be limited by the incoherent instabilities, such as time-varying magnetic fields and mechanical vibration. The stray fields will introduce a time-dependent phase shift between the scattering beam and direct beam and hence degrade the resolution. To avoid this, a μ-metal shield was used between the sample and detector in the present setup.

The mechanical vibrations of the tip with respect to the sample or detector can also limit the resolution of PPM, for example, at a magnification of $10^4 – 10^6$, tip motion by 0.1 nm results in the displacement of 1µm-100µm in the fringes. This possibility can be ruled out in the present case as, during the experiment, all the mechanical vacuum pumps were switched off, and the entire setup was located on a vibration-isolated optical table.

6.3.3.2 Energy spread

The energy spread of the electron source could also affect the fringe visibility. Spence *et al*. showed that the highest resolvable fringe number n_{max} equals twice the ratio of the average energy to the energy spread of electrons [194]. For beam energy of 90 eV, an energy spread of 0.34 eV (Figure 5.20) gives n_{max} ~ 400-500. This means that chromatic broadening is not responsible for the lack of fringe visibility.

6.3.3.3 Detector resolution

The limited resolution of the imaging system (MCP/phosphor assembly and CCD camera) could also be the reason for fringe absence in the present PPM setup. The diameter of the channels of single MCP determines the highest resolution limit of the detection system. It is 12µm for the MCP used in the current PPM setup. The gain of 1000 was achieved with the acceleration voltage of 700V between the front and back electrodes of the MCP. The increase in electron density at the output of the MCP results in electrostatic repulsion. This broadens the electron cloud between the MCP and phosphor such that the resolution of the P43 phosphor screen for one electron impinges on the MCP front is in the order of 20-25µm[216][217][218]. The CCD camera installed to capture the visible light signal produced by the MCP screen is equipped with a KAI-04022 Kodak sensor of size 16.67mm × 16.05mm with pixel size 7.4µm × 7.4µm. According to the Nyquist criterion, the image space resolution of the CCD is 16µm. This corresponds to the object space resolution, and hence the imaging system resolution is 40µm for the desired field of view (40mm). If the separation distances among Fresnel fringes as well as fringe widths are comparable to or smaller than 40µm, then the fringes cannot be resolved. The maximum magnification achieved with the in-house built PPM was 3.4×10^4 at 70V (λ =1.5 Å) and d = 1.5µm. Upon using Equation 6.20 and multiplying with the magnification value, the spatial coherence length L_{sc} = 1.2 mm, which is equivalent to the width of the entire band of Fresnel fringes at the screen (see 6.3.1). Researchers [219] derived an expression for the position of fringes as:

$$X_n = \sqrt{2\lambda d(n + \frac{1}{8})} \qquad 6.24$$

This gives the positions of the first seven fringes at 22.4 nm, 31.2 nm, 37.7 nm 43 nm, 47.5 nm, 51.4 nm and 55 nm with 70V. With the magnification of 3.4×10^4, the corresponding positions at the MCP screen would be 0.77 mm, 1.08 mm, 1.30 mm, 1.49mm, 1.65 mm, 1.78 mm, and 1.91 mm respectively. The distance between the fringes

decreases for higher-orders. It can be seen that the gap between 6th and 7th fringes is 130μm which is much higher than the estimated resolution (40μm) of the imaging system.

The expression for the width of the fringes can be derived by differentiating Equation 6.24 with respect to *n* and taking δn =1 results into:

$$\delta X_n = \frac{\lambda d}{X_n} \qquad 6.25$$

This gives the width of the first seven fringes at the sample plane as follows: 10 nm, 7.2 nm, 5.9 nm, 5.23 nm, 4.73 nm, 4.38 nm, and 4.1 nm with 70V. The corresponding width at the MCP screen should be 346μm, 249μm, 204μm, 181μm, 163μm, 151μm, and 142 μm. However, the complete width of the Fresnel fringes band at the screen is only 1.2 mm as calculated in this section above. The calculated values of the fringe width and the distance between them imply that only 1 or 2 fringes will fall within this Fresnel fringe band. As the width of the fringe band is magnification dependent and hence can be increased by increasing the camera length *D* of the PPM setup. By doing this, several fringes will come under this Fresnel band, and therefore the contrast or visibility would be enhanced as done by previous researchers[103][194][214].

It implies that the lack of fringe visibility is attributed to the camera length *D* of the PPM setup but not the resolution of the imaging system. At the time of writing of this thesis, the setup was still under development.

7 Conclusion and Outlook

This Ph.D. work significantly contributes to the development and characterization of a novel electron source which constitutes a big step towards the dream of single-shot high-resolution phase-contrast imaging of biological samples. The most important achievement of the work presented here is the development of a robust LaB_6 based ultra-bright field emitter electron source with a highly reproducible fabrication method that works superbly even at low vacuum (> 10^{-9}mbar) conditions. This unusual combination is rare compared to other state-of-art cold field emitters (CFE), e.g. Single-atom electron sources, W nanotips and CNT emitters. Moreover, electron microscope industry is facing a challenge of using W CFE in general applications due to the inevitable current instabilities occuring even in ultra-high vacuum (<10^{-11} mbar) conditions. This work opens up the door to the usage of CFE electron source in custom-built electron diffraction and imaging machines and commercial electron microscopes (TEM/SEM/STEM) that do not have an expensive UHV system.

The capability of delivering more than 10^8 e^- per 10µs bunch and its vacuum compatibility can be used to image delicate biological samples in their native state before the beam damage begins. Also, the inherent advantage of the low work function (2.3-2.7 eV) of the LaB_6 compared to W guarantees a low energy spread, and hence the further enhancement of resolution in state-of-art electron microscopes equipped with advanced aberration correctors.

Here are some key achievements of this thesis:

- A reproducible LaB_6 field emitter fabrication method combining electrochemical etching and FIB milling was developed. This method not only significantly reduces processing times in the FIB but also gives more control over the morphology of the field emitter in the sub-100 nm regime, which was the challenge faced by previous researcher in producing a monolithic LaB_6 single tip structure.

- The surface study of the LaB_6 nanotip using EDS demonstrates that the La concentration was increased by the FIB milling process, which was supported by the analytical study using Monte-Carlo simulations. This study also demonstrated that Ga ion implantation occurred only 6-8 nm deep into the surface.

- A test setup (section 3.3), was designed and used for characterization of single field emitter tips, as was presented in section 5.1 and 5.3. This chamber was modified through the course of this Ph.D. work. An in-house developed energy analyser and aperture scan arrangement was integrated into this chamber to measure the energy distribution and angular current density of the electron

beam. The energy spread in the range of 0.3-0.6eV, and the maximum angular current density 8-10μA/Sr was measured, which were in close agreement to the state-of-art field emitter[103][171][220].

- A successful proof-of-principle experiment of microsecond electron pulse generation was performed using electronic pulsing of the extraction voltage. About 11μA of field emission current was extracted at 4.6kV. This is equivalent to 7×10^{8} e^{-} contained in a pulse of width 10μs.

- The energy spectra of the generated electron pulses illustrate an increase in the energy spread by 0.3-0.4 eV compared to the continuous e-beam. As mentioned in section 5.7.4, the increased contribution of the deep energy level electrons at high electric field can explained this. A linear shift of the peaks of energy spectrum towards low energy side was also observed with an increase in extraction voltage, unlike metallic field emitters. It might be due to the inherent non-metallic behaviour of LaB_6 (100) plane. Also, the surface modification due to the high extraction field or the Ga ion implantation might be the other possibilities. It was noticed, however, that no other emission spot emerged even after applying more than two times high electric potential and extracting more than 1000 times current than continuous e-beam, unlike usually observed in W emitters. This indicates the non-volatility and surface robustness of the LaB_6 surface. Nevertheless, the detailed study of the surface structure of LaB_6 after high field treatment must be done to understand the reason for such a non-metallic behaviour.
- In the present study, the effective source size r_{eff} ~ 1nm is estimated using an approximate method, which is in the range of values reported by the previous researchers for other field emitters with the same physical emission area. A more accurate way of estimating the effective source size is by measuring the coherence length. To do this, a point projection setup was developed. A proof of principle low energy (50-100eV) imaging of a holey carbon (quantifoil) grid was performed with this microscope as presented in section 6.3.3.

Outlook

- The yield efficiency of the developed fabrication method can be enhanced by implementing some modifications in both the steps, electrochemical etching and FIB milling. By integrating the feedback mechanism into the electrochemical etching circuit. The mechanism must break the circuit, and hence stop the process on a sudden rise in load resistance which depends on the radius of the tip apex. This modified arrangement will mitigate the manual efforts and human error in monitoring the process. The post-processing step in FIB miiling is used to decrease the Ga^{+} implantation inside the LaB_6. The usage of the noble gas ion

source (NGIS) integrated FIB machine will not only lessen the time of post-processing but also users do not have to worry about the change in electrical properties of the nanotip. With the advance in commercial noble ion source technology, it would be possible soon to fabricate the LaB_6 field emitter sources with a high yield.

- The effect of FIB milling on the LaB_6 work function was found to be in the range of the reported average work function (2.1-2.7 eV). Nevertheless, to get a clear picture of the LaB_6 nanotips' stoichiometry more sensitive and quantitative techniques like WDS and XPS are needed.
- Unwanted oscillations, known as 'ringing', in voltage pulses, were observed in the 2-3 µs regime, which limits the usage of pulse durations less than 5µs for reliable measurements. By tuning the RC network of the pulse generator circuit, µs or sub-µs pulses can be generated. The calculated temperature profile of the LaB_6 nanotip shows that mA range current can be comfortably extracted before its melting (Figure 5.25). Hence, there is a possibility that reducing the duty cycle will help in slowing down the two destructive processes, tip build-up and ion-sputtering, and therefore high peak current, if needed, can be achieved.
- Unfortunately, due to COVID-19, the development of PPM was halted at the final stage. This setup can be upgraded by increasing the camera length of the PPM, as suggested by the author in Chapter 6.

Contribution of the author

Scientific Publication:

- Fabrication and characterization of a focused ion beam milled lanthanum hexaboride based cold field electron emitter source
  G. Singh, R. Bücker, G. Kassier, M. Barthelmess, F. Zheng, V. Migunov, M. Kruth, R. E. Dunin-Borkowski, S. T. Purcell, R. J. D. Miller
  Applied Physics Letters 113 (9), 093101 (2018)

Conference Proceeding:

- Development of a LaB_6 based ultra-bright cold field emitter electron source
  G. Singh, R. Bücker, G. Kassier, R. J. D. Miller, S. T. Purcell
  NEW YORK, NY 10017 USA: IEEE; 2017

Own Poster Presentations:

- Gopal Singh, Robert Bücker, Günther Kassier, Miriam Barthelmess, R. J. Dwayne Miller, presented " *Development of a LaB_6 based high-current cold field emitter to generate microsecond pulses for capturing molecular dynamics*" at Microscience Microscopy Congress (MMC) 2019 Berlin, Germany
- Gopal Singh, Robert Bücker, Günther Kassier, Miriam Barthelmess, R. J. Dwayne Miller, presented " *Development of a LaB_6 based high-current cold field emitter to generate microsecond pulses for capturing molecular dynamics*" at Microscopy Conference (MC) 2019 Manchester, UK
- G. Singh, R. Bücker, G. Kassier, R. J. D. Miller, S. T. Purcell, presented "Development of a LaB_6 based ultra-bright cold field emitter electron source" International Vacuum Nanoelectronics Conference (IVNC) 2017 Regensburg, Germany

Appendices

1. MATLAB code for fitting the I-V curve using F-N model for field emission

```
function [fitresult, gof] = createFit(V, I)

%% Fit: 'untitled fit 1'.
[xData, yData] = prepareCurveData( V, I );
phi = 2.7              % Set work function of the emitter
% Set up fittype and options.
ft = fittype( 'a*x.^2.*exp(-b./x)', 'independent', 'x', 'dependent', 'y' );
opts = fitoptions( 'Method', 'NonlinearLeastSquares' );
opts.Display = 'Off';
opts.StartPoint = [0.138624442828679 0.149294005559057];

% Fit model to data.
[fitresult, gof] = fit( xData, yData, ft, opts );
Coeffs = coeffvalues(fitresult);
a = Coeffs(1)
b = Coeffs(2)
beta = ((6.44e+9)*(phi)^1.5)/b
radius = 1/(5*beta)
fitresult;
% Plot fit with data.
figure( 'Name', 'I-V curve' );
h = plot( fitresult,'b', xData, yData, 'co');
h(2).LineWidth = 3;
h(1).LineWidth = 2;

fitresult
legend( h, 'Experimental data', 'F-N fit', 'Location', 'NorthWest' );
% Label axes
xlabel('Voltage(V)','fontweight','bold','fontsize',16);
ylabel('Emission Current (nA)','fontweight','bold','fontsize',16);
grid off
```

2. MATLAB code for investigating the Joule heating and Nottingham effect

```
function pdemodel
[pde_fig,ax]=pdeinit;
pdetool('appl_cb',1);
set(ax,'DataAspectRatio',[1 1.0000000000000002 1]);
set(ax,'PlotBoxAspectRatio',[1.5000000000000004 1 10000]);
set(ax,'XLim',[-3.9999999999999998e-06 1.9999999999999995e-06]);
set(ax,'YLim',[0 3.9999999999999998e-06]);
set(ax,'XTick',[ a, b]); % a, b depends on the number of division user need
set(ax,'YTick',[ c, d]); % c, d depends on the number of division user need
setappdata(ax,'extraspacex','-2e-6:1e-8:2e-6');

% Geometry description:
pdepoly([ -3.9999999999999998e-06,...
 0,...
 0,...
 -3.9999999999999998e-06,...
],...
[ 1.9999999999999999e-06,...
 7.0000000000000005e-08,...
 -7.0000000000000005e-08,...
 -1.9999999999999999e-06,...
],...
 'P1');
pdeellip(0,0,7.0000000000000005e-08,7.0000000000000005e-08,...
0,'E1');
pderect([-3.9999999999999998e-06 7.0000000000000177e-08 0 -
1.9999999999999999e-06],'R1');
set(findobj(get(pde_fig,'Children'),'Tag','PDEEval'),'String','(P1+E1)-R1')

% Boundary conditions:
pdetool('changemode',0)
pdetool('removeb',[3 8 ]);
pdesetbd(6,...
'neu',...
1,...
'0',...
'(11981300*u.*cot(3.83e-4*u)+27.55-3.4e-9*u.^4).*y')
pdesetbd(5,...
'neu',...
1,...
'0',...
'0')
pdesetbd(4,...
'neu',...
1,...
'0',...
'0')
pdesetbd(3,...
'neu',...
1,...
'0',...
'0')
pdesetbd(2,...
'dir',...
1,...
'1',...
'300')
```

```
pdesetbd(1,...
'neu',...
1,...
'3.68e+6*y',...
'1.1e+9*y')

% Mesh generation:
setappdata(pde_fig,'Hgrad',1.3);
setappdata(pde_fig,'refinemethod','regular');
setappdata(pde_fig,'jiggle',char('on','mean',''));
setappdata(pde_fig,'MesherVersion','preR2013a');
pdetool('initmesh')
pdetool('refine')
pdetool('refine')

% PDE coefficients:
pdeseteq(2,...
'14.7*y',...
'0.0',...
'(1.40e+14*u - 4.10e+15-1.43*u.^4).*y',...
'(835*u + 6.06*u.^3).*y',...
'0:1e-4:1e-1',...
'300',...
'0.0',...
'[0 100]')
setappdata(pde_fig,'currparam',...
['14.7*y                                ';...
'0.0                                   ';...
'(1.40e+14*u - 4.10e+15-1.43*u.^4).*y';...
'(835*u + 6.06*u.^3).*y               '])

% Solve parameters:
setappdata(pde_fig,'solveparam',...
char('0','2400','10','pdeadworst',...
'0.5','longest','0','1E-4','','fixed','Inf'))

% Plotflags and user data strings:
setappdata(pde_fig,'plotflags',[1 1 1 1 1 1 1 1 0 0 0 1001 1 0 0 0 0 1]);
setappdata(pde_fig,'colstring','');
setappdata(pde_fig,'arrowstring','');
setappdata(pde_fig,'deformstring','');
setappdata(pde_fig,'heightstring','');

% Solve PDE:
pdetool('solve')
```

Data extraction:

```
%pde_fig=findobj(allchild(0),'flat','Tag','PDETool')
%u = get(findobj(pde_fig,'Tag','PDEPlotMenu'),'UserData');
int_time = 0.1;    %specify the time of calculation
F = pdeInterpolant(p,t,u);
pOut = [7e-8,  -3e-8, -5e-8, -8e-8,  0,   -1e-6, -5e-8, -8e-8, -2e-6;
% specify the points of emitter where temperture need to be evaluated
         0,       0,      0,      0,  7e-8,   0,  11e-8,  15e-8,   0];
uOut = evaluate(F,pOut);
time = 0:int_time/(length(uOut)-1):int_time;
figure
```

```
h1 = plot(time,uOut(1,:),'-om');


h1(1).LineWidth = 1;
hold on
h2 = plot(time,uOut(2,:),'-ob');
h2(1).LineWidth = 1;
h3 = plot(time,uOut(3,:),'-og');
h3(1).LineWidth = 1;
h4 = plot(time,uOut(4,:),'-or');
h4(1).LineWidth = 1;
h6 = plot(time,uOut(6,:),'-oc');
h6(1).LineWidth = 1;
%hold on
%h6 = plot(time,uOut(6,:),'-b');
%h6(1).LineWidth = 1;
%h7 = plot(time,uOut(7,:),'-g');
%h7(1).LineWidth = 1;
%h8 = plot(time,uOut(8,:),'-r');
%h8(1).LineWidth = 1;
h9 = plot(time,uOut(9,:),'-ks');
h9(1).LineWidth = 1;
hold off
title('Plot of emitter temperature profile with time at different location
on emitter','fontweight','bold','fontsize',16);
xlabel('time(s)','fontweight','bold','fontsize',16)
ylabel('temperature (kelvin)','fontweight','bold','fontsize',16)
legend({'apex','100nm along axis','120nm along axis','150nm along
axis','1micron along axis','base'},'Location','northwest')
xlim([0 int_time]);
ylim([299 max(max(uOut))+1]);

apex = F.evaluate(7e-8,0);      %apex temperature
apex_temp = apex(1,length(time))
```

References

[1] R. Kirby, *Engineering in History*. Courier Dover Publications, 1990.

[2] J. Stewart, *Intermediate Electromagnetic Theory*. World Scientific, 2001.

[3] J. J. Thomson, “Cathode rays,” *Philos. Mag.*, vol. 44, p. 293, 1897.

[4] R. Hooke, “Micrographia: Or Some Physiological Descriptions of Minute Bodies Made by Magnifying Glasses, with Observations and Inquiries Thereupon,” *Cour. Dover Publ.*, 1665.

[5] S. Leeuwenhoek, Antonie van; Hoole, “The Selected Works of Antony van Leeuwenhoek, Containing His Microscopical Discoveries in Many of the Works of Nature,” *G.Sidney*, 1800.

[6] A. Robinson, *The last man who knew everything : Thomas Young, the anonymous polymath who proved Newton wrong, explained how we see, cured the sick, and deciphered the Rosetta stone, among other feats of genius*. New York: New York: Pi Press, 2006.

[7] J. M. Schaeberle, “NEWTON’S CORPUSCULAR THEORY OF LIGHT,” *Science (80-.).*, vol. 53, no. 1382, p. 574, 1921.

[8] J. W. Strutt, “On pin-hole photography,” *Philos. Mag.*, vol. 31, no. 87, 1891.

[9] W. C. Röntgen, “Über eine neue Art von Strahlen,” *Der Würzburg. Phys. Gesellsch.*, vol. 137, pp. 132–141, 1895.

[10] M. von Laue, “Eine quantitative prüfung der theorie für die interferenz-erscheinungen bei Röntgenstrahlen.,” *Sitzungsberichte der Kgl. Bayer. Akad. Der Wiss.*, pp. 363–373, 1912.

[11] W. L. Bragg, “The diffraction of short electromagnetic waves by a crystal,” *Proc. Camb. Philol. Soc.*, vol. XVII, pp. 43–57, 1913.

[12] L. . Davisson, C.J.; Germer, “Reflection of Electrons by a Crystal of Nickel,” *Proc. Natl. Acad. Sci. U. S. A.*, vol. 14, no. 4, 1928.

[13] de Broglie, “RECHERCHES SUR LA THE´ORIE DES QUANTA,” *Ann. Phys.*, vol. 10, no. 3, 1925.

[14] A. V Crewe, J. Wall, and J. Langmore, “Visibility of Single Atoms,” *Science (80-.).*, vol. 168, no. 3937, pp. 1338 LP – 1340, Jun. 1970.

[15] J. Miao, P. Charalambous, J. Kirz, and D. Sayre, “Extending the methodology of X-ray crystallography to allow imaging of micrometre-sized non-crystalline specimens,” *Nature*, vol. 400, no. 6742, pp. 342–344, 1999.

[16] G. an. M. C. Giacovazzo, C; Monaco, H. L.; Artioli, G.; Viterbo,D.;Milaneso, M. ; Ferraris,G.; Gilli,G.; Gilli,P.; Zanotti, “Fundamentals of Crystallography, 3rd edition. C. Giacovazzo, H. L. Monaco, G. Artioli, D. Viterbo, M. Milaneso, G. Ferraris, G. Gilli, P. Gilli, G. Zanotti and M. Catti. Edited by C. Giacovazzo. IUCr Texts on Crystallography No. 15, IUCr/Oxford University,” *Acta Crystallogr. Sect. A*, vol. 67, no. 6, pp. 561–563,

Nov. 2011.

[17] R. J. D. Miller *et al.*, "'Making the molecular movie': first frames," *Acta Crystallogr. A.*, vol. 66, no. Pt 2, p. 137—156, Mar. 2010.

[18] R. Henderson, "The potential and limitations of neutrons, electrons and X-rays for atomic resolution microscopy of unstained biological molecules," *Q. Rev. Biophys.*, vol. 28, no. 2, pp. 171–193, May 1995.

[19] W. Kühlbrandt, "Cryo-EM enters a new era.," *Elife*, vol. 3, p. e03678, Aug. 2014.

[20] S. H. Scheres, "Beam-induced motion correction for sub-megadalton cryo-EM particles.," *Elife*, vol. 3, p. e03665, Aug. 2014.

[21] J. Frank, "Averaging of low exposure electron micrographs of non-periodic objects," *Ultramicroscopy*, vol. 1, no. 2, pp. 159–162, 1975.

[22] E. Knapek and J. Dubochet, "Beam damage to organic material is considerably reduced in cryo-electron microscopy," *J. Mol. Biol.*, vol. 141, no. 2, pp. 147–161, 1980.

[23] J. Dubochet *et al.*, "Cryo-electron microscopy of vitrified specimens," *Q. Rev. Biophys.*, vol. 21, no. 2, pp. 129–228, 1988.

[24] P. Ercius, O. Alaidi, M. J. Rames, and G. Ren, "Electron Tomography: A Three-Dimensional Analytic Tool for Hard and Soft Materials Research," *Adv. Mater.*, vol. 27, no. 38, pp. 5638–5663, Oct. 2015.

[25] H. N. Chapman *et al.*, "Femtosecond X-ray protein nanocrystallography," *Nature*, vol. 470, no. 7332, pp. 73–77, 2011.

[26] D. Shi, B. L. Nannenga, M. G. Iadanza, and T. Gonen, "Three-dimensional electron crystallography of protein microcrystals," *Elife*, vol. 2, Nov. 2013.

[27] C. G. Jones *et al.*, "The CryoEM Method MicroED as a Powerful Tool for Small Molecule Structure Determination.," *ACS Cent. Sci.*, vol. 4, no. 11, pp. 1587–1592, Nov. 2018.

[28] K. Yonekura, T. Ishikawa, and S. Maki-Yonekura, "A new cryo-EM system for electron 3D crystallography by eEFD.," *J. Struct. Biol.*, vol. 206, no. 2, pp. 243–253, May 2019.

[29] R. Bücker *et al.*, "Serial protein crystallography in an electron microscope," *Nat. Commun.*, vol. 11, no. 1, p. 996, 2020.

[30] M. J. Williamson, R. M. Tromp, P. M. Vereecken, R. Hull, and F. M. Ross, "Dynamic microscopy of nanoscale cluster growth at the solid–liquid interface," *Nat. Mater.*, vol. 2, no. 8, pp. 532–536, 2003.

[31] N. de Jonge, D. B. Peckys, G. J. Kremers, and D. W. Piston, "Electron microscopy of whole cells in liquid with nanometer resolution," *Proc. Natl. Acad. Sci.*, vol. 106, no. 7, pp. 2159 LP – 2164, Feb. 2009.

[32] S. Keskin *et al.*, "Visualization of Multimerization and Self-Assembly of DNA-Functionalized Gold Nanoparticles Using In-Liquid Transmission Electron Microscopy," *J. Phys. Chem. Lett.*, vol. 6, no. 22, pp. 4487–4492, Nov. 2015.

[33] C. Mueller, M. Harb, J. R. Dwyer, and R. J. D. Miller, “Nanofluidic Cells with Controlled Pathlength and Liquid Flow for Rapid, High-Resolution In Situ Imaging with Electrons,” *J. Phys. Chem. Lett.*, vol. 4, no. 14, pp. 2339–2347, Jul. 2013.

[34] S. Besztejan *et al.*, “Visualization of Cellular Components in a Mammalian Cell with Liquid-Cell Transmission Electron Microscopy,” *Microsc. Microanal.*, vol. 23, no. 1, pp. 46–55, 2017.

[35] R. F. Egerton, P. Li, and M. Malac, “Radiation damage in the TEM and SEM.,” *Micron*, vol. 35, no. 6, pp. 399–409, 2004.

[36] L. A. Baker and J. L. Rubinstein, “Radiation damage in electron cryomicroscopy.,” *Methods Enzymol.*, vol. 481, pp. 371–388, 2010.

[37] R. M. Glaeser, “Retrospective: radiation damage and its associated ‘information limitations’.,” *J. Struct. Biol.*, vol. 163, no. 3, pp. 271–276, Sep. 2008.

[38] M. Karuppasamy, F. Karimi Nejadasl, M. Vulovic, A. J. Koster, and R. B. G. Ravelli, “Radiation damage in single-particle cryo-electron microscopy: effects of dose and dose rate.,” *J. Synchrotron Radiat.*, vol. 18, no. Pt 3, pp. 398–412, May 2011.

[39] H. N. Chapman, C. Caleman, and N. Timneanu, “Diffraction before destruction.,” *Philos. Trans. R. Soc. London. Ser. B, Biol. Sci.*, vol. 369, no. 1647, p. 20130313, Jul. 2014.

[40] E. F. Garman, “Radiation damage in macromolecular crystallography: what is it and why should we care?,” *Acta Crystallogr. Sect. D*, vol. 66, no. 4, pp. 339–351, Apr. 2010.

[41] R. F. Egerton, “Outrun radiation damage with electrons?,” *Adv. Struct. Chem. Imaging*, vol. 1, no. 1, pp. 1–11, 2015.

[42] R. J. D. Miller, “Mapping Atomic Motions with Ultrabright Electrons: The Chemists’ Gedanken Experiment Enters the Lab Frame,” *Annu. Rev. Phys. Chem.*, vol. 65, no. 1, pp. 583–604, Apr. 2014.

[43] R. J. D. Miller, “Femtosecond crystallography with ultrabright electrons and x-rays: capturing chemistry in action.,” *Science*, vol. 343, no. 6175, pp. 1108–1116, Mar. 2014.

[44] A. H. Zewail, “4D Ultrafast Electron Diffraction, Crystallography, and Microscopy,” *Annu. Rev. Phys. Chem.*, vol. 57, no. 1, pp. 65–103, 2006.

[45] B. W. Reed *et al.*, “The Evolution of Ultrafast Electron Microscope Instrumentation,” *Microsc. Microanal.*, vol. 15, no. 04, pp. 272–281, Aug. 2009.

[46] R. H. Fowler and L. Nordheim, “Electron Emission in Intense Electric Fields,” *Proc. R. Soc. A Math. Phys. Eng. Sci.*, vol. 119, no. 781, pp. 173–181, 1928.

[47] N. de Jonge and J.-M. Bonard, “Carbon nanotube electron sources and applications.,” *Philos. Trans. A. Math. Phys. Eng. Sci.*, vol. 362, no. 1823, pp. 2239–66, Oct. 2004.

[48] E. E. Windsor and C. E. E. Eng, “Construction and performance of practical field emitters from lanthanum hexaboride.”

[49] H. Zhang *et al.*, “An ultrabright and monochromatic electron point source made of a

LaB 6 nanowire," *Nat. Nanotechnol.*, 2016.

[50] O. W. Richardson, "The Emission of Electricity from Hot Bodies," *Longmans, London*, 1916.

[51] A. Einstein, "No Title," *Ann. Phys.*, vol. 17, p. 132, 1905.

[52] C. B. Williams, B. David; Carter, *Transmission Electron Microscopy*, vol. 43, no. 2. 1994.

[53] "On the theory of quantum mechanics," *Proc. R. Soc. London. Ser. A, Contain. Pap. a Math. Phys. Character*, vol. 112, no. 762, pp. 661–677, 1926.

[54] A. Zannoni, "On the Quantization of the Monoatomic Ideal Gas," pp. 1–6, 1999.

[55] H. Hertz, "Ueber einen Einfluss des ultravioletten Lichtes auf die electrische Entladung," *Ann. Phys.*, vol. 267, no. 8, pp. 983–1000, 1887.

[56] P. Lenard, "Ueber die lichtelektrische Wirkung," *Ann. Phys.*, vol. 313, no. 5, pp. 149–198, 1902.

[57] N. D. Browning *et al.*, "Recent developments in dynamic transmission electron microscopy," *Current Opinion in Solid State and Materials Science*. 2012.

[58] P. Hommelhoff, Y. Sortais, A. Aghajani-Talesh, and M. A. Kasevich, "Field Emission Tip as a Nanometer Source of Free Electron Femtosecond Pulses," *Phys. Rev. Lett.*, vol. 96, no. 7, p. 77401, Feb. 2006.

[59] C. Ropers, T. Elsaesser, G. Cerullo, M. Zavelani-Rossi, and C. Lienau, "Ultrafast optical excitations of metallic nanostructures: from light confinement to a novel electron source," *New J. Phys.*, vol. 9, no. 10, p. 397, 2007.

[60] A. H. Zewail, "Four-dimensional electron microscopy.," *Science*, vol. 328, no. 5975, pp. 187–193, Apr. 2010.

[61] M. Gulde *et al.*, "Ultrafast low-energy electron diffraction in transmission resolves polymer/ graphene superstructure dynamics," *Science (80-.).*, vol. 345, no. 6193, 2013.

[62] B. Cook, *Brightness limitations in sources for static and ultra-fast high resolution electron microscopy*. 2013.

[63] M. Krüger, M. Schenk, and P. Hommelhoff, "Attosecond control of electrons emitted from a nanoscale metal tip," *Nature*, vol. 475, no. 7354, pp. 78–81, 2011.

[64] a. H. V. van Veen, C. W. Hagen, J. E. Barth, and P. Kruit, "Reduced brightness of the ZrO/W Schottky electron emitter," *J. Vac. Sci. Technol. B Microelectron. Nanom. Struct.*, vol. 19, no. 6, p. 2038, 2001.

[65] G. Sciaini and R. J. D. Miller, "Femtosecond electron diffraction : heralding the era of atomically resolved," *Reports Prog. Phys.*, 2011.

[66] C. B. Carter and D. B. Williams, "Transmission electron microscopy: Diffraction, imaging, and spectrometry," *Transm. Electron Microsc. Diffraction, Imaging, Spectrom.*, pp. 1–518, 2016.

[67] G. Fursey, *Field emission in Vacuum microelectronics*. New York: Kluwer Academic/ Plenum Publishers, 2005.

[68] R. Stratton, “Theory of field emission from semiconductors,” *Phys. Rev.*, vol. 125, no. 1, pp. 67–82, 1962.

[69] R. . Murphy, E.L; Good, “Thermionic emission, field emission and transition region,” *Phys. Rev.*, vol. 102, no. 6, pp. 1464–1473, 1956.

[70] J. M. Burgess, R.E; Kroemer, H; Housten, “Corrected values of Fowler-Nordheim field emission function v(y) and S(y),” *Phys. Rev.*, vol. 90, no. 515, 1953.

[71] N. Camus *et al.*, “Experimental Evidence for Quantum Tunneling Time,” *Phys. Rev. Lett.*, vol. 119, no. 2, pp. 1–6, 2017.

[72] A. Casandruc, G. Kassier, H. Zia, R. Bücker, and R. J. D. Miller, “Fiber tip-based electron source,” *J. Vac. Sci. Technol. B, Nanotechnol. Microelectron. Mater. Process. Meas. Phenom.*, vol. 33, no. 3, p. 03C101, 2015.

[73] R. Ganter *et al.*, “Nanosecond field emitted and photo-field emitted current pulses from ZrC tips,” *Nucl. Instruments Methods Phys. Res. Sect. A Accel. Spectrometers, Detect. Assoc. Equip.*, vol. 565, no. 2, pp. 423–429, 2006.

[74] R. Smoluchowski, “Anisotropy of the electronic work function of metals,” *Phys. Rev.*, vol. 60, no. 9, pp. 661–674, 1941.

[75] R. Gomer, *Gomer.pdf*. Harvard University Press, 1961.

[76] K. Binh, Vu Thien; Garcia, N; Drensfeld, *Nanosource and manipulation of atoms under high fields and temperature*, 1st ed. Lyon, France: Nato series, 1993.

[77] I. L. Sokolovskia, “No Title,” *J. Tech. Phys.*, vol. 26, no. 1177, 1956.

[78] V. T. Binh, “In situ fabrication and regeneration of microtips for scanning tunnelling microscopy,” *J. Microsc.*, vol. 152, no. 2, pp. 355–361, Nov. 1988.

[79] L. Dyke, W. P. ; Dolan, W. W. and Marton, *Advances in Electronics and Electron Physics*, 8th ed. New York: Academic Press, 1956.

[80] T. Hawkes, Peter. W.;Kazan, Benzamin; Mulvey, *Advances in Imaging and Electron physics*. Academic Press, 2002.

[81] M. Bronsgeest, *Physics of Electron sources*, vol. 28, no. 1–4. 2013.

[82] D. H. Dowell, “LECTURE 2: ELECTRON EMISSION AND CATHODE EMITTANCE.”

[83] W. Osten, “Statistical optics,” *Opt. Lasers Eng.*, vol. 35, no. 6, pp. 403–404, 2001.

[84] B. Cho, T. Ichimura, R. Shimizu, and C. Oshima, “Quantitative evaluation of spatial coherence of the electron beam from low temperature field emitters,” *Phys. Rev. Lett.*, vol. 92, no. 24, pp. 1–4, 2004.

[85] C. C. Chang, H. S. Kuo, I. S. Hwang, and T. T. Tsong, “A fully coherent electron beam from a noble-metal covered W(111) single-atom emitter,” *Nanotechnology*, vol. 20, no.

11, 2009.

[86] B. Cook, M. Bronsgeest, K. Hagen, and P. Kruit, “Improving the energy spread and brightness of thermal-field (Schottky) emitters with PHAST--PHoto Assisted Schottky Tip.,” *Ultramicroscopy*, vol. 109, no. 5, pp. 403–412, Apr. 2009.

[87] H. Shimoyama and S. Maruse, “Theoretical considerations on electron optical brightness for thermionic, field and T-F emissions,” *Ultramicroscopy*, vol. 15, no. 3, pp. 239–254, 1984.

[88] S. T. Purcell, P. Vincent, C. Journet, and V. T. Binh, “Hot Nanotubes: Stable Heating of Individual Multiwall Carbon Nanotubes to 2000 K Induced by the Field-Emission Current,” *Phys. Rev. Lett.*, vol. 88, no. 10, p. 4, 2002.

[89] J. W. Gadzuk and E. W. Plummer, “Field emission energy distribution (FEED),” *Rev. Mod. Phys.*, 1973.

[90] R. D. Young, “Theoretical total-energy distribution of field-emitted electrons,” *Phys. Rev.*, vol. 113, no. 1, pp. 110–114, 1959.

[91] W. Knauer, “Boersch effect in electron-optical instruments,” *J. Vac. Sci. Technol.*, vol. 16, no. 6, pp. 1676–1679, 2002.

[92] J. Teichert, R. Xiang, and J. W. J. Verschuur, “Report on photocathodes,” *Care/Jraphin*, no. July, 2004.

[93] G. Wang, P. Yang, N. A. Moody, and E. R. Batista, “Overcoming the quantum efficiency-lifetime tradeoff of photocathodes by coating with atomically thin two-dimensional nanomaterials,” *npj 2D Mater. Appl.*, vol. 2, no. 1, pp. 1–9, 2018.

[94] A. . Willardson, R.K; Beer, Ed., *Semiconductor and Semimetals*, Volume 9 M. New York and London: Academic Press, 1972.

[95] L. J. Devlin, L. B. Jones, T. C. Q. Noakes, C. P. Welsch, and B. L. Militsyn, “Measurement of the longitudinal energy distribution of electrons in low energy beams using electrostatic elements,” *Rev. Sci. Instrum.*, vol. 89, no. 8, pp. 1–7, 2018.

[96] L. Zhang, J. P. Hoogenboom, B. Cook, and P. Kruit, “Photoemission sources and beam blankers for ultrafast electron microscopy,” *Struct. Dyn.*, vol. 6, no. 5, 2019.

[97] A. V. Crewe, J. Wall, and L. M. Welter, “A high-resolution scanning transmission electron microscope,” *J. Appl. Phys.*, vol. 39, no. 13, pp. 5861–5868, 1968.

[98] K. L. Jensen, M. A. Kodis, R. A. Murphy, and E. G. Zaidman, “Space charge effects on the current-voltage characteristics of gated field emitter arrays Interplay of current crowding and current self-quenching effects in planar cold cathodes Space-charge effects and current self-quenching in a metal/CdS/LaS cold cathode Space charge effects on the current-voltage characteristics of gated field emitter arrays,” *J. Appl. Phys. J. Vac. Sci. Technol. B J. Vac. Sci. Technol. B J. Vac. Sci. Technol. B J. Appl. Phys. AIP Conf. Proc*, vol. 821, no. 10, pp. 2–5, 1997.

[99] W. A. Mackie, T.-. Xie, J. E. Blackwood, and P. R. Davis, “Field emission from HfC films on Mo field emitter arrays and from HfC arrays,” in *IEEE Conference Record - Abstracts. 1997 IEEE International Conference on Plasma Science*, 1997, p. 284.

[100] W. B. Choi, J. J. Cuomo, V. V. Zhirnov, A. F. Myers, and J. J. Hren, “Field emission from silicon and molybdenum tips coated with diamond powder by dielectrophoresis,” *Appl. Phys. Lett.*, vol. 720, no. November 1995, p. 720, 1995.

[101] S. Iijima, “Helical microtubules of graphitic carbon,” *Nature*, vol. 354, pp. 56–58, 1991.

[102] N. D. E. JONGE, Y. LAMY, K. SCHOOTS, and T. H. OOSTERKAMP, “High brightness electron beam from a multi-walled carbon nanotube,” *Nature*, vol. 420, no. 1998, pp. 393–395, 2002.

[103] N. De Jonge, M. Allioux, J. T. Oostveen, K. B. K. Teo, and W. I. Milne, “Optical performance of carbon-nanotube electron sources,” *Phys. Rev. Lett.*, vol. 94, no. 18, pp. 1–4, 2005.

[104] K. J. Kim, W. R. Yu, J. H. Youk, and J. Lee, “Factors governing the growth mode of carbon nanotubes on carbon-based substrates,” *Phys. Chem. Chem. Phys.*, vol. 14, no. 40, pp. 14041–14048, 2012.

[105] M. S. Bronsgeest, J. E. Barth, L. W. Swanson, and P. Kruit, “Probe current, probe size, and the practical brightness for probe forming systems,” *J. Vac. Sci. Technol. B Microelectron. Nanom. Struct.*, vol. 26, no. 3, pp. 949–955, 2008.

[106] P. Kruit, M. Bezuijen, and J. E. Barth, “Source brightness and useful beam current of carbon nanotubes and other very small emitters,” *J. Appl. Phys.*, vol. 99, no. 2, p. 024315, 2006.

[107] R. Rao *et al.*, “Carbon Nanotubes and Related Nanomaterials: Critical Advances and Challenges for Synthesis toward Mainstream Commercial Applications,” *ACS Nano*, vol. 12, no. 12, pp. 11756–11784, Dec. 2018.

[108] W. P. Dyke, J. K. Trolan, E. E. Martin, and J. P. Barbour, “The field emission initiated vacuum arc. I. Experiments on arc initiation,” *Phys. Rev.*, 1953.

[109] A. Rose, “Comparative Noise Properties of Vision, Television, and Photographic Film BT - Vision: Human and Electronic,” A. Rose, Ed. Boston, MA: Springer US, 1973, pp. 95–110.

[110] F. M. Ross, Ed., *Liquid Cell Electron Microscopy*. Cambridge: Cambridge University Press, 2016.

[111] S. A. Campbell, *The Science and Engineering of Microelectronic Fabrication*, Second. Oxford university press, 2013.

[112] B. J. Siwick, J. R. Dwyer, R. E. Jordan, and R. J. D. Miller, “An Atomic-Level View of Melting Using Femtosecond Electron Diffraction,” *Science (80-.).*, vol. 302, no. 5649, pp. 1382–1385, Jun. 2003.

[113] R. D. Young and E. W. Muller, “Experimental measurement of the total energy distribution of field emitted electrons,” *Phys. Rev.*, vol. 113, no. 1, 1959.

[114] J. A. Simpson, “Design of Retarding field energy Analyzers,” *Rev. Sci. Instrum.*, vol. 32, pp. 1283–1293, 1961.

[115] A. A. Holscher, “A FIELD EMI~ION RETARDING POTENTIAL METHOD FOR

MEASURING WORK FUNCTIONS," *Surf. Sci.*, vol. 4, pp. 89–102, 1966.

[116] E. E. Martin, J. K. Trolan, W. P. Dyke, and E. Stability, "Stable, High Density Field Emission Cold Cathode," vol. 782, no. 1960, 2008.

[117] W. P. Dolan, W. W & Dyke, "Temperature-and-Field Emission of Electrons from Metals," *Phys*, vol. 95, no. 2, pp. 327–332, 1952.

[118] H. R. Schmidt, F. F.; Ogden, "The engineering properties of tungsten and tungsten alloys," *DMIC Rep. 191*, 1963.

[119] R. J. Colton, "On the electrochemical etching of tips for scanning tunneling microscopy On the electrochemical etching of tips for scanning tunneling microscopy," *J. Vac. Sci. Technol. A*, vol. 3570, no. 8, 1990.

[120] A. You, M. A. Y. Be, and I. In, "Electrochemical preparation of tungsten tips for a scanning tunneling microscope," *Rev. Sci. Instrum.*, vol. 1917, no. 67, 1996.

[121] O. L. Guise, J. W. Ahner, M. Jung, P. C. Goughnour, and J. T. Yates, "Reproducible Electrochemical Etching of Tungsten Probe Tips," *Nano Lett.*, vol. 2, pp. 191–193, 2002.

[122] M. Kulakov, I. Luzinov, K. G. Kornev, and S. Carolina, "Capillary and Surface Effects in the Formation of Nanosharp Tungsten Tips by Electropolishing," *ACS Langmuir*, vol. 25, no. 8, pp. 4462–4468, 2009.

[123] A. You, M. A. Y. Be, and I. In, "Two-step controllable electrochemical etching of tungsten scanning probe microscopy tips," *Rev. Sci. Instrum.*, vol. 063708, no. 83, 2012.

[124] A. N. Chaika *et al.*, "Fabrication of [001]-oriented tungsten tips for high resolution scanning tunneling microscopy," *Sci. Rep.*, pp. 1–6, 2014.

[125] S. Narasiwodeyar, M. Dwyer, M. Liu, W. K. Park, and L. H. Greene, "Two-step fabrication technique of gold tips for use in point-contact spectroscopy," *Rev. Sci. Instrum.*, vol. 86, no. 3, pp. 1–16, 2015.

[126] A. You, M. A. Y. Be, and I. In, "Mesoscale scanning probe tips with subnanometer rms roughness," *Rev. Sci. Instrum.*, vol. 073707, no. June 2007, 2012.

[127] B.-F. Ju, Y.-L. Chen, and Y. Ge, "The art of electrochemical etching for preparing tungsten probes with controllable tip profile and characteristic parameters," *Rev. Sci. Instrum.*, vol. 82, no. 1, p. 13707, Jan. 2011.

[128] J. P. Ibe et.al, "On the electrochemical etching of tips for scanning tunneling microscopy," *J. Vac. Sci. Technol. A*, vol. 8, no. 3570, 1990.

[129] H. Ahmed and A. N. Broers, "Lanthanum hexaboride electron emitter," *J. Appl. Phys.*, vol. 43, no. 5, pp. 2185–2192, 1972.

[130] L. W. Swanson, M. A. Gesley, and P. R. Davis, "Crystallographic dependence of the work function and volatility of LaB6," *Surf. Sci.*, vol. 107, no. 1, pp. 263–289, 1981.

[131] H. Zhang, Q. Zhang, J. Tang, and L. C. Qin, "Single-crystalline LaB6 nanowires," *J. Am. Chem. Soc.*, 2005.

[132] M. Futamoto, S. Hosoki, H. Okano, and U. Kawabe, "Field-emission and field-ion microscopy of lanthanum hexaboride," *J. Appl. Phys.*, vol. 48, no. 8, pp. 3541–3546, 1977.

[133] X. Wang, Y. Jiang, Z. Lin, K. Qi, and B. Wang, "Field emission characteristics of single crystal LaB 6 field emitters fabricated by electrochemical etching method," *J. Phys. D Appl. Phys. J. Phys. D Appl. Phys*, vol. 42, no. 42, pp. 55409–4, 2009.

[134] M. A. Uijttewaal, G. A. de Wijs, and R. A. de Groot, "Ab Initio and Work Function and Surface Energy Anisotropy of LaB_6," *J. Phys. Chem. B*, 2006.

[135] X. Wang, Y. Jiang, Z. Lin, K. Qi, and B. Wang, "Field emission characteristics of single crystal LaB 6 field emitters fabricated by electrochemical etching method," *J. Phys. D Appl. Phys. J. Phys. D Appl. Phys*, vol. 42, no. 42, pp. 55409–4, 2009.

[136] U. Futamoto,M ; Hosoki,S; Okano,H and Kawabe, "Field -emission and field-ion microscopy of lanthanum hexaboride," *J. Appl. Phys.*, vol. 48, no. 3541, 1977.

[137] Allen J Bard; Roger Parsons; Joseph Jordan, *Standard potentials in aqueous solution*, 1st ed. New York : M. Dekker, 1985, 1985.

[138] J. Atkins, Peter; Loretta, *Chemical Principles: The Quest for Insight*, Third. New York: W. H. Freeman, 2005.

[139] M. K. Miller, K. F. Russell, K. Thompson, R. Alvis, and D. J. Larson, "Review of Atom Probe FIB-Based Specimen Preparation Methods," *Microsc. Microanal.*, vol. 13, no. 06, pp. 428–436, Dec. 2007.

[140] N. V. (Nikolay V. . Egorov and E. Sheshin, *Field emission electronics*. 2017.

[141] T. Gnanavel, Y. Peng, X. Xu, B. J. Inkson, M. R. J. Gibbs, and G. Möbus, "Ni and W nanotips: Fabrication and characterisation," *J. Phys. Conf. Ser.*, vol. 126, pp. 8–12, 2008.

[142] L. W. Swanson and T. Dickinson, "Single-crystal work-function and evaporation measurements of LaB_6," *Appl. Phys. Lett.*, vol. 28, no. 10, pp. 578–580, May 1976.

[143] D. J. Larson *et al.*, "Field-ion specimen preparation using focused ion-beam milling," *Ultramicroscopy*, vol. 79, no. 1–4, pp. 287–293, 1999.

[144] B. W. Kempshall, L. A. Giannuzzi, B. I. Prenitzer, F. A. Stevie, and S. X. Da, "Comparative evaluation of protective coatings and focused ion beam chemical vapor deposition processes," *J. Vac. Sci. Technol. B Microelectron. Nanom. Struct.*, vol. 20, no. 1, pp. 286–290, 2002.

[145] J. F. Ziegler, J. P. Biersack, and U. Littmark, *The stopping and range of ions in matter*. Springer, 1985.

[146] E. B. David, Ed., *Energy Research Abstracts*. Technical Information center, U.S. Department of Energy, 1979.

[147] V. T. Binh, Ed., *Surface mobilities on solid materials*. New York and London: Plenum press, 1981.

[148] I. Brodie and C. A. Spindt, "Vacuum Microelectronics," *Adv. Electron. Electron Phys.*,

vol. 83, pp. 1–106, Jan. 1992.

[149] K. Y. Cheong, *Two-Dimensional Nanostructures for Energy-Related Applications*, 1st ed. CRC press, 2016.

[150] G. Singh *et al.*, “Fabrication and characterization of a focused ion beam milled lanthanum hexaboride based cold field electron emitter source,” vol. 093101, 2018.

[151] H. Zhang *et al.*, “Nanostructured LaB6 field emitter with lowest apical work function,” *Nano Lett.*, vol. 10, no. 9, pp. 3539–3544, 2010.

[152] H. Nagata, K. Harada, R. Shimizu, H. Nagata, K. Harada, and R. Shimizu, “Thermal field emission observation of single-crystal LaB6.pdf,” vol. 3614, no. 1990, 2008.

[153] C. KLEINT, “Surface Diffusion Model of Adsorption-Induced Field Emission Flicker Noise,” *Surf. Sci.*, vol. 25, pp. 394–410, 1971.

[154] F. M. Bettler,Philip C; Charbonnier, “Activation Energy for the Surface Migration of Tungsten in the presence of a High-Electric Field,” *Phys. Rev.*, vol. 119, no. 1, pp. 85–89, 1960.

[155] K. Christmann, “Interaction of hydrogen with solid surfaces,” *Surf. Sci. Rep.*, vol. 9, no. 1–3, pp. 1–163, 1988.

[156] J. H. Kaspersma, “PHYSICAL ADSORPTION ON METALS,” *Thesis*, 1972.

[157] J. K. ROBERTS, “Adsorption of Nitrogen on Tungsten,” *Nature*, vol. 137, no. 3468, pp. 659–660, 1936.

[158] V. N. Tondare, N. J. van Druten, C. W. Hagen, and P. Kruit, “Stable field emission from W tips in poor vacuum conditions,” *J. Vac. Sci. Technol. B Microelectron. Nanom. Struct.*, vol. 21, no. 4, p. 1602, 2003.

[159] L. W. Swanson and N. A. Martin, “Field electron cathode stability studies: Zirconium/tungsten thermal-field cathode,” *J. Appl. Phys.*, vol. 46, no. 5, pp. 2029–2050, 1975.

[160] H. Li and R. C. Bradt, “Knoop microhardness anisotropy of single-crystal LaB6,” *Mater. Sci. Eng. A*, vol. 142, no. 1, pp. 51–61, 1991.

[161] G. Singh *et al.*, “Fabrication and characterization of a focused ion beam milled lanthanum hexaboride based cold field electron emitter source,” *Appl. Phys. Lett.*, vol. 113, no. 9, 2018.

[162] M. D. V. Longuet-Higgins, Hugh Christopher; Roberts, “The electronic structure of the borides MB6,” *1954*, vol. 224, no. 1158, pp. 336–347, 1954.

[163] A. Hasegawa *et al.*, “Energy bandstructure and Fermi surface of LaB 6 by a self-consistent APW method Self-consistent energy bands and Fermi surface of YZn Electronic structure of CsAu Self-consistent relativistic band structure for Pb at normal and high pressure Semi-empirical band structure theory Electronic structure of La monopnictides,” *J. Phys. F Met. Phys*, vol. 7, 1977.

[164] R. Nishitani *et al.*, “Surface structures and work functions of the LaB6 (100), (110) and

(111) clean surfaces," *Surf. Sci.*, vol. 93, no. 2–3, pp. 535–549, 1980.

[165] M. Aono, C. Oshima, T. Tanaka, E. Bannai, and S. Kawai, "Structure of the LaB6 (001) surface studied by angle- resolved XPS and LEED," vol. 2761, no. May 2014, pp. 12–16, 1989.

[166] M. Trenary, "Surface science studies of metal hexaborides," *Sci. Technol. Adv. Mater.*, vol. 13, no. 2, 2012.

[167] H. E. Gallagher, "Poisoning of LaB6 Cathodes," *J. Appl. Phys.*, vol. 40, no. 1, pp. 44–51, Jan. 1969.

[168] W. Zhu, Ed., *Vacuum Microelectronics*. John Wiley & Sons, Inc., 2001.

[169] W. P. Dyke and J. K. Trolan, "Field emission: Large current densities, space charge, and the vacuum arc," *Phys. Rev.*, 1953.

[170] R. Urban, R. A. Wolkow, and J. L. Pitters, "Evaluating angular ion current density for atomically defined nanotips," *Microsc. Microanal.*, vol. 20, no. 5, pp. 1514–1520, 2014.

[171] M. J. Fransen, T. L. Van Rooy, and P. Kruit, "Field emission energy distributions from individual multiwalled carbon nanotubes," *Appl. Surf. Sci.*, 1999.

[172] A. A. Holscher, "A field emission retarding potential method for measuring work functions," *Surf. Sci.*, vol. 4, no. September 1964, pp. 89–102, 1966.

[173] P. H. D. Kura, "Investigation of the photoelectric work function of titanium," Washington, 1952.

[174] T. Swanson, L. W.; Dickinson, "Single-crystal work-function and evaporation measurements of LaB6," *Appl. Phys. Lett.*, vol. 28, no. 578, 1976.

[175] W. B. Nottingham *et al.*, *Electron-Emission Gas Discharges I / Elektronen-Emission Gasentladungen I*, vol. 4 / 21. 1956.

[176] P. H. Levine, "Thermoelectric Phenomena Associated with Electron-Field Emission," *J. Appl. Phys.*, vol. 582, no. June 2004, 1962.

[177] D. Lide, *CRC Handbook of Chemistry and Physics*, 75th ed. CRC press, 1995.

[178] J. J. Gilvarry, "The Lindemann and Gr\"uneisen Laws," *Phys. Rev.*, vol. 102, no. 2, pp. 308–316, Apr. 1956.

[179] D. C. Agrawal, "Grüneisen ' s law for the classroom," *Phys. Educ.*, vol. 36, no. 486, 2001.

[180] N. N. Sirota, V. V Novikov, V. A. Vinokurov, and Y. B. Paderno, "Temperature dependence of the heat capacity and lattice constant of lanthanum and samarium hexaborides," *Phys. Solid State*, vol. 40, no. 11, pp. 1856–1858, 1998.

[181] F. Hulliger, ".," *Solid State Commun.*, vol. 15, no. 6, p. 933, 1974.

[182] M. D. Williams, L. T. Jackson, D. O. Kippenhan, K. N. Leung, M. K. West, and C. K. Crawford, "Lanthanum hexaboride (LaB6) resistivity measurement," *Appl. Phys. Lett.*, vol. 50, no. 25, pp. 1844–1845, Jun. 1987.

[183] V. I. Ivashchenko, P. E. A. Turchi, V. I. Shevchenko, N. R. Medukh, J. Leszczynski, and L. Gorb, “Electronic, thermodynamics and mechanical properties of LaB6 from first-principles,” *Phys. B Condens. Matter*, vol. 531, no. December 2017, pp. 216–222, 2018.

[184] P. A. Popov, V. V Novikov, A. A. Sidorov, and E. V Maksimenko, “Thermal conductivity of LaB6 and SmB6 in the range 6–300 K,” *Inorg. Mater.*, vol. 43, no. 11, pp. 1187–1191, 2007.

[185] J. M. Lafferty, “Boride cathodes,” *J. Appl. Phys.*, vol. 22, no. 3, pp. 299–309, 1951.

[186] M. Drechsler, “Erwin Müller and the early development of field emission microscopy,” *Surf. Sci.*, vol. 70, no. 1, pp. 1–18, 1978.

[187] T. Tanaka, J. Yoshimoto, M. Ishli, and E. Bannai, “ELASTIC CONSTANTS OF LaB6 AT ROOM TEMPERATURE,” *Solid State Commun.*, vol. 22, pp. 203–205, 1977.

[188] M. Futamoto, T. Aita, and U. Kawabe, “Microhardness of hexaboride single crystals,” *Mater. Res. Bull.*, vol. 14, no. 10, pp. 1329–1334, Oct. 1979.

[189] G. . Krotevich, D. N.; Ptitsyn,V.E; and Fursey, “Spontaneous build-up of a field emission cathode at maximum current densities,” *Zh.Tech.Fiz.*, vol. 55, no. 3, pp. 625–627, 1985.

[190] D. . Fursey, G. N; Ptitsyn, V.E; Krotevich, “Spontaneous migration of the surface atoms at maximum current densities of the field-electron emission initiating vacuun breakdown,” in *11th ISDEIV, Berlin, GDR*, 1984, pp. 69–71.

[191] B. L. Qian and H. E. Elsayed-Ali, “Electron pulse broadening due to space charge effects in a photoelectron gun for electron diffraction and streak camera systems,” *J. Appl. Phys.*, vol. 91, no. 1, pp. 462–468, 2002.

[192] C. Xu, J ; Möller, R; Läuger, K; Dransfeld, K; Williams C, “On the Energy Dissipation in Field Emission and Tunneling Microscopy,” in *Nanosources and Manipulation of Atoms Under High Fields and Temperatures: Applications*, pp. 89–100.

[193] A. Lubk and F. Röder, “Phase-space foundations of electron holography,” *Phys. Rev. A - At. Mol. Opt. Phys.*, 2015.

[194] J. C. H. Spence, W. Qian, and M. P. Silverman, “Electron source brightness and degeneracy from Fresnel fringes in field emission point projection microscopy,” *J. Vac. Sci. Technol. A Vacuum, Surfaces, Film.*, vol. 12, no. 2, pp. 542–547, 1994.

[195] “Longitudinal Coherence,” *C*, 2010.

[196] A. M. Michalik, E. Y. Sherman, and J. E. Sipe, “Theory of ultrafast electron diffraction: The role of the electron bunch properties,” *J. Appl. Phys. J. Appl. Phys. Appl. Phys. Lett. J. Appl. Phys*, vol. 104, no. 102, 2008.

[197] F. O. Kirchner, S. Lahme, F. Krausz, and P. Baum, “Coherence of femtosecond single electrons exceeds biomolecular dimensions,” *New J. Phys.*, 2013.

[198] P. Kruit, T. Verduin, and B. Cook, “Stochastic Coulomb interactions limitation to brightness of electron sources,” *Proc. - 2010 8th Int. Vac. Electron Sources Conf.*

Nanocarbon, IVESC 2010 NANOcarbon 2010, pp. 29–30, 2010.

[199] C. Han, I. Sul, and B. Cho, “Edge shadow projection method for measuring the brightness of electron guns,” *Rev. Sci. Instrum.*, vol. 88, no. 2, 2017.

[200] I.-S. Hwang, H.-S. Kuo, C.-C. Chang, and T. T. Tsong, “Noble-Metal Covered W(111) Single-Atom Electron Sources,” *J. Electrochem. Soc.*, vol. 157, no. 2, p. P7, 2010.

[201] J. C. . Scheinfein,M.R; Qian, W; and Spence, “Aberrations of emission cathodes: Nanometer diameter field-emission electron sources,” *J. Appl. Phys.*, vol. 73, no. 2057, 1993.

[202] J. C. H. Spence and M. R. Howells, “Synchrotron soft X-ray and field-emission electron sources: a comparison,” *Ultramicroscopy*, vol. 93, no. 3–4, pp. 213–222, 2002.

[203] F. Zolotorev,M; Commins D., E; Sannibale, “Theory and proposal for a quantum-degenerate electron source,” *LBNL Form. Rep.*, vol. 61587, 2006.

[204] P. Lougovski and H. Batelaan, “Quantum description and properties of electrons emitted from pulsed nanotip electron sources,” *Phys. Rev. A - At. Mol. Opt. Phys.*, vol. 84, no. 2, pp. 1–11, 2011.

[205] S. Keramati, E. Jones, J. Armstrong, and H. Batelaan, “Partially coherent quantum degenerate electron matter waves,” *Adv. Imaging Electron Phys.*, pp. 1–25, 2020.

[206] J. Orloff, Ed., *Handbook of Charged Particle Optics*, 2nd ed. Boca Raton, 2009.

[207] J. D. Jarvis, N. Ghosh, B. L. Ivanov, J. L. Kohler, J. L. Davidson, and C. A. Brau, “Resonant tunneling and extreme brightness from diamond field emitters and carbon nanotubes,” *FEL 2010 - 32nd Int. Free Electron Laser Conf.*, pp. 504–507, 2010.

[208] M. Zolotorev, E. D. Commins, and F. Sannibale, “Proposal for a Quantum-Degenerate Electron Source,” *Phys. Rev. Lett.*, vol. 98, no. 18, p. 184801, May 2007.

[209] B. J. Claessens, S. B. van der Geer, G. Taban, E. J. D. Vredenbregt, and O. J. Luiten, “Ultracold Electron Source,” *Phys. Rev. Lett.*, vol. 95, no. 16, p. 164801, Oct. 2005.

[210] G. A. Morton and E. G. Ramberg, “Point projector electron microscope [4],” *Phys. Rev.*, vol. 56, no. 7, p. 705, 1939.

[211] V. T. Binh, V. Semet, S. T. Purcell, and F. Feschet, “Fresnel Projection Microscopy , Theory and Experiment : Electron Microscopy With Nanometer Resolution At 200 Volts,” *Scanning Microsc.*, vol. 12, no. 1, pp. 93–106, 1998.

[212] van C. Zernicke, “Degree of coherence,” *Physica*, vol. 1, pp. 201–204, 1934.

[213] D. Cronin D., Alexander; Schmiedmayer, Jörg; Pritchard E., “Optics and interferometry with atoms and molecules,” *Rev. Mod. Phys.*, vol. 81, no. 1051, 2009.

[214] V. T. Binh, V. Semet, S. T. Purcell, and F. Feschet, “Fresnel Projection Microscopy, Theory and Experiment: Electron Microscopy with Nanometer Resolution at 200 Volts,” *eCM J.*, vol. 12, no. January, p. 93, 1998.

[215] M. P. Silverman, “Microscopy and interferometry with an atomic-scale electron source ,” *Curr. Sci.*, vol. 68, no. 10, pp. 1003–1009, 1995.

[216] "Technical Information MCP Assembly, Hamamatsu Photonics K.K., Electron Tube Division," 2006. [Online]. Available: http://www.triumf.ca/sites/default/files/Hamamatsu MCP guide.pdf.

[217] J. Ladislas Wiza, "Microchannel plate detectors," *Nucl. Instruments Methods*, vol. 162, no. 1, pp. 587–601, 1979.

[218] A. S. Tremsin and O. H. W. Siegmund, "Spatial distribution of electron cloud footprints from microchannel plates: Measurements and modeling," *Rev. Sci. Instrum.*, vol. 70, no. 8, pp. 3282–3288, Jul. 1999.

[219] W. Spence, J. C. H.; Qian, "Transmission-electron Fourier imaging of crystal lattices using low-voltage field-emission sources: Theory," *Phys. Rev. B*, vol. 45, no. 10271, 1992.

[220] E. E. Martin, J. K. Trolan, and W. P. Dyke, "Stable, High Density Field Emission Cold Cathode Analytic transmission for field emission from coated cold cathodes Theoretical analysis of field emission from a metal diamond cold cathode emitter Stable, High Density Field Emission Cold Cathode*," *J. Appl. Phys. J. Appl. Phys. J. Appl. Phys. J. Vac. Sci. Technol. B J. Vac. Sci. Technol. A*, vol. 31, no. 5, 1960.

Acknowledgements

Incommensurable thanks to my parents and brothers who have always guided me towards an academic career and support me in tough times, nothing of these would have been possible without them.

I would like to acknowledge Professor R. J. Dwayne Miller for allowing me to work in a precious environment and granted me access to state-of-the-art scientific instruments which were compulsory for the success of this work. Thanks to Professor Franz X. Kärtner for attending my Ph.D. annual panel meeting to analyze the progress even his tight schedule. My most profound appreciation to Günther Kassier and Robert Bücker for guiding me throughout this Ph.D. work and for also being helpful and motivating colleagues during all these years. Thank you all for your guidance and support.

Also, the help of the following people is highly acknowledged:

Professor Henry Chapman for granting access to their FIB and SEM machine. Sincere thanks to Miriam Barthelmeß for providing the training in SEM and putting so many efforts in the FIB milling process even in a busy schedule. Professor Rafal Borkowski at Julich Forschungszentrum for providing the FIB milling beam time. I am also very grateful to Prof. Steve Purcell at ILM CNRS to introduce me to the area of field emission during my first year of Ph.D.

I am very grateful to the technical staff: Djordje Gitaric and Josef Gonschior for their help with technical drawings. Also, I would like to appreciate the tiring efforts of SSU team members throughout this Ph.D. work. Special thanks to Henrik Schikora and Martin Kollowe who helped me in modifying the test chamber at different stages. Also, thanks to Friedjoff Tellkamp and Jan Phillip for helping me occasionally. Thanks to Nadja Bardenheuer, Kirsten Teschke, Kathja Schröder, Tania Hartin, Neda Lotfiomran, Miriam Lange and Ulrike Warda, Ute Kaluza for their administrative support. Peter Johanssen and Björn Witt for their IT support. Also, I sincerely thank Steffi Killough, Anna Kazakova, Gabriella Kirstein, Maria Peker for their help in visa procedures which made life easy in a foreign land.

Thanks to the wonderful colleagues Sana Azim, Chiwon Lee, Sacha Epp, Ajay Jha, Vandana Tiwari, Maria Katsiaflaka, Andrey Krutlin for making the last five years so pleasant.